Dynamic modelling of post-collisional magmatism

Lars Mikael Kaislaniemi
Earth Science Department
Durham University

A thesis submitted for the degree of
Doctor of Philosophy (PhD)
November 2014

Abstract

This study addresses the question of post-collisional magmatism and its production mechanisms, addressing especially the mantle processes involved. Numerical experiments are conducted to examine the effects of viscosity weakening by subduction related water content increase in the upper mantle and the resulting sub-lithospheric small-scale convection. The models presented incorporate parameterized and thermodynamic melting models, and take into account variable relationships between mantle water content, mantle strength, water extraction by partial melting and related depletion stiffening.

The results demonstrate the possible importance of so called "hydrous activation" of the lithosphere-asthenosphere boundary: The post-collisional loss of the lithospheric mantle can be initiated and augmented by the elevated upper mantle water contents that enhances the sub-lithospheric small-scale convection, increases heat flow into the lithosphere, and produces localized lithosphere thinning. The irregular spatial and temporal melting patterns and the mantle melt volumes correspond to typical post-collisional mantle-derived magmatism. The small-scale convection can be localized into an edge-driven convection by significant lithosphere thickness gradients, e.g. craton edges. This helps to understand the uplift and volcanism observed in intraplate orogenic settings and implies the importance of these processes at other locations of lithosphere thickness gradients, e.g. recent collision zones.

The lithospheric thinning produced by small-scale convection can initiate whole lithosphere mantle loss via positive feedback mechanisms: gradual thinning of the lithosphere causes partial melting in the lowermost crust, weakening the crust-mantle boundary and providing a detachment mechanism for the lithospheric mantle, leading to stronger lithosphere thinning and, finally, exposure of the lower crust to the hot asthenosphere.

Small-scale convection and processes related to or initiated by it offer new insight and future research possibilities in studies of continental collision magmatism.

Contents

List of Figures

List of Tables

Declaration

I, Lars Mikael Kaislaniemi, declare that this thesis, presented for the degree of Doctor of Philosophy at Durham University, is a result of my own original research and has not been previously submitted to Durham University or any other institution. Any previously published material and the contributions of colleagues have been, when appropriate, clearly indicated.

The thesis work was conducted from October 2011 to November 2014 under the supervision of Dr Jeroen van Hunen and Dr Mark Allen at Durham University.

Signed: _____
Lars Mikael Kaislaniemi

Date: _____

Acknowledgments

I am greatly indebted to *Jeroen* for providing exceptionally good supervision and training during my PhD studies, and spending countless hours reading and scribbling comments and feedback on my works and manuscripts. Equally large gratitude has to be expressed to *Mark* for not only hugely helpful feedback but also for most intriguing discussions on geological problems related to my PhD work and for "geological reality checks" that are so often overlooked by those concentrating too much on their world of computers and numerical models. I also want to thank *Iain Neill*, *Pierre Bouilhol* and *Jean-François Moyen* for valuable and fruitful comments and discussions during my PhD. Working with *Valentina Magni*, *Roberto Agrusta*, *Hongliang Wang* and *Andy Bottrill* has been of great help in using and developing (and bearing the quirks of the) computer software used for my models.

None of the work would have been possible without the funding from the European Union Marie Curie Initial Training Network *'Topomod'*, and the PhD time would not have been nearly as unforgettable as it was without the short courses and field excursions spent with the Topomod fellows and fellow supervisors. Computing facilities have been provided by the Durham University High Performance Computing service and the N8 Consortium co-ordinated by the Universities of Leeds and Manchester.

Finally, the nearly immeasurable stock of fresh 'pulla' provided by *Maria* during the last three years has been of outmost importance in accomplishing this project.

Chapter 1

Introduction

The model of plate tectonics and the so called Wilson cycle succesfully describes the sequence of rifting of continents, seafloor spreading and continental drift, closure of the ocean by subduction of the oceanic plate, and continental collision. All the related structural and magmatic phenomena at the plate boundaries are well explained within this framework. However, the geodynamic setting following a continental collision—rapid uplift, widespread post-collisional igneous activity and crustal deformation in what is effectively an intracontinental environment—has no explanation in this framework or is merely described as a relaxation phase after the collision (Bird, 1979). The post-collisional stage is a distinct period, separate from the subduction and peak of the collision preceding it: the widespread within-plate magmatism observed (Dilek and Altunkayanak, 2007; Williams, 2004; Sylvester, 1989; Black et al., 1985) cannot be related to the subduction phase, as these subduction related rocks would have been strongly metamorphosed during the collision, neither can it be related to the collision (i.e. period of maximum convergence) itself, for the compression effectively prevents the ascent of magmas (Brown, 1994). Furthermore, this post-collisional magmatism is often associated with significant uplift—formation of orogenic plateaux—and continuing crustal deformation unconnected to the plate tectonic forces. The question of how to integrate the evolution of orogenic belts in post-collisional and post-orogenic stages into the plate tectonic framework has been studied from point of view of both magmatic (Ducea, 2011; Bonin, 2004; Keskin, 2003; Chung et al., 2003; Väisänen et al., 2000; Sylvester, 1989) as well as structural and large scale geodynamic (Francois et al., 2014; van Hunen and Allen, 2011; Gögüs and Pysklywec, 2008; Le Pourhiet et al., 2006; Black and Liégeois, 1993; England and Houseman, 1989) evolution. Unresolved issues remain in deciphering the relation between large scale mantle processes and geologically observable processes, such as the timing of plateau uplift (Spencer, 1996; Guo, 2006; Mouthereau, 2011) and the relative importance of different petrogenetic (Bonin, 2004) and heat sources of post-collisional magmatism (Kukkonen and Lauri, 2009; Bodorkos et al., 2002; Petford and Gallagher, 2001; Thompson and Connolly, 1995; England and Thompson, 1984).

1.1 Stages of continental collision

Continental collision starts with the final stages of oceanic subduction and closure of an oceanic basin between the colliding continents. The oceanic plate will be completely subducted under the overriding plate, and the continental crust following it can subduct to about 150-200 km, sometimes even deeper (Ye et al., 2000). The subduction of continental crust forms the ultra-high pressure metamorphic suites observed at collision zones (Chopin, 2003). Activity of the volcanic arc during the oceanic subduction diminishes and stops. Finally, the buoyancy of the continental crust prohibits it from subducting further, and it collides with the overriding plate, forming the uplifted mountain range and "docking" the colliding continental blocks together and forming a new continental land mass.

The nomenclature for periods following the peak of the collision (maximum convergence and maximum deformation) is not well agreed upon. The traditional classification into synorogenic, late orogenic, post-orogenic and anorogenic (Sederholm, 1934) is obscured by the fact that the datings for rocks of "late orogenic" and "post-orogenic" often overlap or that they might be difficult to discreminate from each other based on their geochemistry (Bergman et al., 1995; Liégeois et al., 1998). Following the suggestions of Bonin et al. (1998) and Liégeois (1998), the orogenic timeline is divided into orogenic, post-orogenic and anorogenic stages (Fig. 1.1). These stages take place in different tectonic settings, namely the active margin, collisional, post-collisional, and intraplate setting.

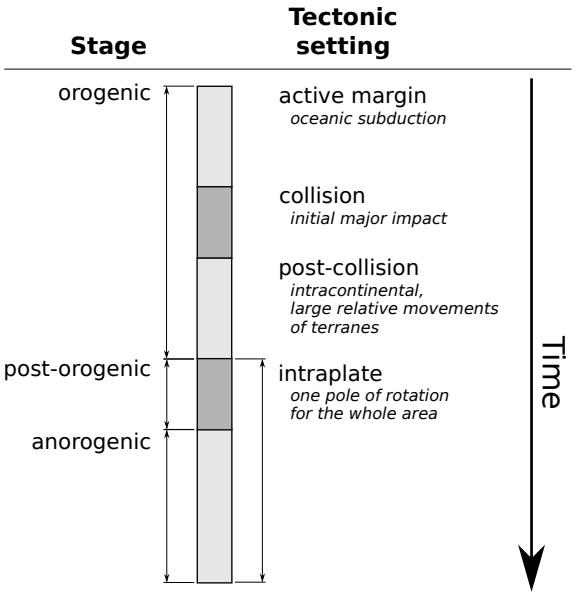

Figure 1.1: Progression of orogenic event, after Liégeois (1998).

The major division between orogenic and post-orogenic stages is the criterion of having the collided plates moving regionally as one coherent plate. This corresponds to the switch from post-collisional to an intraplate tectonic setting. The anorogenic stage shows no plate convergence but is associated with alkaline magmatic suites which have a common mantle source and on a global scale can be related to large contemporaneos collision events (Black et al., 1985).

Within the orogenic stage the switch from collisional tectonic setting to a post-collisional one is relatively poorly defined. The post-collisional setting can be characterized by following properties (Liégeois, 1998; Bonin, 2004):

1. Plate convergence continues, with intracontinental thrust, wrench deformation and possible

lateral escape of discrete terranes. Large horizontal movements along these shear zones are associated with ...

2. ... magmatic events with a) potassic to ultrapotassic calc-alkaline rocks shifting towards more alkaline at later stages of the orogen, and b) sporadic but possibly voluminous strongly peraluminous and sodic alkaline-peralkaline granitoids ;

3. the source of the magmatism lies in the subduction modified mantle and crust with an ambiguous isotopic signature.

During the late stages of the orogeny, mountain belts often experience crustal scale collapse (Dewey, 1988). Reasons and mechanisms for the collapse can be various. Suggested mechanisms include the collapse of the overthickened crust after gaining more potential energy than can be supported by the plate tectonic lateral forces produced by the waning convergence. A sudden increase in the potential energy, causing it to exceed the lateral support, can be introduced by the loss of the destabilized mantle root (Molnar et al., 1993; England and Houseman, 1989; Dewey, 1988) and the strength of the crust due to rheological changes during the orogeny (Vanderhaeghe and Teyssier, 2001).

After the loss of the mantle root, rapid uplift, orogenic collapse and voluminous magmatism and crustal anatexis, the thinned lithospheric mantle starts to grow by cooling back to its original thickness (Black and Liégeois, 1993). This marks the end of the major orogenic episode and the post-orogenic period commences. Petrologically, this switch can be oserved in the geochemistry of the post-collisional and post-orogenic rocks. The post-collisional suites can be complex and heterogeneous. They include felsic peraluminous (molar ratio $Al_2O_3/(K_2O + Na_2O + CaO)$, or A/CNK, greater than one) rocks, usually granites or leucogranites but also granitoids and tonalites, that indicate involvement of a metasedimentary crustal source and dehydration melting of muscovite or biotite (Sylvester, 1998). The post-collisional rocks also include the metaluminous (A/CNK < 1 but A/NK > 1) mafic-felsic igneous suites that are composed of medium- to high-K calc-alkaline suites (source in metasomatised lithospheric amphibole-spinel peridotite) and shoshonitic to ultrapotassic metaluminous suites. The high potassium content of the latter is explained by involvement of phlogopite in the partial melting of depleted garnet-bearing lithospheric upper mantle that has been metasomatized by subducted material (Bonin, 2004). The post-orogenic association includes mafic and felsic rocks that range from alkali-calcic metaluminous to peralkaline (A/NK < 1) and in which the composition trends toward more sodic rather than potassic. These post-orogenic associations evolve towards alkaline within-plate magmatism, evidencing the increasing role of enriched ocean island basalt mantle sources, and in general waning role of the crustal anatexis during the transition from post-collisional to post-orogenic (Bonin, 2004).

1.2 Mechanisms of lithosphere thinning

1.2.1 Stability of thickened lithosphere

Delamination, convective removal, foundering, and lithospheric dripping are some of the terms used for closely related processes used to explain the lithospheric thinning, usually in a late-orogenic

setting. They all share the same idea of gravitational instability of the lithosphere: Because of compositional differences, the lithospheric mantle is more dense than the crust above it, but because of its lower temperature, the lithospheric mantle is also more dense than the asthenospheric mantle below it (Kay and Mahlburg Kay, 1993). The lithospheric mantle is thus gravitationally instable and is prone to being recycled into the asthenosphere. It is also possible for the lower crust to become negatively buoyant (relative to the mantle lithosphere below) via phase changes taking place during the thickening of the crust (Kay and Mahlburg-Kay, 1991). The high temperature dependence of the lithospheric strength ensures that the cold lithospheric mantle stays attached to the overlying crust. This, however, might be disturbed by processes during an orogenic sequence. Two lines of evidence are used to argue that lithospheric mantle and/or lower crust is being frequently recycled back to the deeper mantle:

1. The extreme shortening at continental convergent margins should produce much thicker mantle lithospheres than is observed (DeCelles et al., 2009).

2. The intermediate average bulk composition of the continental crust (Rudnick and Fountain, 1995) requires an ultramafic complementary residue. However, such a reservoir seems absent in many continental areas.

Delamination of the lithosphere, in its original sense (Bird, 1979), refers to the "peeling off" of the lithospheric mantle, detaching from the crust along a zone of weakness. This requires a weak lower crust and a weak conduit from the asthenosphere to the moho level for a starting point for the delamination. Today, delamination is used in a relatively wide sense, but still refers to the process of decoupling the lithospheric mantle (and, possibly with it, parts of the lower crust) from the overlying crust (Meissner and Mooney, 1998).

Convective removal of the lithosphere, or lithospheric dripping, is caused by the thickening of the lithosphere: thickened, colder lithosphere, is pushed downwards into more buoyant asthenosphere, which initiates a Rayleigh-Taylor instability at the asthenosphere-lithosphere boundary (Houseman and Molnar, 1997). This leads to "drips" of lithospheric material to drop into the asthenosphere, accompanied by asthenospheric material flowing upwards in between the drips. If these instabilities reach to the mantle-crust boundary, the upwelling asthenosphere might work as the weak conduit needed to initiate the delamination of the lithosphere (Morency and Doin, 2004).

Crustal delamination can take place when the lowermost mafic crust is transformed into eclogite and so becomes more dense than the underlying mantle (Arndt and Goldstein, 1989; Rey, 1993). The eclogitization might happen as a solid-state phase change as a consequence of the crustal thickening and increasing pressure (Leech, 2001), or it can take place as a consequence of extraction of partial melts, leaving behind an eclogitic residue (Ducea, 2002; Lee et al., 2006).

The gravitational instability of the lithospheric mantle is a balance between compositional (intrinsic) density and the thermal buoyancy (thermal expansion). The intrinsic density of the lithospheric mantle varies (e.g. Poudjom Djomani et al., 2001; Lenardic and Moresi, 1999) but is on average slightly more buoyant than the asthenosphere below it. However, the density decrease related to the thermal expansion can make the hotter asthenosphere effectively less dense. The magnitude of this effect, however, is very close to that of the intrinsic density difference (Kay and Mahlburg

Kay, 1993), so that a lithospheric mantle that is intrinsically 1.5% more buoyant than the asthenosphere below it, has effectively the same buoyancy as the asthenosphere. The secular evolution of the mean composition of the newly formed sub-continental lithospheric mantle (towards less depleted) is likely to have made the lithospheric mantle slightly more dense in the Phanerozoic than what it was in the Archaean, and, on the other hand, the pressure dependency of the effect of depletion on density, a thin Phanerozoic lithospheric mantle slightly less buoyant than a thick one (Poudjom Djomani et al., 2001).

The weak lower crust required for the mantle delamination is considered in the so called "jelly sandwich" rheology model of the lithosphere (Meissner and Strehlau, 1982; Zuber, 1994) that has been later refined (e.g. Singh and McKenzie, 1993; Hirth and Tullis, 1994), but retains the idea of stratification of rheological properties in the lithosphere being caused by petrological stratification. This leads to a relatively strong lithospheric mantle and upper-middle crust and to a weak lower crust that can act as detachment zone in the delamination. The model has been challenged by the so called "crème brûlée" model where most of the strength of the lithosphere resides in the upper crust (Jackson, 2002), though this model has been criticized for not being able to predict a stable lithospheric structure (Burov, 2006).

Despite the uncertainties related to the buoyancy and rheological structure of the lithosphere, the concept of delamination/convective removal of the lithosphere is widely used. This is due to the difficulties of explaining the late-stage extension of orogenies without involving other processes than crustal thickening and cessation of plate convergence (England and Houseman, 1989). Several active and ancient mountain belts, such as the Variscan (Faure et al., 2009), the Basin and Range in Western USA (Colgan et al., 2006), the Aegean sea region (Jackson et al., 1992) and the New Guinea orogen (Abers, 1991), show late stage crustal extension and normal faulting at a stage where thrust faulting and crustal thickening had already taken place or where thrust faulting continues at the margins of the plateau while extension dominates elsewhere (Houseman and Molnar, 1997). Initially, the release of the potential energy, stored in the thickened crust, was seen responsible for driving the extension and normal faulting. However, such a model cannot explain the change from the thrust faulting to normal faulting, often even while large scale tectonic environment still remains in a convergence (e.g. Armijo and Tapponnier, 1986; England and Houseman, 1989). An additional process, the loss of lithospheric mantle, is needed to explain these features (Houseman and Molnar, 1997; Platt and England, 1993). In addition, the rapid uplift and the voluminous magmatism and high temperature metamorphism associated with the change from compressional to extensional regime (the "collapse" of the orogen, Dewey, 1988) are hard to explain without a lithosphere loss. These features in numerous recent orogenies (Andean Altiplano-Puna plateaux (Allmendinger et al., 1997), Tibetan plateau (Molnar et al., 1993), Eastern Anatolia (Keskin, 2003), Eastern Carpathians (Fillerup et al., 2010), Sierra Nevada region (Ducea and Saleeby, 1998), Variscan orogeny (Gutiérrez-Alonso et al., 2012)) show that they are an important process in orogen evolution and the loss of lithospheric mantle needs to be considered when examining the geodynamic history of these regions. The temporal evolution of ancient orogenies is harder to constrain, but similar late stage extensional features, magmatism and crustal collapse has been observed in the deep exhumed parts of the Proterozoic Svecofennian orogeny and in the Neoproterozoic Arabian-Nubian shield (e.g. Korja et al., 2009; Avigad and Gvirtzman,

2009).

Jackson et al. (2004) have proposed that the strength of the thick roots supporting the high mountains is due to metastable granulite: the granulite, even if at high pressure at eclogite stability conditions, would not transform into eclogite for kinematic reasons, and requires introduction of water to initiate and accelerate the transformation. This transformation would then also be accompanied by loss of strength, and together these processes would remove the support of the root for the high mountains above. This could explain how the collapse could be initiated without loss of lithospheric mantle. However, the eclogitization of the lower crust is likely to enhance the chances for crustal delamination and thus also loss of lithosheric mantle (Krystopowicz and Currie, 2013).

Seismic evidence for the loss of the lithospheric mantle also exists. Beck and Zandt (2002) and Schurr et al. (2006) show low velocities and high attenuation underneath most of the Altiplano-Puna plateau in the Andes, implying high temperatures and the absence of the lithospheric mantle. Same has been concluded for the eastern Anatolia on the Turkish-Iranian plateau (Gök et al., 2007). The steep distribution of deep earthquakes underneath the eastern Carpathians is suggested to picture an active delamination event (Knapp et al., 2005), and delamination of the crustal root of an arc has been pictured in tomographic images of the Southern Sierra Nevada (Zandt et al., 2004).

The exact mechanisms for the initiation of the loss of the lithospheric mantle remains an open question. Two different sequences of events can be hypothesized (Meissner and Mooney, 1998): After the thickening of the crust the mountain belt collapses under its own weight due to changes in the plate tectonic stress system, and leads to lateral extrusion and thinning of the crust, together with upwelling asthenosphere and thus loss of the lithospheric mantle and subsequent uplift (England and Houseman, 1989; Houseman et al., 1981; Bird, 1979). The loss of the lithospheric mantle can also be seen as the primary cause for the collapse and thinning (Wells and Hoisch, 2008; Lang Farmer et al., 2002; Nelson, 1992). The loss of the lithospheric mantle would in that case lead to the uplift (causing an increase in the potential energy and exceeding the lateral support) and to a significant heat pulse in to the crust, weakening it, and enhancing the collapse.

Recognizing a lithospheric mantle loss event in a geological record and telling the difference between styles of lithospheric mantle loss (delamination in its strictest sense or convective removal) is hampered by the fact that melts can be produced from multiple different locations in a such situation (Ducea, 2011). Upwelling asthenosphere is the most likely source for melt production (Kay and Mahlburg Kay, 1993), but melting can also happen in the downgoing, delaminating pieces of crust by dehydration melting, similar to slab melting in a subduction setting (Elkins-Tanton, 2007), or by amphibole break-down (compressional melting due to negative dT/dP curve in the stability field (Iwamori, 1997)) in the convectively removed downwelling lithosphere. All the mantle sources could have been also recently affected by fluids and melts from the previous subduction. The heat pulse caused by the lithospheric mantle loss can lead to crustal melting. Thus, regardless of the style of the lithospheric mantle loss, a multitude of different melt sources is expected.

The volumes of mafic magmatism associated with areas of suspected lithosperic mantle loss are relatively low. This is the case for example in Sierra Nevada in California (Ducea and Saleeby,

1998; Lang Farmer et al., 2002), the Puna region in the Andes (Drew et al., 2009; Mahlburg Kay et al., 1994) and the Tibetan plateau (Chung et al., 2005). This could point to a convective style of lithosphere mantle loss where the removed pieces of the lithosphere are small in size. In this case the size of asthenosphere upwelling would also be small, and the timescales for the existence of the instabilities could be relatively large (Ducea, 2011; Morency and Doin, 2004; Morency et al., 2002). This would be in contrast to large instabilities, or catasthropic style of mantle delamination with very large lithosphere drips falling off to the asthenosphere, in which large melt volumes would be produced in short timescales. Regions of greater volumes of mafic melts associated with an alleged delamination event also exist, for example the Eastern Anatolia region of the Turkish-Iranian plateau (Gögüs and Pysklywec, 2008).

1.2.2 Small-scale convection

The stability of the lithosphere bottom can also be studied from another perspective. The classical half-space cooling model of the oceanic lithosphere (Turcotte and Schubert, 2001) describes the cooling of the oceanic plate as a conductive heat transfer process where the bathymetry and the thickness of the plate is proportional to the square root of time. This fits well with bathymetry observation from young oceanic plates but starts to deviate as the age of the plate increases. Unlike in the half-space cooling model, where the thickness of the lithosphere grows indefinitely due to conductive cooling of the lithosphere, the observations that the bathymetry and heat flow values on oceanic lithosphere approach an asymptotic value, point to a flattening of the old oceanic lithosphere bottom. This flattening of the lithosphere bottom is attributed to the small scale convection at the lithosphere-asthenosphere boundary (Huang, 2005; Dumoulin et al., 2001; Yuen and Fleitout, 1985; Buck, 1985), providing constant heat flow into the overlying lithosphere and balancing the cooling effect of the conduction.

The onset of small-scale convection can be understood schematically as a competing process between conductive and convective heat transfer (Fig. 1.2). The oceanic lithosphere forming at the mid-ocean ridge grows in thickness as long as the conductive cooling is strong enough to counteract the convective heating from below. Once the magnitude of conductive and convective heat flow are roughly equal, the tendency to find balance between these two drives recurring thickening (by conductive cooling) and thinning (by convective heating from below) of the lithosphere. Although small-scale convection formulation is developed for a simple stagnant lid convection regime with temperature dependent viscosity and no material buoyancy differences, most suitable to model oceanic settings, it has been applied succesfully also for continental lithosphere (Morency et al., 2002; Sleep, 2011; Doin et al., 1997; Sleep, 2005), giving insight into the stability of the roots of the thickened continental lithosphere. The major difference between small-scale convection models of oceanic (e.g. Ballmer et al., 2009) and continental settings (e.g. Kaislaniemi et al., 2014, Chapter 3) is that it is assumed that there is no preferred direction of shearing underneath the continental lithosphere.

Small-scale convection takes place in the so called stagnant lid convection regime where the viscosity of the convecting fluid is highly temperature dependent (Solomatov and Moresi, 2000). This temperature dependency forms a structure of very high viscosity immobile lid (lithosperic plates)

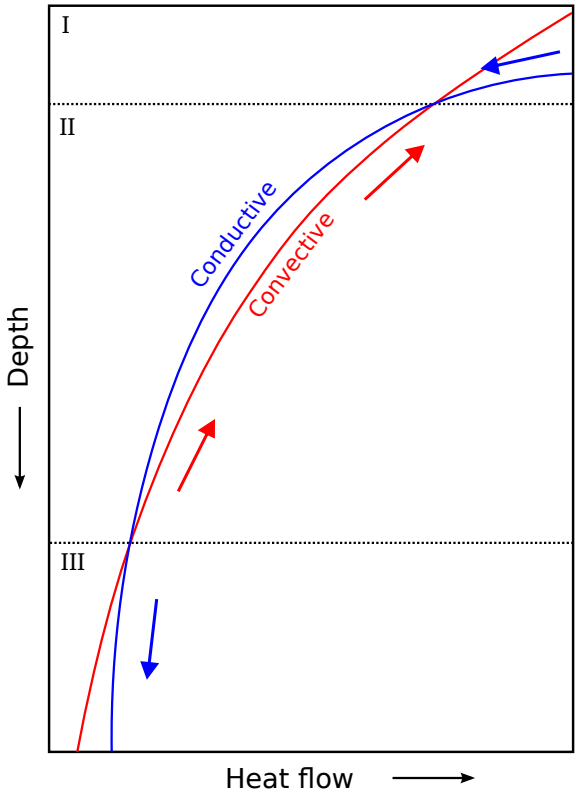

Figure 1.2: Schematic figure of the balance between conductive and convective heat transfer driving the small scale convection and forming a stable lithosphere thickness. A thin lithosphere (depth in region I) is governed by conductive heat transfer, cooling the lithosphere. As the thickness increases, the conductive heat flow decreases (inversely proportional to the thickness of the layer) and convective heat transfer comes relatively larger (region II). Pressure dependency of the viscosity causes the convective heat transfer to decrease with depth, finally decreasing below conductive heat transfer rate (region III). The depth between regions I and II is a stable depth which the lithosphere thickness approaches. Depths in region III are unstable and grow indefinitely via conductive cooling. Such a situation can occur in numerical models of mantle convection if initial lithosphere thickness is too large. Figure after Sleep (2011).

overlying the convecting fluid (asthenosphere). Between these two layers there is a rheological boundary layer where the small-scale convection takes place (Fig 1.3). The rheological temperature contrast across the rheological boundary layer, ΔT_{rheo}, adjusts itself so that to maximize the heat flow (Solomatov and Moresi, 2000). If the mantle viscosity is defined with

$$\eta \propto \exp\left(-\gamma T\right) ,$$

then

$$\Delta T_{rheo} \propto \gamma^{-1} , \tag{1.1}$$

(Solomatov and Moresi, 2000). The parameter γ quantifies how sensitive the mantle viscosity is to the temperature[1] T. If the temperature sensitivity approaches zero, the thickness of the rheological boundary layer approaches infinity, i.e. the whole mantle becomes a rheological boundary layer, and the convection is no more in the stagnant lid regime and there are no more rigid plates above the convecting mantle.

Because small-scale convection prohibits the growth of the lithosphere thickness, some counteracting mechanism is needed to explain the existence of the thick roots of cratonic lithosphere. The compositional buoyancy of continental lithosphere and the higher viscosity of the depleted lithospheric mantle are probable causes for the stability of the thick lithospheric roots (Wang et al., 2014; Sleep, 2005; Lenardic and Moresi, 1999; Doin et al., 1997). Conversely, the lack of these

[1] $\gamma = Q/RT_i^2$, where $Q = E^* + pV^*$ is the activation enthalpy (see section 2.1.4) and T_i is the temperature of the convective mantle.

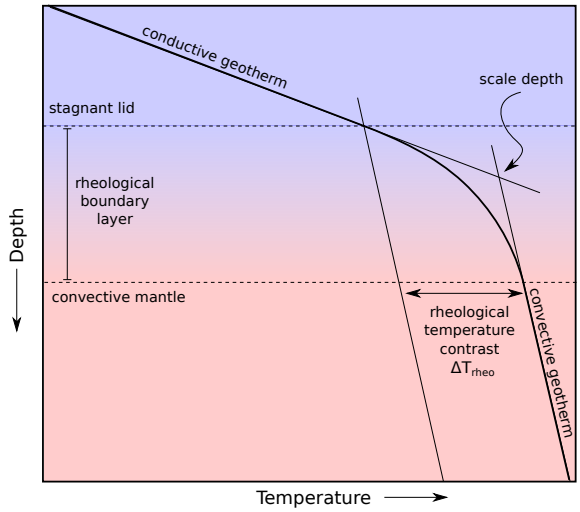

Figure 1.3: Rheological boundary layer between convective mantle and the stagnant lid is the region where both convective and conductive heat transfer are significant and thus the geotherm deviates from both the conductive geotherm and the mantle adiabat. The scale depth can be taken as an useful measure for the rheological thickness of the lithosphere. Figures after Sleep (2011) and Sleep (2005).

properties can be used to argue for lithospheric thinning by small-scale convection.

1.3 Mantle water contents

Water has profound effects on mantle dynamics: Although differing views exist (Fei et al., 2013), it is generally accepted that water has significant effects on the mantle viscosity (Karato, 2010). As the mechanisms held responsible for post-collisional magmatism involve mantle processes (lithosphere thinning, delamination, slab break-off), it is crucial to be aware of the factors affecting mantle strength. Laboratory experiments on olivine, the most abundant mantle mineral and as such controlling the mantle strength, show maximum weakening by water to be one to four orders of magnitude (Fei et al., 2013; Hirth and Kohlstedt, 1996; Mei and Kohlstedt, 2000; Karato, 2010). Changes in viscosity influence the whole mantle convection, but are especially important near thermal boundary layers, like the lithosphere, where viscosity affects the thickness of this boundary layer and the vigour of convection underneath it, and thus the heat flow through it (Sleep, 2011).

Water also affects the melting behaviour of the mantle (Asimow and Langmuir, 2003). Decreasing solidus temperature with increasing water contents enhances melting. In decompression melting this can lead to increased total melt volumes but smaller average extent of melting, affecting the composition of the produced melts. Partial melts in the mantle affect the viscosity as well (Mei et al., 2002).

Knowledge about the mantle water cycle has increased rapidly during the last decade. It has been known that the sources of the mid-ocean ridge basalts contain about 0.005-0.02 wt-% of water (Saal et al., 2002), and also that the minerals wadsleyite and ringwoodite, high-pressure polymorphs of olivine existing at the upper-lower mantle transition zone, can in theory contain 1-3 wt-% water (Kohlstedt et al., 1996; Smyth, 1987). The recent discovery (Pearson et al., 2014) of a ringwoodite inclusion in a diamond originating from the transition zone, however, gives direct evidence that the transition zone does include significant amounts of water, at least locally. Studies on seismic attenuation and electrical conductivity (Zhu et al., 2013; Kelbert et al., 2009) support the idea of more global hydration state of the mantle transition zone.

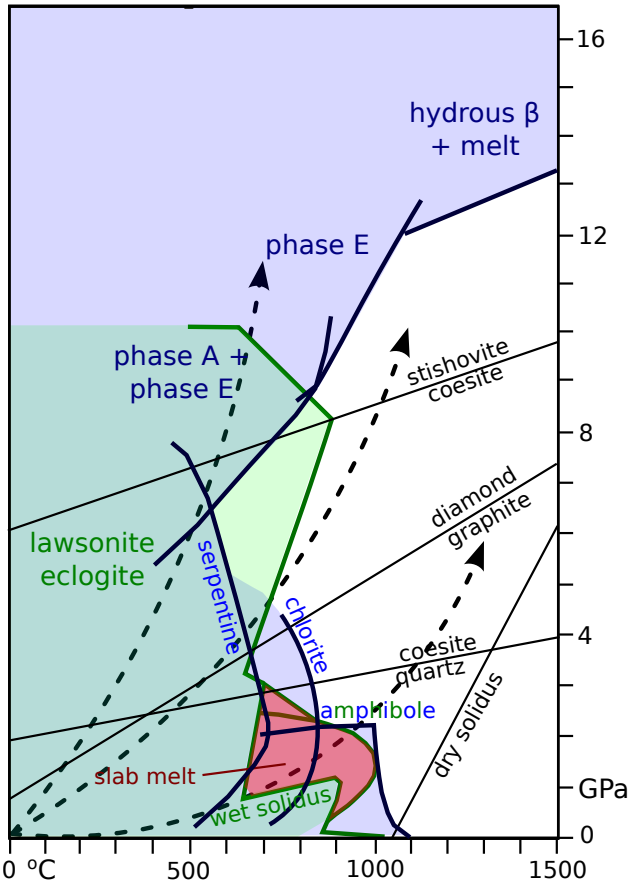

Figure 1.4: Simplified phase diagram for systems MORB+H_2O (green) and peridotite+H_2O (blue). Shaded areas show where hydrous phases are stable in each system. Dashed arrows plot a hot, moderate and cold geoterm. A plate subducting along a hot geotherm, will experience slab melting and dehydrate at conditions where hydrous peridotite phases are not stable. Any released fluids will percolate upwards in the mantle wedge. A slab going down along the cold geotherm will dehydrate slowly and at depths where hydrous phases in peridotite exist. Fluids released from the slab by dehydration form hydrous phases (phase A, phase E) in the mantle peridotite. These can be freely transferred downwards in mantle convection. Figure modified after Maruyama and Okamoto (2007).

Subduction zones are places where water can be circulated back in to the mantle. The oceanic slab, hydrated earlier at the ocean bottom by hydrothermal circulation, starts to dehydrate and release the fluids into the overlying mantle wedge, being the main cause for magma genesis in subduction zone environments (Delany and Helgeson, 1978; Tatsumi et al., 1986). However, in the light of high amounts of water at the mantle transition zone, it seems plausible to assume that downgoing oceanic slabs do not dehydrate completely at the vicinity of the subduction zones, and that they can bring down significant amounts of water beyond the shallow mantle levels (cf. Fig 1.4) (Maruyama and Okamoto, 2007).

Water in the mantle can be stored in the lattice space of nominally hydrous minerals, as on hydroxyl ion, forming an hydrogen bond with the principal anion, oxygen. This makes the water content in nominally anhydrous minerals pressure sensitive and explains their relative importance in the mantle. All major minerals in the uppermost mantle, olivine, pyroxenes and garnet can incorporate water. In addition, water can be stored in the hydrous magnesium-silicate mineral phases, phase-A and phase-E (Thompson, 1992).

Even though experimental data shows that very large quantities of water can be stored in the nominally anhydrous minerals, up to and over 0.4% just above the 410 km discontinuity (Hirschmann et al., 2005), the actual amounts existing in the upper mantle proves to be harder to estimate. Studies on electrical conductivity of mantle minerals (Dai and Karato, 2009) estimate bulk water contents in the asthenosphere of 0.01 to 0.04 wt-%, with probably smaller values underneath

continental regions (Wang et al., 2006). Considering the importance of subduction systems in the input of water in to the upper mantle, it is not surprising that mantle melts extracted at back-arc basin record water contents of 0.5 wt-% and more in their sources (Kelley et al., 2006). However, even at a distance of 400 km from the trench, these mantle melts still record water concentrations of almost 0.05 wt-% in their sources (Kelley et al., 2006), providing important information about the lateral extent to which a subduction zone can affect the water contents of the upper mantle. Geochemical data on mantle xenoliths and lavas in the western USA (Dixon et al., 2004) point to high water contents (up to 0.1 wt-%) in the uppermost mantle. This is credited to the long local history of subduction (at 100-30 Ma). In addition, long time lags (tens of millions of years) between subduction related hydration and the eruption of volcanics from the hydrated sources exist in some areas in western USA (Lange et al., 1993; Feldstein and Lange, 1999), pointing to relatively long residence times of the water in the upper mantle. Numerical models by Hernlund et al. (2008) show long time periods between the end of extension and onset of small-scale convection (and, thus, melt production by small-scale convection). This might be one reason for the long residence time of the water in the asthenosphere.

Despite the lack of full understanding of the water cycle in the Earth's mantle, it seems probable that there is significant variation in the water content of the upper mantle. This is caused by the subduction zones hydrating the mantle around them, and by the large amounts of water stored at the deeper level in mantle transition zone, while the melting events, most notably at mid-ocean ridges, continuously remove water from mantle. The mantle between crust and the transition zone can then become hydrated from above (subduction) but also from below, if the water-rich minerals from the transition zone move upwards across their stability field.

1.4 Thesis outline

This thesis consists of three studies looking at different aspects of continental collision magmatism. The emphasis is on the mafic, mantle-derived magmatism, the observations of which is being used to deduce the nature of mantle processes behind post-collisional magmatism (Chapters 3 and 4). For this, well-studied regions with existing mantle-derived primary magma compositions, such as the Turkish-Iranian plateau, are used as examples. Although volumetrically more significant (cf. Niu et al., 2013), the felsic magmatism in continental collisions is of limited use in trying to constrain the initial and boundary conditions for numerical models. Instead, regions with primary or near-primary post-collisional mantle melts, such as the Turkish-Iranian plateau, are used to to give simple constraints about the timing, volume and depth of melting. The interaction of mantle and crustal processes producing the high volume felsic magmatism is still, in its great complexity, beyond the capacity of most numerical models. However, an attempt is made (Chapter 5) to develope new methods for modelling of crustal melt production during and within mantle convection models of post-collisional settings.

Chapter 2 describes the physical principles and methods for the numerical calculations of the models in Chapters 3, 4 and 5, as well as the benchmarks used to test the numerical correctness of the models.

Chapter 3 presents a model of sub-lithospheric small-scale convection and describes how this process can produce the mantle-derived mafic post-collisional volcanism of the Turkish-Iranian plateau and other orogenic plateaux, with implications for other intra-continental volcanism. This chapter has been previously published as Kaislaniemi L., van Hunen J., Allen M. B., Neill I. (2014). *Sub-lithospheric small-scale convection—a mechanism for collision zone magmatism.* Geology, 42 (4). DOI:10.1130/G35193.1.

Chapter 4 continues examination of small-scale convection processes, and studies how a lithospheric thickness gradient can produce surface uplift and mantle-derived volcanism. A parameter study is conducted and applied to the intra-continental orogeny of the Moroccan Atlas mountains. This chapter has been previously published as Kaislaniemi L. and van Hunen J. (2014). *Dynamics of lithospheric thinning and mantle melting by edge-driven convection: Application to Moroccan Atlas mountains.* Geochemistry, Geophysics, Geosystems, 15. DOI:10.1002/2014GC005414.

Chapter 5 studies the interaction between local lithospheric thinning and crustal anatexis. A new dynamically integrated model of crustal melting and mantle convection is presented and applied to the study of magmatism during orogenic collapse.

Chapter 6 summarises results from the three previous chapters and presents possible directions for future work.

References

Abers, G. A. (1991). "Possible seismogenic shallow-dipping normal faults in the Woodlark-D'Entrecasteaux extensional province, Papua New Guinea". In: *Geology* 19, pp. 1205–1208.

Allmendinger, R. W., T. E. Jordan, S. M. Kay, and B. L. Isacks (1997). "The evolution of the Altiplano-Puna Plateau of the Central Andes". In: *Annual Review of Earth and Planetary Sciences* 25, pp. 139–174.

Armijo, R. and P. Tapponnier (1986). "Quaternary extension in southern Tibet: Field observations and tectonic implications". In: *Journal of Geophysical Research* 91.B14, pp. 13803–13872.

Arndt, N. T. and S. L. Goldstein (1989). "An open boundary between lower continental crust and mantle : its role in crust formation and crustaf recycling". In: *Tectonophysics* 161, pp. 201–212.

Asimow, P. D. and C. H. Langmuir (2003). "The importance of water to oceanic mantle melting regimes". In: *Nature* 421, pp. 815–820.

Avigad, D. and Z. Gvirtzman (2009). "Late Neoproterozoic rise and fall of the northern Arabian-Nubian shield: The role of lithospheric mantle delamination and subsequent thermal subsidence". In: *Tectonophysics* 477.3-4, pp. 217–228.

Ballmer, M. D., J. van Hunen, G. Ito, T. A. Bianco, and P. J. Tackley (2009). "Intraplate volcanism with complex age-distance patterns: A case for small-scale sublithospheric convection". In: *Geochemistry, Geophysics, Geosystems* 10.Q06015.

Beck, S. L. and G. Zandt (2002). "The nature of orogenic crust in the central Andes". In: *Journal of Geophysical Research* 107.B10, p. 2230.

Bergman, T., H. Schöberg, and K. Sundblad (1995). "Geochemistry, age, and origin of the Högberget granite, western Bergslagen, Sweden". In: *GFF* 117.2, pp. 87–95.

Bird, P. (1979). "Continental Delamination and the Colorado Plateau". In: *Journal of Geophysical Research* 84.B13, pp. 7561–7571.

Black, R. and J.-P. Liégeois (1993). "Cratons, mobile belts, alkaline rocks and continental lithospheric mantle: the Pan-African testimony". In: *Journal of the Geological Society, London* 150, pp. 89–98.

Black, R., J. Lameyre, and B. Bonin (1985). "The structural setting of alkaline complexes". In: *Journal of African Earth Sciences* 3.1, pp. 5–16.

Bodorkos, S., M. Sandiford, N. H. Oliver, and P. A. Cawood (2002). "High- T , low- P metamorphism in the Palaeoproterozoic Halls Creek Orogen , northern Australia : the middle crustal response to a mantle-related transient thermal pulse". In: *Journal of Metamorphic Geology* 20, pp. 217–237.

Bonin, B. (2004). "Do coeval mafic and felsic magmas in post-collisional to within-plate regimes necessarily imply two contrasting, mantle and crustal, sources? A review". In: *Lithos* 78.1-2, pp. 1–24.

Bonin, B., A. Azzouni-Sekkal, F. Bussy, and S. Ferrag (1998). "Alkali-calcic and alkaline post-orogenic (PO) granite magmatism: petrologic constraints and geodynamic settings". In: *Lithos* 45, pp. 45–70.

Brown, M. (1994). "The generation, segregation, ascent and emplacement of granite magma: the migmatite-to-crustally-derived granite connection in thickened orogens". In: *Earth-Science Reviews* 36.1-2, pp. 83–130.

Buck, W. R. (1985). "When does small-scale convection begin beneath oceanic lithosphere?" In: *Nature* 33, pp. 775–777.

Burov, E. B. (2006). "The long-term strength of continental lithosphere: "jelly sandwich" or "crème brûlée"?" In: *GSA Today* 16.1, pp. 4–10.

Chopin, C. (2003). "Ultrahigh-pressure metamorphism: tracing continental crust into the mantle". In: *Earth and Planetary Science Letters* 212.1-2, pp. 1–14.

Chung, S.-L., D. Liu, J. Ji, M.-F. Chu, H.-Y. Lee, D.-J. Wen, C.-H. Lo, T.-Y. Lee, Q. Qian, and Q. Zhang (2003). "Adakites from continental collision zones: Melting of thickened lower crust beneath southern Tibet". In: *Geology* 31.11, p. 1021.

Chung, S.-L., M.-F. Chu, Y. Zhang, Y. Xie, C.-H. Lo, T.-Y. Lee, C.-Y. Lan, X. Li, Q. Zhang, and Y. Wang (2005). "Tibetan tectonic evolution inferred from spatial and temporal variations in post-collisional magmatism". In: *Earth-Science Reviews* 68.3-4, pp. 173–196.

Colgan, J. P., T. A. Dumitru, P. W. Reiners, J. L. Wooden, and E. L. Miller (2006). "Cenozoic Tectonic Evolution of the Basin and Range Province in Northwestern Nevada". In: *American Journal of Science* 306.8, pp. 616–654.

Dai, L. and S.-i. Karato (2009). "Electrical conductivity of orthopyroxene: Implications for the water content of the asthenosphere". In: *Proceedings of the Japan Academy. Series B, Physical and Biological Sciences* 85, pp. 466–475.

DeCelles, P. G., M. N. Ducea, P. Kapp, and G. Zandt (2009). "Cyclicity in Cordilleran orogenic systems". In: *Nature Geoscience* 2.4, pp. 251–257.

Delany, J. M. and H. C. Helgeson (1978). "Calculation of the thermodynamic consequences of dehydration in subducting oceanic crust to 100 kb and $>$ 800°C". In: *American Journal of Science* 278, pp. 638–686.

Dewey, J. F. (1988). "Extensional collapse of orogens". In: *Tectonics* 7.6, pp. 1123–1139.

Dilek, Y. and S. Altunkayanak (2007). "Cenozoic Crustal Evolution and Mantle Dynamics of Post-Collisional Magmatism in Western Anatolia". In: *International Geology Review* 49, pp. 431–453.

Dixon, J. E., T. H. Dixon, D. R. Bell, and R Malservisi (2004). "Lateral variation in upper mantle viscosity: role of water". In: *Earth and Planetary Science Letters* 222.2, pp. 451–467.

Doin, M.-P., L. Fleitout, and U. Christensen (1997). "Mantle convection and stability of depleted and undepleted continental lithosphere". In: *Journal of Geophysical Research* 102.B2, p. 2771.

Drew, S. T., M. N. Ducea, and L. M. Schoenbohm (2009). "Mafic volcanism on the Puna Plateau, NW Argentina: Implications for lithospheric composition and evolution with an emphasis on lithospheric foundering". In: *Lithosphere* 1.1993, pp. 305–318.

Ducea, M. N. (2011). "Fingerprinting orogenic delamination". In: *Geology* 39.2, pp. 191–192.

Ducea, M. N. (2002). "Constraints on the bulk composition and root foundering rates of continental arcs: A California arc perspective". In: *Journal of Geophysical Research* 107.B11, p. 2304.

Ducea, M. and J. Saleeby (1998). "A Case for Delamination of the Deep Batholithic Crust beneath the Sierra Nevada, California". In: *International Geology Review* 40.1, pp. 78–93.

Dumoulin, C., M.-P. Doin, and L. Fleitout (2001). "Numerical simulations of the cooling of an oceanic lithosphere above a convective mantle". In: *Physics of the Earth and Planetary Interiors* 125.1-4, pp. 45–64.

Elkins-Tanton, L. T. (2007). "Continental magmatism, volatile recycling, and a heterogeneous mantle caused by lithospheric gravitational instabilities". In: *Journal of Geophysical Research* 112.B03405.

England, P. C. and A. B. Thompson (1984). "Pressure-Temperature-Time Paths of Regional Metamorphism I. Heat Transfer during the Evolution of Regions of Thickened Continental Crust". In: *Journal of Petrology* 25.4, pp. 894–928.

England, P. and G. Houseman (1989). "Extension during continental convergence, with application to the Tibetan plateau". In: *Journal of Geophysical Research* 94.B12, pp. 17561–17579.

Faure, M., J.-M. Lardeaux, and P. Ledru (2009). "A review of the pre-Permian geology of the Variscan French Massif Central". In: *Comptes Rendus Geoscience* 341.2-3, pp. 202–213.

Fei, H., M. Wiedenbeck, D. Yamazaki, and T. Katsura (2013). "Small effect of water on upper-mantle rheology based on silicon self-diffusion coefficients". In: *Nature* 498.13 June, pp. 213–215.

Feldstein, S. N. and R. A. Lange (1999). "Pliocene Potassic Magmas from the Kings River Region, Sierra Nevada, California: Evidence for Melting of a Subduction-Modified Mantle". In: *Journal of Petrology* 40.8, pp. 1301–1320.

Fillerup, M. A., J. H. Knapp, C. C. Knapp, and V. Raileanu (2010). "Mantle earthquakes in the absence of subduction? Continental delamination in the Romanian Carpathians". In: *Lithosphere* 2.5, pp. 333–340.

Francois, T., E. Burov, P. Agard, and B. Meyer (2014). "Build-up of a dynamically supported orogenic plateau: numerical mdelling of the Zagros/Central Iran case study". In: *Geochemistry, Geophysics, Geosystems* 15.6, pp. 2632–2654.

Gögüs, O. H. and R. N. Pysklywec (2008). "Mantle lithosphere delamination driving plateau uplift and synconvergent extension in eastern Anatolia". In: *Geology* 36.9, pp. 723–726.

Gök, R., M. E. Pasyanos, and E. Zor (2007). "Lithospheric structure of the continent-continent collision zone: eastern Turkey". In: *Geophysical Journal International* 169.3, pp. 1079–1088.

Guo, Z. (2006). "Post-collisional, Potassic and Ultrapotassic Magmatism of the Northern Tibetan Plateau: Constraints on Characteristics of the Mantle Source, Geodynamic Setting and Uplift Mechanisms". In: *Journal of Petrology* 47.6, pp. 1177–1220.

Gutiérrez-Alonso, G., S. T. Johnston, A. B. Weil, D. Pastor-Galán, and J. Fernández-Suárez (2012). "Buckling an orogen: The Cantabrian Orocline". In: *GSA Today* 22.7, pp. 4–9.

Hernlund, J. W., P. J. Tackley, and D. J. Stevenson (2008). "Buoyant melting instabilities beneath extending lithosphere: 1. Numerical models". In: *Journal of Geophysical Research* 113.B4, B04405.

Hirschmann, M. M., C. Aubaud, and A. C. Withers (2005). "Storage capacity of H2O in nominally anhydrous minerals in the upper mantle". In: *Earth and Planetary Science Letters* 236.1-2, pp. 167–181.

Hirth, G. and D. L. Kohlstedt (1996). "Water in the oceanic upper mantle: implications for rheology, melt extraction and the evolution of the lithosphere". In: *Earth and Planetary Science Letters* 144, pp. 93–108.

Hirth, G. and J. Tullis (1994). "The brittle-plastic transition in experimentally deformed quartz aggregates". In: *Journal of Geophysical Research* 99.B6, p. 11731.

Houseman, G. A., D. P. Mckenzie, and P. Molnar (1981). "Convective instability of a thickened boundary layer and its relevance for the thermal evolution of continental convergent belts". In: *Journal of Geophysical Research* 86.B7, pp. 6115–6132.

Houseman, G. A. and P. Molnar (1997). "Gravitational (Rayleigh-Taylor) instability of a layer with non-linear viscosity and convective thinning of continental lithosphere". In: *Geophysical Journal International* 128, pp. 125–150.

Huang, J. (2005). "Sublithospheric small-scale convection and its implications for the residual topography at old ocean basins and the plate model". In: *Journal of Geophysical Research* 110.B5, B05404.

Iwamori, H. (1997). "Compression melting in subduction zones". In: *Terra Nova* 9, pp. 9–13.

Jackson, J. A., H. Austrheim, D. McKenzie, and K. Priestley (2004). "Metastability, mechanical strength, and the support of mountain belts". In: *Geology* 32.7, p. 625.

Jackson, J. (2002). "Strength of the continental lithosphere: Time to abandon the jelly sandwich?" In: *GSA Today* 12.9, pp. 5–9.

Jackson, J., J. Haines, and W. Holt (1992). "The Horizontal Velocity Field in the Deforming Aegean Sea Region Determined From the Moment Tensors of Earthquakes". In: *Journal of Geophysical Research* 97.B12, pp. 17657–17684.

Kaislaniemi, L, J van Hunen, M. B. Allen, and I Neill (2014). "Sublithospheric small-scale convection — A mechanism for collision zone magmatism". In: *Geology* 42.4, pp. 291–294.

Karato, S.-i. (2010). "Rheology of the deep upper mantle and its implications for the preservation of the continental roots: A review". In: *Tectonophysics* 481.1-4, pp. 82–98.

Kay, R. W. and S. Mahlburg-Kay (1991). "Creation and destruction of lower continental crust". In: *Geologische Rundschau* 80.2, pp. 259–278.

Kay, R. and S. Mahlburg Kay (1993). "Delamination and delamination magmatism". In: *Tectonophysics* 219.1-3, pp. 177–189.

Kelbert, A., A. Schultz, and G. Egbert (2009). "Global electromagnetic induction constraints on transition-zone water content variations." In: *Nature* 460.7258, pp. 1003–6.

Kelley, K. A., T. Plank, T. L. Grove, E. M. Stolper, S. Newman, and E. Hauri (2006). "Mantle melting as a function of water content beneath back-arc basins". In: *Journal of Geophysical Research* 111.B9, B09208.

Keskin, M. (2003). "Magma generation by slab steepening and breakoff beneath a subduction-accretion complex: An alternative model for collision-related volcanism in Eastern Anatolia, Turkey". In: *Geophysical Research Letters* 30.24, pp. 7–10.

Knapp, J. H., C. C. Knapp, V. Raileanu, L. Matenco, V. Mocanu, and C. Dinu (2005). "Crustal constraints on the origin of mantle seismicity in the Vrancea Zone, Romania: The case for active continental lithospheric delamination". In: *Tectonophysics* 410.1-4, pp. 311–323.

Kohlstedt, D. L., H. Keppler, and D. C. Rubie (1996). "Solubility of water in the α, β and γ phases of $(\mathrm{Mg,Fe})_2\mathrm{SiO}_4$". In: *Contrib Mineral Petrol* 123, pp. 345–357.

Korja, A., T. Korja, U. Luosto, and P. Heikkinen (2009). "Seismic and geoelectric evidence for collisional and extensional events in the Fennoscandian Shield — implications for Precambrian crustal evolution". In: *Tectonophysics* 219, pp. 129–152.

Krystopowicz, N. J. and C. A. Currie (2013). "Crustal eclogitization and lithosphere delamination in orogens". In: *Earth and Planetary Science Letters* 361, pp. 195–207.

Kukkonen, I. and L. Lauri (2009). "Modelling the thermal evolution of a collisional Precambrian orogen: High heat production migmatitic granites of southern Finland". In: *Precambrian Research* 168.3-4, pp. 233–246.

Lang Farmer, G., A. F. Glzner, and C. R. Manley (2002). "Did lithospheric delamination trigger late Cenozoic potassic volcanism in the southern Sierra Nevada, California?" In: *Geological Society of America Bulletin* 114.6, pp. 754–768.

Lange, R. A., I. S. E. Carmichael, and P. R. Renne (1993). "Potassic volcanism near Mono basin, California: Evidence for high water and oxygen fugacities inherited from subduction". In: *Geology* 21, pp. 949–952.

Le Pourhiet, L., M. Gurnis, and J. Saleeby (2006). "Mantle instability beneath the Sierra Nevada Mountains in California and Death Valley extension". In: *Earth and Planetary Science Letters* 251.1-2, pp. 104–119.

Lee, C.-T. A., X. Cheng, and U. Horodyskyj (2006). "The development and refinement of continental arcs by primary basaltic magmatism, garnet pyroxenite accumulation, basaltic recharge and delamination: insights from the Sierra Nevada, California". In: *Contributions to Mineralogy and Petrology* 151.2, pp. 222–242.

Leech, M. L. (2001). "Arrested orogenic development: eclogitization, delamination, and tectonic collapse". In: *Earth and Planetary Science Letters* 185.1-2, pp. 149–159.

Lenardic, A. and L.-N. Moresi (1999). "Some thoughts on the stability of cratonic lithosphere: Effects of buoyancy and viscosity". In: *Journal of Geophysical Research* 104.B6, p. 12747.

Liégeois, J.-P. (1998). "Preface — Some words on the post-collisional magmatism". In: *Lithos* 45, pp. xv–xvii.

Liégeois, J.-P., J. Navez, J. Hertogen, and R. Black (1998). "Contrasting origin of post-collisional high-K calc-alkaline and shoshonitic versus alkaline and peralkaline granitoids. The use of sliding normalization". In: *Lithos* 45, pp. 1–28.

Mahlburg Kay, S., B. Coira, and J. Viramonte (1994). "Young mafic back arc volcanic rocks as indicators of continental lithospheric delamination beneath the Argentine Puna plateau, central Andes". In: *Journal of Geophysical Research* 99.B12, pp. 24323–24339.

Maruyama, S. and K. Okamoto (2007). "Water transportation from the subducting slab into the mantle transition zone". In: *Gondwana Research* 11, pp. 148–165.

Mei, S. and D. Kohlstedt (2000). "Influence of water on plastic deformation of olivine aggregates 1 . Diffusion creep regime". In: *Journal of Geophysical Research* 105, pp. 21457–21469.

Mei, S., W. Bai, T. Hiraga, and D. Kohlstedt (2002). "Influence of melt on the creep behavior of olivine-basalt aggregates under hydrous conditions". In: *Earth and Planetary Science Letters* 201.3-4, pp. 491–507.

Meissner, R. and J. Strehlau (1982). "Limits of stresses in continental crusts and their relation to the depth-frequency distribution of shallow earthquakes". In: *Tectonics* 1.1, pp. 73–89.

Meissner, R. and W. Mooney (1998). "Weakness of the lower continental crust: a condition for delamination, uplift, and escape". In: *Tectonophysics* 296.1-2, pp. 47–60.

Molnar, P., P. England, and J. Martinod (1993). "Mantle dynamics, uplift of the Tibetan plateau and the Indian monsoon". In: *Reviews of Geophysics* 31.4, pp. 357–396.

Morency, C. and M.-P. Doin (2004). "Numerical simulations of the mantle lithosphere delamination". In: *Journal of Geophysical Research* 109.B3, B03410.

Morency, C., M.-P. Doin, and C. Dumoulin (2002). "Convective destabilization of a thickened continental lithosphere". In: *Earth and Planetary Science Letters* 202.2, pp. 303–320.

Mouthereau, F. (2011). "Timing of uplift in the Zagros belt/Iranian plateau and accommodation of late Cenozoic Arabia-Eurasia convergence". In: *Geological Magazine* 148.5-6, pp. 726–738.

Nelson, K. D. (1992). "Are crustal thickness variations in old mountain belts like the Appalachians a consequence of lithospheric delamination?" In: *Geology* 20, pp. 498–502.

Niu, Y., Z. Zhao, D.-C. Zhu, and X. Mo (2013). "Continental collision zones are primary sites for net continental crust growth - A testable hypothesis". In: *Earth-Science Reviews* 127, pp. 96–110.

Pearson, D. G., F. E. Brenker, F. Nestola, J. McNeill, L. Nasdala, M. T. Hutchison, S. Matveev, K. Mather, G. Silversmit, S. Schmitz, et al. (2014). "Hydrous mantle transition zone indicated by ringwoodite included within diamond." In: *Nature* 507.7491, pp. 221–4.

Petford, N. and K. Gallagher (2001). "Partial melting of mafic (amphibolitic) lower crust by periodic influx of basaltic magma". In: *Earth and Planetary Science Letters* 193, pp. 483–499.

Platt, J. P. and P. C. England (1993). "Convective removal of lithosphere beneath mountain belts: Thermal and mechanical consequences". In: *American Journal of Science* 293, pp. 307–336.

Poudjom Djomani, Y. H., S. Y. O'Reilly, W. L. Griffin, and P. Morgan (2001). "The density structure of subcontinental lithosphere through time". In: *Earth and Planetary Science Letters* 184, pp. 605–621.

Rey, P. (1993). "Seismic and tectonometamorphic characters of the lower continentan crust in Phanerozoic areas: a consequence of post-thickening extension". In: *Tectonics* 12.2, pp. 580–590.

Rudnick, R. L. and D. M. Fountain (1995). "Nature and composition of the continental crust: a lower crustal perspective". In: *Reviews of Geophysics* 33.3, pp. 267–309.

Saal, A. E., E. H. Hauri, C. H. Langmuir, and M. R. Perfit (2002). "Vapour undersaturation in primitive mid-ocean-ridge basalt and the volatile content of Earth's upper mantle". In: *Nature* 419, pp. 451–455.

Schurr, B., A. Rietbrock, G. Asch, R. Kind, and O. Oncken (2006). "Evidence for lithospheric detachment in the central Andes from local earthquake tomography". In: *Tectonophysics* 415.1-4, pp. 203–223.

Sederholm, J. J. (1934). "On migmatites and associated pre-Cambrian rocks of southwestern Finland: Part III. The Åland Islands". In: *Bulletin de la Commission géologique de Finlande* 107, pp. 1–68.

Singh, S. C. and D. McKenzie (1993). "Layering in the lower crust". In: *Geophysical Journal International* 113.3, pp. 622–628.

Sleep, N. H. (2005). "Evolution of the Continental Lithosphere". In: *Annual Review of Earth and Planetary Sciences* 33.1, pp. 369–393.

– (2011). "Small-scale convection beneath oceans and continents". In: *Chinese Science Bulletin* 56.13, pp. 1292–1317.

Smyth, J. R. (1987). "β-Mg_2SiO_4: A potential host for water in the mantle?" In: *American Mineralogist* 72, pp. 1051–1055.

Solomatov, V. S. and L.-N. Moresi (2000). "Scaling of time-dependent stagnant lid convection: Application to small-scale convection on Earth and other terrestrial planets". In: *Journal of Geophysical Research* 105.B9, pp. 21795–21817.

Spencer, J. E. (1996). "Uplift of the Colorado Plateau due to lithosphere attenuation during Laramide low-angle subduction of about calculations". In: *Journal of Geophysical Research* 101.B6, pp. 13595–13609.

Sylvester, P. J. (1989). "Post-Collisional Alkaline Granites". In: *The Journal of Geology* 97.3, pp. 261–280.

– (1998). "Post-collisional strongly peraluminous granites". In: *Lithos* 45.1-4, pp. 29–44.

Tatsumi, Y., D. L. Hamilton, and R. W. Nesbitt (1986). "Chemical characteristics of fluid phase released from a subducted lithosphere and origin of arc magmas: Evidence from high-pressure experiments and natural rocks". In: *Journal of Volcanology and Geothermal Research* 29, pp. 293–309.

Thompson, A. B. and J. A. D. Connolly (1995). "Melting of the continental crust: Some thermal and petrological constraints on anatexis in continental collision zones and other tectonic settings". In: *Journal of Geophysical Research* 100.B8, pp. 15565–15579.

Thompson, A. B. (1992). "Water in the Earth's upper mantle". In: *Nature* 358, pp. 295–302.

Turcotte, D. L. and G. Schubert (2001). *Geodynamics*. 2nd ed. New York: Cambridge University Press, 456 p.

Väisänen, M., I. Mänttäri, L. M. Kriegsman, and P. Hölttä (2000). "Tectonic setting of post-collisional magmatism in the Palaeoproterozoic Svecofennian Orogen, SW Finland". In: *Lithos* 54, pp. 63–81.

Vanderhaeghe, O. and C. Teyssier (2001). "Crustal-scale rheological transitions during late-orogenic collapse". In: *Tectonophysics* 335.1-2, pp. 211–228.

Wang, D., M. Mookherjee, Y. Xu, and S.-i. Karato (2006). "The effect of water on the electrical conductivity of olivine." In: *Nature* 443.7114, pp. 977–80.

Wang, H. L., J. van Hunen, D. G. Pearson, and M. B. Allen (2014). "Craton stability and longevity : the roles of composition-dependent rheology and buoyancy". In: *Earth and Planetary Science Letters* 391, pp. 224–233.

Wells, M. L. and T. D. Hoisch (2008). "The role of mantle delamination in widespread Late Cretaceous extension and magmatism in the Cordilleran orogen, western United States". In: *Geological Society of America Bulletin* 120.5-6, pp. 515–530.

Williams, H. M. (2004). "Nature of the Source Regions for Post-collisional, Potassic Magmatism in Southern and Northern Tibet from Geochemical Variations and Inverse Trace Element Modelling". In: *Journal of Petrology* 45.3, pp. 555–607.

Ye, K., B. Cong, and D. Ye (2000). "The possible subduction of continental material to depths greater than 200 km". In: *Nature* 407, pp. 734–736.

Yuen, D. A. and L. Fleitout (1985). "Thinning of the lithosphere by small-scale convective destabilization". In: *Nature* 313, pp. 125–128.

Zandt, G., H. Gilbert, T. J. Owens, M. Ducea, J. Saleeby, and C. H. Jones (2004). "Active foundering of a continental arc root beneath the southern Sierra Nevada in California". In: *Nature* 431, pp. 41–46.

Zhu, H., E. Bozdag, T. S. Duffy, and J. Tromp (2013). "Seismic attenuation beneath Europe and the North Atlantic: Implications for water in the mantle". In: *Earth and Planetary Science Letters* 381, pp. 1–11.

Zuber, M. T. (1994). "Folding a jelly sandwich". In: *Nature* 371, pp. 650–651.

van Hunen, J. and M. B. Allen (2011). "Continental collision and slab break-off: A comparison of 3-D numerical models with observations". In: *Earth and Planetary Science Letters* 302.1-2, pp. 27–37.

Chapter 2

Methods

2.1 Governing equations for mantle convection

2.1.1 Continuity and Stokes equation

The basic equations describing the convection in the Earth's mantle are the conservation of mass, momentum and energy in a fluid continuum (Schubert et al., 2001). For a infinitesimal volume element, the equation for the conservation of mass is

$$\frac{\partial}{\partial x_i}(\rho u_i) + \frac{\partial \rho}{\partial t} = 0\,, \tag{2.1}$$

where $\mathbf{x}$ is the position vector[1], $\mathbf{u}$ is the velocity, ρ the density, and t the time. This states that the net flow of mass in and out of the infinitesimal volume element should be compensated by a change in the density of the material. Earth's mantle is often assumed incompressible, $\frac{\partial \rho}{\partial t} = 0$, so that the equation simplifies to

$$\frac{\partial u_i}{\partial x_i} = 0\,. \tag{2.2}$$

The equation for conservation of momentum, the fluid mechanical analogue to Newton's second law of motion, is

$$\rho \frac{Du_i}{Dt} = -\frac{\partial p}{\partial x_i} + \frac{\partial \tau_{ij}}{\partial x_j} + \rho g_i\,, \tag{2.3}$$

where p is the fluid pressure, τ_{ij} the deviatoric stress tensor, and g_i the acceleration of gravity. This is also known as the Navier-Stokes equation for incompressible fluid. The term on the left is the product of the fluid mass and acceleration. The two first terms on the right are the surface forces (normal and shear stresses) working on the infinitesimal fluid volume, and the third term

[1] Cartesian tensor notation (Einstein summation convention) is used here, so that repeated subscripts implies a summation over the spatial directions ($i = 1, 2$ or $i = 1, 2, 3$)

on the right is the body force working on the fluid volume. Here, only acceleration of gravity is considered.

For mantle convection, the inertia forces are negligible compared to the gravitational force, i.e. changes in kinetic energy are very small (Schubert et al., 2001). Thus, gravitational forces dominate over inertia and the first term in the Navier-Stokes equation can be equated to zero, $\rho\frac{Du_i}{Dt} = 0$. This means that all the forces acting upon a volume of mantle are immediately in balance. This non-time-dependent version of the Navier-Stokes equation is called the Stokes equation, and the approximation where density differences are neglected except when multiplied by the acceleration of gravity g_i is called the Boussinesq approximation.

To make use of equation (2.3) the deviatoric stress τ_{ij} has to be related to the velocities or the strain rates that produce it:

$$\tau_{ij} = f(\dot{\epsilon}_{ij})\,, \tag{2.4}$$

The strain rate is defined as

$$\dot{\boldsymbol{\epsilon}} = \nabla\mathbf{u} + (\nabla\mathbf{u})^T \quad \text{or} \quad \dot{\epsilon}_{ij} = \frac{\partial u_i}{\partial x_j} + \frac{\partial u_j}{\partial x_i}\,. \tag{2.5}$$

If the strain rate to deviatoric stress relationship is a linear one, the fluid is said to be Newtonian and dominating creep mechanism is the diffusion creep. In this case, and assuming the material is isotropic and incompressible,

$$\tau_{ij} = \eta\dot{\epsilon}_{ij} = \eta\left(\frac{\partial u_i}{\partial x_j} + \frac{\partial u_j}{\partial x_i}\right)\,, \tag{2.6}$$

where η is the dynamic viscosity. For a non-linear relationship in (2.4), the fluid is said to be non-Newtonian and dislocation creep is the dominant creep mechanism. In this case,

$$\tau_{ij}^n = A_{\text{eff}}^{-1}\dot{\epsilon}_{ij}\,. \tag{2.7}$$

The proportionality constant A_{eff}^{-1} is analogous to the viscosity in Newtonian case but does not have the units of Pa s. The exponent n is usually between 2 and 5 for most rocks. The viscosity and the parameter A_{eff}^{-1} may be a function of number of material properties and, most notably, of temperature and pressure.

In order to experiment and parameterize rock rheology, second invariants of the deviatoric stress (effective shear stress) and strain rate are used:

$$\sigma_{II} = \sqrt{\frac{1}{2}\left(\tau_{ij}\tau_{ij} - \tau_{ii}\tau_{jj}\right)}\,, \tag{2.8}$$

$$\dot{\epsilon}_{II} = \sqrt{\frac{1}{2}\left(\dot{\epsilon}_{ij}\dot{\epsilon}_{ij} - \dot{\epsilon}_{ii}\dot{\epsilon}_{jj}\right)}\,. \tag{2.9}$$

(Note that for deviatoric stress tensor $\tau_{ii} = 0$.) With these, the effective viscosity can be defined

$$\eta_{eff} = \frac{\sigma_{II}}{\dot{\epsilon}_{II}} \,. \tag{2.10}$$

Different flow laws, relating these three quantities, are discussed in section 2.1.4.

2.1.2 Conservation of energy

The conservation of energy equation is derived from the second law of thermodynamics and describes the balance between energy in different forms within an elemental fluid volume (Schubert et al., 2001):

$$\rho T \frac{Ds}{Dt} = \tau_{ij} \frac{\partial u_i}{\partial x_j} + \frac{\partial}{\partial x_i} \left(k \frac{\partial T}{\partial x_i} \right) + \rho H + \Phi \,, \tag{2.11}$$

where T is the temperature, s is the specific entropy, k is the thermal conductivity, and H is the rate of internal heat production per unit mass. In order from left to right, the terms correspond to the rate of change of the specific entropy, heat production rate due to viscous dissipation, thermal conduction, and internal heat generation due to radioactive decay, and finally, ϕ, the rate of heat production or consumption by phase changes, e.g. melting. The change in specific entropy can be expressed as

$$\frac{Ds}{Dt} = \left(\frac{\partial s}{\partial T} \right)_p \frac{DT}{Dt} + \left(\frac{\partial s}{\partial p} \right)_T \frac{Dp}{Dt} \,, \tag{2.12}$$

and further, with more familiar thermodynamic quantities,

$$\frac{Ds}{Dt} = \frac{C_p}{T} \frac{DT}{Dt} - \frac{\alpha}{\rho} \frac{Dp}{Dt} \,, \tag{2.13}$$

where $C_p = T \left(\frac{\partial s}{\partial T} \right)_p$ is the constant pressure heat capacity and $\alpha = -\frac{1}{\rho} \left(\frac{\partial \rho}{\partial T} \right)_p = \frac{1}{v} \left(\frac{\partial v}{\partial T} \right)_p$ the coefficient of thermal expansion. Substituting (2.13) into (2.11) gives

$$\rho C_p \frac{DT}{Dt} - \alpha T \frac{Dp}{Dt} = \frac{\partial}{\partial x_i} \left(k \frac{\partial T}{\partial x_i} \right) + \tau_{ij} \frac{\partial u_i}{\partial x_j} + \rho H + \Phi \,. \tag{2.14}$$

From definitions of α and C_p and thermodynamic relation $\left(\frac{\partial s}{\partial v} \right)_p = \left(\frac{\partial p}{\partial T} \right)_s$

$$\frac{\alpha T}{\rho C_p} = \left(\frac{\partial T}{\partial p} \right)_s \,. \tag{2.15}$$

Substituting this into (2.14) leads to

$$\rho C_p \left(\frac{DT}{Dt} - \left(\frac{\partial T}{\partial p} \right)_s \frac{Dp}{Dt} \right) = \frac{\partial}{\partial x_i} \left(k \frac{\partial T}{\partial x_i} \right) + \tau_{ij} \frac{\partial u_i}{\partial x_j} + \rho H + \Phi \,. \tag{2.16}$$

The second term inside the parentheses on the left is the rate of the temperature change due to adiabatic compression or expansion. In the absence of internal heat sources and heat exchange with the surroundings, the total change of the temperature is

$$\left(\frac{DT}{Dt}\right)_s = \left(\frac{\partial T}{\partial p}\right)_s \frac{Dp}{Dt} = \frac{\alpha T}{\rho C_p}\frac{Dp}{Dt}\,. \tag{2.17}$$

The adiabatic gradient, γ, can be derived from this by using the hydrostatic relation $\frac{\partial p}{\partial x_i} = \rho g_i$:

$$\gamma = \left(\frac{\partial T}{\partial x_i}\right)_s = \frac{\alpha T g_i}{C_p}\,. \tag{2.18}$$

2.1.3 Extendend Boussinesq approximation, non-dimensionalization

To solve the above discussed equations of incompressible fluid flow with infinite Prandtl number (very large ratio of kinematic viscosity and thermal diffusion) and so called extended Boussinesq approximation (Boussinesq approximation for buoyancy driven flow with additional terms to take into account the energy effects of adiabatic heating, latent heat of phase changes and frictional heating, Christensen and Yuen, 1985) equations (2.2), (2.3) and (2.14) are non-dimensionalized to take following forms:

$$\nabla \cdot \mathbf{u} = 0\,, \tag{2.19}$$

$$-\nabla \cdot p + \nabla \cdot [\eta(\nabla \mathbf{u} + \nabla^T \mathbf{u})] = -RaT \cdot \mathbf{e}_z + RbC \cdot \mathbf{e}_z\,, \tag{2.20}$$

$$\frac{\partial T}{\partial t} + \mathbf{u} \cdot \nabla T = \nabla^2 T + \frac{Di}{Ra}\eta\dot{\epsilon}^2 + \gamma \mathbf{u}_z + \rho H + \Phi\,, \tag{2.21}$$

where Ra is the thermal Rayleigh number, η viscosity, $\mathbf{e}_z$ unit vector in vertical direction, Rb compositional Rayleigh number, C compositional buoyancy, Di dissipation number, and $\dot{\epsilon}$ the strain rate. The non-dimensionalization of the physical quantities used in solving these equations are shown in Table 2.1. The dimensionless parameters used above are defined as

$$Ra = \frac{\alpha \Delta T \rho_0 g h^3}{\kappa \eta_0}\,, \tag{2.22}$$

$$Rb = \frac{\rho_0 g h^3}{\kappa \eta_0}\,, \tag{2.23}$$

$$Di = \frac{\alpha g h}{C_p}\,, \tag{2.24}$$

where ΔT is the difference between reference mantle (potential) temperature and surface temperature, h the model domain height, $\kappa = k/\rho C_p$ heat diffusivity, η_0 reference viscosity, and ρ_0 the reference density.

The compositional buoyancy takes into account the density differences caused by melt depletion and inherent material properties:

$$C = (\Delta\rho_F - 1) + \left(\frac{\rho_M}{\rho_0} - 1\right), \qquad (2.25)$$

where $\Delta\rho_F$ is the density change caused by melt depletion and ρ_M is the density of the rock in question.

Density decrease in mantle rocks due to melt depletion is parameterized as (Schutt and Lesher, 2006):

$$t = t'\frac{h^2}{\kappa} \quad L = L'\Delta T C_p \quad \gamma = \gamma'\frac{\Delta T}{h}$$
$$u = u'\frac{\kappa}{h} \quad p = p'\frac{\kappa}{h^2}\eta_0 \quad \eta = \eta'\eta_0$$
$$z = z'h \quad T = T'\Delta T$$

Table 2.1: The non-dimensionalized physical quantities used when numerically solving equations (2.19), (2.20) and (2.21). The non-dimensional quantities are marked with a prime, left out in the text for clarity.

$$\frac{\mathrm{d}\ln\rho}{\mathrm{d}F_{\mathrm{tot},\%}} = a_{\mathrm{depl}}\,, \qquad (2.26)$$

where $a_{\mathrm{depl}} < 0$ is a pressure dependent parameter and $F_{\mathrm{tot},\%} = 100F_{\mathrm{tot}}$ (cf Fig. 2.1). F_{tot} is the total depletion parameter, describing how big proportion of extractable melt has been produced and extracted from the rock during its whole history ($F_{\mathrm{tot}} = 0$ corresponding to fertile, unmolten and undepleted rock, $F_{\mathrm{tot}} = 0.1$ corresponding to a rock from which 10% has been extracted as melt, etc. See details in section 2.3.1). We simplify the equation by taking a_{depl} as a constant, applicable at the depth of interest (about 3 GPa), which leads to

$$\Delta\rho_F = \exp(100 a_{\mathrm{depl}} F_{\mathrm{tot}})\,. \qquad (2.27)$$

which is the non-dimensional ratio between the densities of undepleted and depleted rock, and is used in eq. (2.25) to calculate the effect of depletion on compositional buoyancy. The equation 2.26 is derived from experimental results, and, in effect, describes the depletion of the residue in Al_2O_3, which again controls the stability of the heavy mineral garnet (Niu et al., 2003).

The material parameter ρ_M in eq. (2.25) can be used to impose different densities due to lithological differences, e.g. rocks of crustal or mantle densities.

Heat consumption due to phase changes in Eq. (2.21) is caused by melting of the rock and consumption of the latent heat of fusion:

$$\Phi = \frac{DT_{\mathrm{fusion}}}{Dt}/\Delta T = \frac{D\left(\frac{LmF}{\Delta T C_p m}\right)}{Dt} = \frac{L}{C_p\Delta T}\frac{DF}{Dt}\,, \qquad (2.28)$$

where F_t is the amount of melt produced in one time step (not necessarily extracted), m is the mass of the finite volume of the rock and L is the specific heat of fusion, and ΔT is used for non-dimensionalization (i.e. directly in non-dimensional form: $\Phi = L'\frac{DF}{Dt}$ where L' is from Table 2.1).

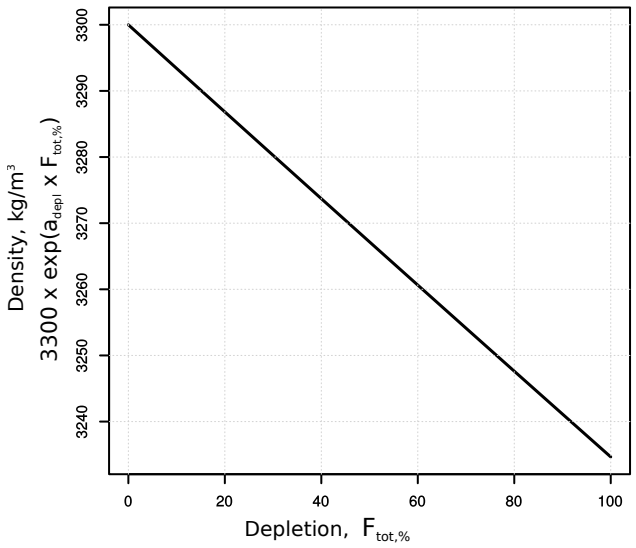

Figure 2.1: Depletion-buoyancy relationship from eq. (2.27). The density ratio $\Delta\rho_F$ on the vertical axis has been multiplied by 3300 $\mathrm{kg/m^3}$ to demonstrate the density values produced by the depletion of mantle rock.

2.1.4 Mantle rheology

Whether governed by diffusion creep or dislocation creep (Newtonian or non-Newtonian rheology), the flow law of mantle rock is usually expressed in form (Karato, 2010):

$$\dot{\epsilon} = Ad^m \tau^n \exp\left(-\frac{E+pV}{RT_{\mathrm{abs}}}\right), \tag{2.29}$$

where A is a pre-exponential factor, a material constant insensitive to thermo-mechanical conditions, d grain size, m grain size exponent, n the stress exponent (cf. eq. (2.7)), E activation energy, V activation volume, R the gas constant and $T_{\mathrm{abs}} = T + 273\,(\mathrm{K})$ the absolute temperature. Assuming isotropic material stress and strain rate tensors can be replaced by their second invariants (eq. (2.8) and (2.9)) which are scalar values. This assumption is used in solving the Stokes equation. The grain size exponent in (2.29) is $m = 0$ for dislocation creep. In diffusion creep, the grain size and its exponent might be incorporated into the material constant, $A_* = Ad^m$. Activation energy defines the temperature dependency and activation volume the pressure dependency of the viscosity.

Using definition for effective viscosity (2.10)

$$\eta_{\mathrm{eff}} = A_*^{-\frac{1}{n}} \dot{\epsilon}_{II}^{\frac{1-n}{n}} \exp\left(\frac{E+pV}{nRT}\right). \tag{2.30}$$

For Newtonian case $n = 1$ and the strain rate vanishes. The effective viscosity can then be expressed in terms of reference state

$$\eta_{\mathrm{eff}} = \eta_0 \exp\left(\frac{E+pV}{RT_{\mathrm{abs}}}\right) \exp\left(-\frac{E+p_0V}{RT_{\mathrm{abs},0}}\right), \tag{2.31}$$

where p_0 and $T_{\mathrm{abs},0} = \Delta T + 273\,(\mathrm{K})$ are the reference pressure and temperature (K) at which conditions $\eta_{\mathrm{eff}} = \eta_0$. These reference state conditions are a mathematical device useful for non-dimensionalization of the governing equations (2.19-2.21). However, such P-T-conditions might

not exist anywhere in the model. This is especially true for extended Boussinesq approximation where adiabatic heating is applied and the reference temperature is usually taken as the mantle potential temperature and reference pressure as the pressure at the bottom of the model domain.

Dislocation creep, non-Newtonian rheology, is an important deformation mechanism in the upper mantle (Schubert et al., 2001). However, because it introduces strong non-linearities in the Stokes equation (2.3), we have used an approach where the non-linearity of the viscosity is mimicked by using Newtonian rheology with a low activation energy value. This is shown to provide valid results at shallow level of the mantle, the lithosphere-asthenosphere boundary, where the interest of our study mainly lies. Christensen (1984) showed that multiplying the activation enthalpy ($H = E + pV$) value of the Newtonian rheology formulation by a factor $\beta < 1$ produces similar steady state convection patterns than a nonlinear rheology with normal activation enthalpy. For temperature dominated rheology (high E/V), such as used in our models, Christensen (1984) suggests that $0.3 \lessapprox \beta \lessapprox 0.5$. Van Hunen et al. (2005) studied the initiation of small-scale convection underneath oceanic lithosphere and found that using Newtonian rheology with activation energy $E = 120\,\mathrm{kJ/mol}$ results in similar amounts of thermomechanical erosion of the lithosphere bottom as in case of non-linear rheology with $E = 540\,\mathrm{kJ/mol}$. It was also shown (van Hunen et al., 2005), that the onset time of the sub-lithospheric small-scale convection below a lithosphere growing in to its steady-state thickness is similar in both Newtonian and non-Newtonian cases. The non-Newtonian rheology, however, produced stronger initial deformation than the Newtonian case (i.e. more punctuated instabilities). From technical point of view, using low activation energy has an advantage over non-linear rheology by making it computationally easier to find the long-term steady state solutions we have used as initial conditions in all our models, and by significantly decreasing the computation time needed for the parameter studies run.

2.1.5 Effect of water on mantle rheology

Mantle water content affects its viscosity. An usual parameterization for deformation of hydrous olivine is

$$\dot{\epsilon}_{\mathrm{hydr}} = f^r_{\mathrm{H_2O}}(p,T)\dot{\epsilon}, \tag{2.32}$$

where $f_{\mathrm{H_2O}}$ is the water fugacity and $r \approx 1 \pm 0.3$ is a non-dimensional constant (Hirth and Kohlstedt, 2003). Often, a simplification that water fugacity is proportional to the olivine water content $f_{\mathrm{H_2O}} \propto C_{\mathrm{OH}}$ (i.e. that C_{OH} is constant) is used (Karato, 2010, see also discussion below). Together with the definition of the effective viscosity (2.10), this leads to

$$\eta_{C_{\mathrm{OH}},\mathrm{eff}} = A_*^{-\frac{1}{n}} C_{\mathrm{OH}}^{-r} \dot{\epsilon}_{II}^{\frac{1-n}{n}} \exp\left(\frac{E+pV}{nRT}\right). \tag{2.33}$$

We parameterize the effect of water on viscosity with an exponential relationship

$$\eta_{\mathrm{hydr,eff}} = W\eta_{\mathrm{eff}},\ W = 100^{\frac{-X_{\mathrm{H_2O}}}{X_{\mathrm{H_2O}}+a}}, \tag{2.34}$$

where $X_{\mathrm{H_2O}}$ is the bulk water content (wt ppm), proportional to the olivine water content, and a is a parameter controlling the sensitivity of viscosity to water content. This parameterization lowers

the viscosity by one order of magnitude when $X_{\mathrm{H_2O}} = a$. The advantage of this parameterization over eq. (2.33) is that the effective viscosity approaches the dry viscosity value when water content approaches zero,

$$\lim_{X_{\mathrm{H_2O}} \to 0} \eta_{\mathrm{hydr,eff}} = \eta_{\mathrm{dry,eff}} \,, \tag{2.35}$$

instead of approaching infinity, i.e.

$$\lim_{C_{\mathrm{OH}} \to 0} \eta_{C_{\mathrm{OH}},\mathrm{eff}} = \infty \,, \tag{2.36}$$

as is the case for parameterizations based on (2.33). In addition, it conforms to the boundary conditions set by experimental work: viscosity lowering is exponential and maximum viscosity lowering is about two orders of magnitude (Mei and Kohlstedt, 2000; Karato, 2010). The value of a is adjusted so that normal mantle background water contents do not cause significant viscosity lowering, i.e. a should be clearly larger than about 120 wt ppm which is a typical water content for mid-ocean ridge basalts (Dixon et al., 2004). On the other hand, increasing values of a, or, in general, values of a significantly outside the variation interval of $X_{\mathrm{H_2O}}$, causes the relationship to become more linear, thus violating the assumption of exponential decrease. Results from models using this parameterization (chapter 3) have shown that values of a between 200 and 500 wt ppm produce realistic asthenospheric viscosity values.

The correctness of the functional form of our parameterization can be examined by comparing it to experimental results on effect of water fugacity on viscosity and water solubility in mantle minerals. Our parameterization is in terms of bulk water content (in nominally anhydrous minerals of the mantle), but the experimentally found relationships are usually given in terms of water fugacity in olivine. Water concentration in olivine relates to the water fugacity as $f_{\mathrm{H_2O}} \propto C^{0.9}_{\mathrm{OH,ol}}$ (Kohlstedt et al., 1996). The relation between water concentration in olivine and the bulk water content depends on the partition coefficients between the mantle mineral phases olivine, garnet and the two pyroxenes (Hirschmann et al., 2005, and references therein). Assuming these partition coefficients do not have orders of magnitude variation within the upper mantle, one can relate

$$X_{\mathrm{H_2O}} \propto C_{\mathrm{OH,ol}}, \;\; f_{\mathrm{H_2O}} \propto X^{0.9}_{\mathrm{H_2O}}, \;\; \text{and finally } \eta \propto \left(X^{0.9}_{\mathrm{H_2O}}\right)^{-r} . \tag{2.37}$$

A suitable value for a can be found by plotting $W(X_{\mathrm{H_2O}})$ and $\left(X^{0.9}_{\mathrm{H_2O}}\right)^{-r}$ side by side (Fig 2.2) and comparing the form of the curves. This does not take into account uncertainties related to the values of proportionality constants in eq. (2.37).

2.1.6 Effect of melt on mantle rheology

The partial melts existing within the rock affect its viscosity by occupying spaces between grain boundaries and at the triple junctions. Experimental data (Mei et al., 2002) shows an empirical relationship between melt-affected $\dot{\epsilon}(\phi)$ and melt-absent $\dot{\epsilon}(0)$ strain rate, and melt content ϕ:

$$\dot{\epsilon}(\phi) = \dot{\epsilon}(0) \exp(\lambda \phi) \,, \tag{2.38}$$

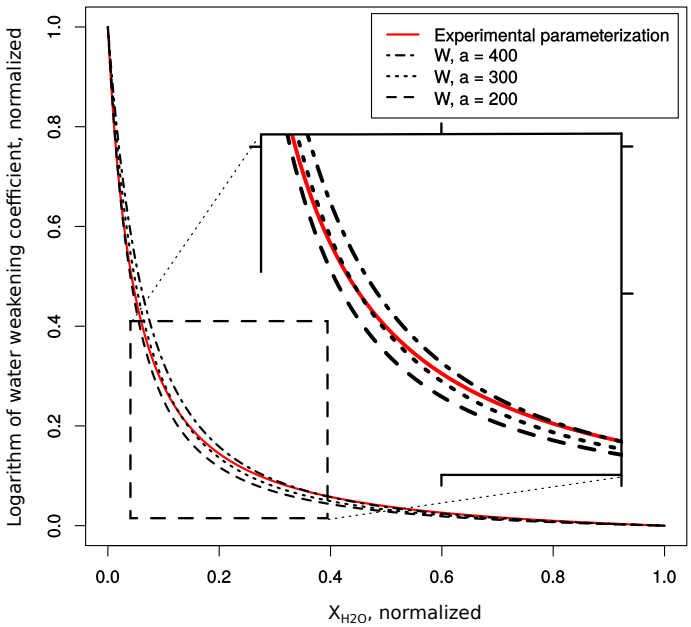

Figure 2.2: Comparison of the weakening effect of water, using experimental parameterization ($X_{\mathrm{H_2O}}$ vs $\left(X_{\mathrm{H_2O}}^{0.9}\right)^{-r}$, red line) and the parameterization used in this study (eq. (2.34), black lines, with different values of parameter a). Water content and weakening effects for both types of parameterizations are normalized to range from 0 to 1, so that no weakening (y=1) is assumed to take place at $X_{\mathrm{H_2O}} = 50\,\mathrm{ppm}$ (x=0) or less, and maximum weakening (y=0) is reached at $X_{\mathrm{H_2O}} = 1000\,\mathrm{ppm}$ (x=1).

where $\lambda \approx 26$ for diffusion creep and $\lambda \approx 31$ for dislocation creep. In models where melt weakening is taken into account, a Newtonian rheology is assumed, and the total effective viscosity is

$$\eta_{\mathrm{hydr},\phi,\mathrm{eff}} = \eta_0 W \exp\left(-\lambda_{\mathrm{diff}} F_t\right) \exp\left(\frac{E+pV}{RT_{\mathrm{abs}}}\right) \exp\left(-\frac{E+p_0 V}{RT_{\mathrm{abs},0}}\right), \tag{2.39}$$

where $F_t = \phi$ is the amount of melt produced during the time step t, and assumed to affect the rock viscosity for the duration of the time step (see also section 2.3.1 below).

2.2 Numerical methods for mantle convection

Finite element method has been a popular option for numerical mantle convection models because of its effectivity in handling complicated geometries and material properties. (e.g. Christensen, 1984; Bunge et al., 1997; van den Berg et al., 1992). We use the finite element code CitCom (Moresi and Gurnis, 1996; Zhong et al., 2000) because of its long-term development history and numerous previous applications to mantle convection modelling, and apply it in solving the Stokes flow (equations (2.19) and (2.20)) and the energy equation (2.21).

2.2.1 Finite element method

The finite element method is used to independently solve the Stokes flow with a Galerkin weak-form formulation (Hughes, 2000) and the energy equation with a streamline upwind Petrov-Galerkin formulation (Brooks, 1981).

The idea of the Galerkin weak formulation of the Stokes flow is to find the flow velocity $u_j = v_i + g_i$ and pressure P, such that $v_i \in \mathbf{V}$, $P \in \mathbf{P}$ and

$$\int_\Omega \frac{\partial w_i}{\partial x_j}\tau_{ij}\mathrm{d}\Omega - \int_\Omega q\frac{\partial u_i}{\partial x_i}\mathrm{d}\Omega = \int_\Omega w_i f_i \mathrm{d}\Omega + \sum_{i=1}^{n_{sd}} \int_{\Gamma_{h_i}} w_i h_i \mathrm{d}\Gamma \tag{2.40}$$

for all $w_i \in \mathbf{V}$ and $q \in \mathbf{P}$ (Zhong et al., 2009). $\mathbf{V}$ is a set of functions which are zero on the boundary Γ_{g_i}. The g_i are the velocities prescribed on this boundary, and h_i the forces prescribed on the boundary Γ_{h_i}. f_i are the body forces. The solution domain Ω is the discretized with a set of grid (nodal) points, which are used with so-called shape functions to interpolate the nodal points. The volumes defined by surrounding nodal points are called the elements. The set of functions derived from eq. (2.40) can be expressed in a matrix form

$$\begin{bmatrix} K & G \\ G^T & 0 \end{bmatrix} = \begin{Bmatrix} V \\ P \end{Bmatrix} = \begin{Bmatrix} F \\ 0 \end{Bmatrix}, \tag{2.41}$$

where vectors V and P contain the velocities and pressures at nodal and pressure points, respectively, vector F contains all the body and boundary forces, and matrices K, G, and G^T are the stiffness matrix, discrete gradient operator and discrete divergence operator, respectively.

To solve the matrix equation (2.41), Citcom uses the Uzawa algorithm (Moresi and Solomatov, 1995) in which the matrix equation is broken into two systems of equations

$$KV + GP = F \text{ and} \tag{2.42}$$

$$G^T V = 0\ , \tag{2.43}$$

which are then combined to eliminate V. This leaves the so called Schur complement system for pressure (Hughes, 2000):

$$\left(G^T K^{-1} G\right) P = G^T K^{-1} F\ , \tag{2.44}$$

which is used to find the pressure P. This system of equations is solved by using a modified iterative conjugate gradients method (Hestenes and Stiefel, 1952; Ramage and Wathen, 1994) to find the pressure and thus the velocity field via equation (2.42).

A streamline upwind Petrov-Galerkin (SUPG) formulation (Hughes, 2000) is used to solve the energy equation. The approach is similar to the Galerkin formulation described above for Stokes flow, but the finite element implementation of the SUPG formulation also includes an additional

non-physical diffusion term that counteracts the numerical diffusion caused by advection and interpolation of quantities from nodal points to integration points. However, because we have implemented the temperature advection within the tracers (see section below), the SUPG formulation is used to only solve the energy equation (2.21) without the advection term:

$$\frac{\partial T}{\partial t} = \nabla^2 T + \frac{Di}{Ra}\eta\dot{\epsilon}^2 + \rho H \,. \tag{2.45}$$

Also, the terms for adiabatic heating $\gamma \mathbf{u}_z$ and latent heat of melting Φ are left out here because the calculations for these are done at tracer level (see section 2.2.2)

2.2.2 Tracer method

A particle method (e.g. Tackley and King, 2003; Gerya and Yuen, 2003) is used to keep track of compositional quantities within the model domain. The model domain is injected with a high number of so called tracers at the beginning of the model. The initial locations of these tracers are random and they have an homogeneous density distribution. These tracers advect within the velocity field during subsequent time steps, carrying information about things such compositional buoyancy and geochemical information for melting calculations. Tracers are also used for the advection of temperature field.

Each tracer i is associated with the information vector $\mathbf{I}_i$, storing the information it carries, and a location vector $\mathbf{x}_i$. The advection of a tracer is solved by second order Runge-Kutta method, where the new location of a tracer is

$$\mathbf{x}_i^{t+1} = \mathbf{x}_i^t + \mathbf{v}_i^{\text{eff}} \Delta t \,, \tag{2.46}$$

where $\mathbf{v}_i^{\text{eff}}$ is the effective velocity vector for a point $\mathbf{x}_i^{t+\frac{1}{2}}$ halfway along the path of the tracer during the next timestep (Press et al., 2007):

$$\mathbf{v}_i^{\text{eff}} = \mathbf{u}\left(\mathbf{x}_i^{t+\frac{1}{2}}\right) = \mathbf{u}\left(\mathbf{x}_i^t + \mathbf{u}\left(\mathbf{x}_i^t\right)\frac{\Delta t}{2}\right) . \tag{2.47}$$

Some of the information $\mathbf{I}$ carried by the tracers is needed at the finite element mesh to solve the equations of Stoke flow and energy conservation. These quantities are interpolated between tracers and the finite element nodal points.

The interpolation from the tracers to the nodes takes place using

$$\mathbf{I}_n = \frac{\sum_i w_i \mathbf{I}_i}{\sum_i w_i} \,, \tag{2.48}$$

where $\mathbf{I}_n$ is the information vector of the nodal point, i runs over all the tracers within the element where the nodal point is located, and w_i is a weighting factor based on area/volume between the nodal point and the tracer within the element:

$$w_i = \prod_k \left(l_{\text{elem},k} - |x_{i,k} - x_{n,k}| \right) , \tag{2.49}$$

where k runs over spatial dimensions, $\mathbf{l}_{\text{elem}}$ is the size of the element, $\mathbf{x}_i$ is the location of the tracer, and $\mathbf{x}_n$ is the location of the nodal point. Compositional buoyancy (due to lithology changes and depletion), temperature and water content information is interpolated from tracers to the nodal points

Temperature advection in tracers

A tracer method is used to advect the temperature (term $\mathbf{u} \cdot \nabla T$ in equation (2.21)) and to update the temperature according to the amount of adiabatic heating ($\gamma \mathbf{u}_z$) and consumption of latent heat (Φ). The procedure within one time step is the following:

1. Solve the Stokes flow and the simplified energy equation (2.45) to find the velocity and temperature field.
2. Interpolate the change in temperature field, caused by equation (2.45) in step 1, from nodal points to tracers, using bilinear interpolation.
3. Advect tracers according to the velocity field.
4. Update tracer values:
   (a) Add the adiabatic heating $\Delta T_{\text{adiab}} = \gamma u_{i,z}$ to the tracer temperature.
   (b) Calculate the amount of melt produced (see section 2.3) and with it the amount of latent heat consumed. Subtract $\Delta T_{\text{melting}} = L\Delta F / C_p$ from the tracer temperature.
5. Interpolate tracer values (temperature, buoyancy) from the tracers to the nodal points

By interpolating only the change in the temperature (step 2) artificial diffusion due to repeated tracers-to-nodes and nodes-to-tracers interpolations is avoided (Gerya and Yuen, 2003).

2.3 Melting models

Parameterized and thermodynamics based melting models are used to study the extent, volumes and compositions of melts produced in the mantle and in the crust. Material properties (composition, melting history) related to the melting models are carried in tracers (see 2.2) and all melting related calculations are performed at tracer level. Each tracer is assigned a lithology which determines whether a parameterized or thermodynamic melting model is used for that tracer. Tracers representing mantle compositions use parameterized models (section 2.3.1) and tracers representing crustal composition use thermodynamic models (section 2.3.2). Both melting models take into account the latent heat of melting (section 2.3.4).

2.3.1 Parameterized melting models

Parameterized melting models are used for rocks of mantle (peridotite) compositions. These parameterizations (e.g. Katz et al., 2003; Hirschmann et al., 1998; Hirschmann, 2000) relate temperature, pressure and degree of melting, based on thermodynamic calculations and results from melting experiments. These parameterizations may take into account some simple compositional constraints. We have used the parameterization of Katz et al. (2003), which relates $F = f(p, T, X^{\mathrm{melt}}_{\mathrm{H_2O}}, M_{\mathrm{cpx}})$, where F is the degree of melting (also called depletion once melt has been extracted), $X^{\mathrm{melt}}_{\mathrm{H_2O}}$ water concentration in the melt produced (itself a function of F and $X_{\mathrm{H_2O}}$), and M_{cpx} is the modal abundance of clinopyroxene in the rock. The basic principle of the parameterization is to form a parameterization for the solidus and liquidus temperatures as a function of pressure, apply a reduction in these according to the water content, and the assume a function describing the degree of melting between the solidus and liquidus, according to the maximum water saturation level of the melt in given conditions (i.e. so that melts produced close to the solidus are more sensitive to water content than those produced close the liquidus). Parameters for the parameterizations are then adjusted according to experimental and thermodynamic data. In the Katz et al. (2003) parameterization, different sets of parameters are used for values above and below conditions for clinopyroxene exhaustion. This is because melt production rates below clinopyroxene exhaustion are higher than those with clinopyroxene absent. As the clinopyroxene is exhausted from the residue at relatively high values of F (depending on pressure, but generally >20%), a parameterization not considering clinopyroxene abundance is sufficient for mantle melting studies where degrees of melting remain small. Below melting degree of clinopyroxene exhaustion the parameterization can be expressed in an implicit form

$$F(p, T, X^{\mathrm{bulk}}_{\mathrm{H_2O}}) = \left[\frac{T - \left(T_{\mathrm{solidus}}(p) - \Delta T \left(X^{\mathrm{melt}}_{\mathrm{H_2O}} \left(X^{\mathrm{bulk}}_{\mathrm{H_2O}}, p, F \right) \right) \right)}{T_{\mathrm{liquidus}}(p) - T_{\mathrm{solidus}}(p)} \right]^{\beta_1}, \tag{2.50}$$

where, for clarity, $X^{\mathrm{bulk}}_{\mathrm{H_2O}} = X_{\mathrm{H_2O}}$ is the bulk water content used also in viscosity parameterization, T_{solidus} and T_{liquidus} are parameterized dry rock solidus and liquidus, ΔT is the solidus lowering due to water content, and β_1 is a constant. Due to its implicit form, this parameterization requires iterative solver in cases where $X^{\mathrm{bulk}}_{\mathrm{H_2O}} > 0$. We implement the iteration with an adaptive relaxation scheme:

1. Calculate $X^{\mathrm{melt}}_{\mathrm{H_2O},n}$ with given $X^{\mathrm{bulk}}_{\mathrm{H_2O}}$, p and F_{n-1}. During the first iteration (loop counter $n = 1$), $F_0 = F_{\mathrm{tot}}$, the total amount of melt extracted during the history of the tracer (see below).
2. Calculate F_n with given p, T, and $X^{\mathrm{melt}}_{\mathrm{H_2O},n}$ calculated in step 1.
3. If $|F_n - F_{n-1}| < E_w$ exit iteration (E_w is the set precision limit for the iteration). Otherwise,
4. Set $F_n \leftarrow \xi_w F_n + (1 - \xi_w) F_{n-1}$, where ξ_w is the relaxation parameter.
5. If $n > n_{\mathrm{max}}$, adapt relaxation:
   (a) Set $n_{\mathrm{max}} \leftarrow 100/\xi_w$

(b) Set $\xi_w \leftarrow \xi_w/2$

6. Set $n \leftarrow n+1$

7. Go to step 1.

For $n = 1$, maximum number of iterations $n_{\max} = 100$ and $\xi_w = 0.5$. Because all the functions used by the parametrization are continuous and monotonic, the iteration is guaranteed to converge.

We utilize the melting parameterization in two possible ways: In models where melts are not extracted, equation (2.50) is applied every time step to calculate the amount of partial melting existing in equilibrium with the rock (so called instantenous melt amount), and as the bulk composition of the rock does not change, F in the next time step can increase or decrease, depending on whether the amount of partial melt increases or decreases. The total melt depletion parameter F_{tot}, describing the total amount of melt extracted from the rock, and used also in density change parameterization (section 2.1.3), is always zero. In models where melts are extracted, the F from (2.50) is used to calculate the mass of the melt produced and $X^{\text{melt}}_{\text{H}_2\text{O}}$ is used to calculate the mass of water in the melt. The amount of new melt produced (instantenous melt amount) during time step $t+1$ is

$$\mathrm{d}F_{t+1} = \max\left(F_{t+1} - \sum_t \mathrm{d}F_t,\, 0\right), \tag{2.51}$$

where $\sum_t \mathrm{d}F_t = F_{\text{tot}}$ and for initial fertile rock $\mathrm{d}F_0 = 0$. The water content of the residue is then adjusted using mass balance equation

$$\begin{aligned} m^{\text{bulk}}_{\text{H}_2\text{O}} &= X^{\text{melt}}_{\text{H}_2\text{O}} m^{\text{melt}} \qquad + X^{\text{residue}}_{\text{H}_2\text{O}} m^{\text{residue}} \\ &= X^{\text{melt}}_{\text{H}_2\text{O}} m^{\text{bulk}} \mathrm{d}F_{t+1} + X^{\text{residue}}_{\text{H}_2\text{O}} m^{\text{bulk}} \left(1 - \mathrm{d}F_{t+1}\right), \end{aligned} \tag{2.52}$$

where m is the mass of the bulk rock, residue, or melt ($m^{\text{bulk}} = m^{\text{residue}} + m^{\text{melt}}$), and which, when divided by m^{bulk} and re-arranged, gives

$$X^{\text{residue}}_{\text{H}_2\text{O}} = \frac{X^{\text{bulk}}_{\text{H}_2\text{O}} - X^{\text{melt}}_{\text{H}_2\text{O}} \mathrm{d}F_{t+1}}{1 - \mathrm{d}F_{t+1}}. \tag{2.53}$$

This value of the residue water concentration becomes the value of the bulk water concentration ($X_{\text{H}_2\text{O}}$) in the next time step. Unlike in cases where melts are not extracted, in this case the amount of total depletion cannot decrease, as is seen from eq. (2.51).

2.3.2 Principles of thermodynamic models of phase equilibria

Gibbs energy minimization is used to find the thermodynamically stable phases of a closed system, and the concentrations of chemical species (components) in them, *in equilibrium state*, in given temperature, pressure and system bulk composition. By *phase* one means "a substance that is spatially uniform at the macroscopic scale and is physically distinct from its surroundings in a

system" (Ganguly, 2008). Thus, in rocks, minerals and melt phases commonly constitute the phases of the system. These phases can also be solid solutions of two ore more end members (e.g. Ca-Na feldspar). *Components* are those chemical species that are needed to build up all the phases of the system. The number of components in a system is uniquely defined, but there are usually multiple different choices for the components of the system. In geological applications, components are usually chosen as major oxides, such as SiO_2, MgO, Al_2O_3, etc.

The concept of phase equilibrium has its roots in the second law of thermodynamics, which states that for any isolated system, the condition for spontaneous process to occur, is

$$\mathrm{d}S \geq 0, \tag{2.54}$$

where S is the entropy of the system. From this, a criteria for equilibrium can be stated in respect to the Gibbs free energy of the system, G (Liu and Bassett, 1986):

$$(\mathrm{d}G)_{T,P} \geq 0\,. \tag{2.55}$$

Gibbs free energy is defined in constant temperature and pressure, so it is usually the most useful measure in geological applications. Gibbs energy is defined as

$$G = \sum_{i=1}^{p}\sum_{j=1}^{c} n_{ij}\mu_{ij}\,, \tag{2.56}$$

where p and c are the numbers of phases and components, n_{ij} is the number of moles and μ_{ij} is the chemical potential of component j in phase i (Connolly and Kerrick, 1987). The chemical potential of a component, μ_j, is a measure of internal energy change when an infinitesimal change in n_j is introduced, i.e. $\mu_j \equiv (\partial U/\partial n_k)_{P,T,(n_k,k\neq j)} = (\partial G/\partial n_k)_{P,T,(n_k,k\neq j)}$. In equilibrium the chemical potentials of the same components in all phases must be equal to each other, $\mu_{1j} = \mu_{2j} = \ldots = \mu_{pj}$, and (2.56) can be rewritten as

$$G = \sum_{j=1}^{c} n_j\mu_j\,. \tag{2.57}$$

where n_j and μ_j are the molar amount and chemical potential of the component j in the whole system.

Finding the stable phases is a matter of minimizing G of the whole system, that is, minimizing

$$G = \sum_{i=1}^{p} \alpha_i G_i, \tag{2.58}$$

where α_i and G_i are the stoichiometric abundance and Gibbs energy of the phase i. In addition, following constraints need to be met:

$$\alpha_i \geq 0 \tag{2.59}$$

for each i (phases cannot have negative abundances), and

$$n_j = \sum_{i=1}^{p} \alpha_i n_{ij},\ j = 1 \dots c \tag{2.60}$$

which states that the total amount of a component is the sum of its abundances in the phases. In a geological application, this corresponds to finding the combination and amounts of phases (minerals, melts, and fluids) and their compositions that has the lowest possible Gibbs free energy. The distribution of components between phases is varied but temperature, pressure, and bulk composition is held constant. In the following, basic principles for calculating the system's Gibbs free energy are given.

The change in the Gibbs free energy of one phase is (the Gibbs fundamental equation)

$$\mathrm{d}G = V\mathrm{d}P - S\mathrm{d}T + \sum_{j=1}^{c} \mu_j \mathrm{d}n_j \,. \tag{2.61}$$

In constant T and P the change in Gibbs energy is due only to transfer of some components between phases (the last term), e.g. reactions between minerals in a rock. Differentiating equation (2.56) gives

$$\mathrm{d}G = \sum_{j=1}^{c} n_j \mathrm{d}\mu_j + \sum_{j=1}^{c} \mu_j \mathrm{d}n_j \ . \tag{2.62}$$

Combining equations (2.61) and (2.62), and assuming $dP = 0$ and $dT = 0$, gives the Gibbs-Duhem relation,

$$\sum_{j=1}^{c} n_j \mathrm{d}\mu_j = 0 \ , \tag{2.63}$$

which is a base for evaluation of changes among the chemical potentials of a phase in constant P and T (Ganguly, 2001). The chemical potential of a component j in a phase α is

$$\mu_j^{\alpha}(P,T,X) = \mu_j^{\alpha,\star}(T) + RT \ln a_j^{\alpha}(P,T,X) \ , \tag{2.64}$$

where

$$a_j^{\alpha}(P,T,X) = \frac{f_j^{\alpha}(P,T,X)}{f_j^{\star}(T)} \ . \tag{2.65}$$

Here, P, T and X are the pressure, temperature and composition (mole fraction $X = n_j / \sum n_j$) of interest, R is the gas constant, a_j^{α} is the *activity*, or "effective concentration", of the component in given conditions, $\mu_j^{\alpha,\star}$ is the chemical potential ($\mu_j = \frac{\partial G_j}{\partial n_j}$) of the pure component j in its *standard state,* f_j^{α} is the fugacity of the component in given conditions, and $f_j^{\star}$ is the fugacity of the component in its standard state. Standard state refers to any chosen state that is at the temperature of interest and at a fixed composition. In equilibrium, the chemical potential of each component j has to be equal in each phase, i.e. $\mu_j^{\alpha} = \mu_j^{\beta} = \mu_j^{\gamma} = \dots$ etc. for each phase α, β, γ, ….

For example, the chemical potentials of component O_2 in water vapour residing above liquid water are equal $\mu_{O_2}^{\text{liquid}} = \mu_{O_2}^{\text{vapour}}$. Similarly, one can write $\mu_{Al_2O_3}^{\text{sillimanite}} = \mu_{Al_2O_3}^{\text{cordierite}}$ for a metamorphic pelitic hornfels where sillimanite and cordierite exist in equilibrium with each other.

The standard state chemical potential of the pure component j, needed to evaluate eq. (2.64), is

$$\mu_j^\star(P,T) = G^\circ_{f,298,j} - \int_{298}^{T} S^\circ_{f,j}(T)\mathrm{d}T + \int_{P^\circ}^{P} V_{T,j}(P)\mathrm{d}P = G^\circ_{f,T,j} + \int_{P^\circ}^{P} V_{T,j}(P)\mathrm{d}P \ , \tag{2.66}$$

where $G^\circ_{f,298|T,j}$ $S^\circ_{f,j}$ are the Gibbs energies and entropy of formation of the component in temperatures 298 K and T, V_j is the molar volume, and P° is the pressure of formation in G° and S°. Because measurements for the Gibbs energy of formation are rarely available and instead the enthalpy and entropy of formation and the isobaric heat capacity are usually measured by calorimetric studies, equation (2.66) is transformed using relation

$$G = H - TS \tag{2.67}$$

and relation between isobaric heat capacity and entropy ($C_p(T) = T\left(\frac{\partial S}{\partial T}\right)_P$) to give

$$G_j^\star(P,T) = H^\circ_{f,298,j} + \int_{298}^{T} C^\circ_{P,f,j}(T)\mathrm{d}T - T\left[S^\circ_{f,298,j} + \int_{298}^{T}\left(\frac{C^\circ_{P,f,j}}{T}\right)\mathrm{d}T\right] + \int_{P^\circ}^{P} V_{T,j}(P)\mathrm{d}P\,. \tag{2.68}$$

Here the standard state chemical potential μ_j^* is replaced by partial molar Gibbs energy G_j^*, which are equivalent in constant P and T, $\mu_j^* = \left(\frac{\partial G_j^*}{\partial n_j}\right)_{P,T}$. Values of enthalpy and entropy of formation of different components of interest in geological sciences are usually tabulated in thermodynamic databases (e.g. Stixrude and Lithgow-Bertelloni, 2011; Holland and Powell, 1998; Berman, 1988; Robie et al., 1979), together with information about equations of state (for pressure-volume relationships) and tabulated data of heat capacity C_P (see below).

Fugacity, used in equation (2.65) to define activity, and needed to evaluate the partial molar Gibbs energies (chemical potentials) of mixtures of components, is a measure of equilibrium vapor pressure, i.e. the vapor pressure exerted by a solid substance introduced into an evacuated container when they are in equilibrium. This equilibrium vapor pressure could be used as a measure of the relative stabilities of the gas and condensed phase, as long as the gas phase behaves as an ideal gas. When not, corrections need to be used and one comes up with fugacity, the corrected vapor pressure. By analogy to the relation between the Gibbs energy and the vapor pressure of an ideal gas,

$$\mathrm{d}G = V\mathrm{d}P = RT\mathrm{d}\ln P \ , \tag{2.69}$$

the fugacity f is defined as

$$\mathrm{d}G = RT\mathrm{d}\ln f = RT\mathrm{d}\ln(P\phi) \ , \tag{2.70}$$

where ϕ is the fugacity coefficient. Additionally, the perfect gas behaviour should be reached at

sufficiently low pressures:

$$\lim_{P\to 0} f = P \ . \tag{2.71}$$

Thus, the discrepancy between ideal gas and real gas behaviour can be measured to find out the fugacity coefficient of a real gas and the fugacity itself. If the condensed phase is a solution of multiple components, the partial pressures of these components should ideally follow their concentrations in the condensed phase with linear proportionality. However, real gas behaviour is different, and thus the fugacities are proportional to the concentrations:

$$f_j = f_j^\circ X_j \gamma_j \ , \tag{2.72}$$

where f_j° is the fugacity of the pure component, and γ_j is an *activity coefficient* to account for different energetic properties of the components in solution. Now, the activity of component j in phase α can be redefined as

$$a_j^\alpha = (X_j^\bullet \gamma_j^\bullet)^\alpha \ , \tag{2.73}$$

where $X_j^\bullet$ is a some chosen measure of the content of j in the phase (simplest choice is $X_j^\bullet = X_j$), and $\gamma_j^\bullet$ is the corresponding activity coefficient.

Using equation (2.73) , the chemical potential (eq. (2.64)), can be expressed as

$$\mu_j^\alpha(P,T,X) = \mu_j^{\star,\alpha}(T) + RT\ln X_j^{\bullet,\alpha} + RT\ln \gamma_j^{\bullet,\alpha} \ . \tag{2.74}$$

Consequently, the molar Gibbs energy of a phase is

$$G^\alpha = \sum_{j=1}^{c} X_j \mu_j^\star + RT\sum_{j=1}^{c} X_j \ln X_j^\bullet + RT\sum_{j=1}^{c} X_j \ln \gamma_j^\bullet \ . \tag{2.75}$$

The first term is total Gibbs energy of the phase due to mechanical mixing of components, and the sum of the second and third terms is the Gibbs energy of chemical mixing, ΔG^{mix}, accounting for changes in the Gibbs energy due to chemical interaction between components within the phase. (Ganguly, 2001)

The parameterizations used to determine the values of activity coefficients and ways to measure $X_j^\bullet$ in equation (2.73) are called activity models for solid solutions (and activity models for the melt). Activity models may also use more complex forms of eq. (2.73) to determine the activity of a component in a phase (Holland and Powell, 1998).

In order to use equations (2.61) and (2.68) one needs to find the integral of the $V_{T,j}$ over a pressure range from the reference state to the pressure of interest. For this the volume must be known as a function of pressure. Such a relation is known as *equation of state* (EoS). A simple example is the ideal gas EoS, $pV = nRT$. For solids and fluids more advanced equations of state are used, such as the Birch-Murnaghan equation of state and equation of state for silicate liquids (Ghiorso et al., 2002). The integral of heat capacity $C_{P,f,j}^\circ$ over the temperature range from the reference

temperature to the temperature of interest requires knowledge of the heat capacity as a function of temperature. For this purpose, measurements of heat capacity at different temperatures for materials of interest are performed and the data parameterized.

The standard state Gibbs free energies and entropies for different components, the activity model parameters for different solid solutions and melt phases, and the heat capacity and equations of state are tabulated in collected into so called thermodynamic databases. These thermodynamic databases (e.g. Holland and Powell, 1998; Stixrude and Lithgow-Bertelloni, 2011; Ghiorso et al., 2002; Berman, 1988) are used as input data for calculations of thermodynamic geochemical models.

2.3.3 Integration of thermodynamic models with mantle convection code

The thermodynamic Gibbs energy minimization code PerpleX (Connolly, 2005) is used. The choice of PerpleX over more widely used software for mantle melting models (e.g. MELTS/pMELTS, Ghiorso et al., 2002) was dictated by the free availability of its source code and, thus, easier integration with the mantle convection code Citcom. In order to do the Gibbs energy minimization, equation (2.75) needs to be solved for multiple possible compositions of phases in course of minimization. The non-linearity of these functions causes technical problems with performance, stability and convergence, especially when the number of phases and components increases. In addition, the mixing properties of components may cause local minima of G outside the global minima to exist, and a method to find the global minimum is needed. One solution is to use so called "pseudocompounds", originally developed by White et al. (1958). In the pseudocompound method, the Gibbs free energy of the solution is calculated in a finite number of pre-determined phase compositions (linear combinations of components), called pseudocompounds, thus effectively discretizing the composition space and approximating the Gibbs energy function by linear approximations between the discretized points. This removal of compositional degrees of freedom reduces the problem of Gibbs energy minimization into group of linear equations that can be solved by effective direct solvers of linear equation groups (White et al., 1958).

The source code of PerpleX is available upon request from the author. The subroutines of the provided source code have been called from within the mantle convection code to use the required functionality of PerpleX. PerpleX subroutines are written in programming language *Fortran*, whereas the mantle convection code has been written in *C*. A set of interface routines, callable from C, have been written, and provide a simple interface to the Gibbs free energy minimization procedure. These interface routines are

1. An initialization routine, `ini_phaseq(datafile)`, that reads and initializes the thermodynamic databases from the given file, and
2. `[name_phases, wt_phases, composition_phases] = phaseq(P, T, bulk_composition)`, that, based on input data of pressure, temperature and rock bulk composition, calls the PerpleX routines that calculate the equilibrium phase composition, reads the results from the PerpleX memory space and returns the reformatted results: the names of the stable phases (minerals, possible melt), their weight percentage, and the composition of these phases (in terms of major oxide components used).

From the output data of routine `phaseq()`, the amount of melt phase is checked, and, if existing, the composition of the melt phase is recorded and stored in the tracers of the mantle convection code. The information given by the thermodynamic melting model is handled similarly to the parameterized melting models, as described in section 2.3.1. The melt amount returned by `phaseq()` is directly recorded as dF_t and F (cf. Equation (2.51) of parameterized models where the value of dF_t depends on the history of the previous values of dF). Again, the melt can be either extracted or left in place. If the melt is left in place, the dF_{t+1} will get a new value directly from `phaseq()` during the next time step $t+1$. If melts are extracted, the F_{tot} is increased by dF_t, i.e. $F_{tot} = \sum_t dF_t$ as in parameterized models.

Because `phaseq()` returns the full melt composition (all major oxides used in the modelling), the residue composition in case of melt extraction can be easily calculated on basis of mass balance (similarly to the case of water in parameterized melting models, Eq. (2.52)).

2.3.4 Latent heat of melting

Melting a rock consumes latent heat. This is taken into account when calculating the amounts of melts produced by the melting models. The amount of rock melted during one time step, $\mathrm{d}F_t$, consumes latent heat of amount $E_{\text{latent}} = \mathrm{d}F_t m L$, where m is the mass of the rock and L is the specific latent heat of melting (J/kgK). The total heat content of the rock is not allowed to change during the melting, so the consumption of latent heat decreases the temperature of the rock. This, on the other hand, decreases the amount of partial melt. The consumed latent heat corresponds to a temperature decrease of $\Delta T_{\text{melting}} = E_{\text{latent}}/(mC_p) = \mathrm{d}F_t L/C_p$. This reduction in T may affect the amount of melting, so to find the correct amount of melt produced, an iterative solver needs to be implemented. The iteration uses an adaptive relaxation scheme and has the following steps ($n = 1 \ldots n_{\max}$), performed each time step for each tracer:

1. Calculate the amount of melt produced during this time step, $\mathrm{d}F_{t,n}(T - \Delta T_{\text{melting},n-1})$, as described in sections above. For $n = 1$, $\Delta T_{\text{melting},n=0} = 0$.
2. If $|\mathrm{d}F_{t,n} - \mathrm{d}F_{t,n-1}| < \epsilon_L$ the iteration has converged, exit iteration (ϵ_L is the set precision limit for the iteration; $\mathrm{d}F_{t,0} = 0$). Otherwise,
3. Set $\mathrm{d}F_{t,n} \leftarrow \xi_L \mathrm{d}F_{t,n} + (1 - \xi_L)\mathrm{d}F_{t,n-1}$, where $0 < \xi_L \leq 1$ is a relaxation parameter.
4. Calculate $\Delta T_{\text{melting},n} = \mathrm{d}F_{t,n} L/C_p$.
5. If $n > n_{\max}$, adapt relaxation:
   (a) Set $n_{\max} \leftarrow 100/\xi_L$
   (b) Set $\xi_L \leftarrow \xi_L/2$
6. Set $n \leftarrow n + 1$
7. Go to step 1.

Initially, for $n = 1$, maximum number of iterations $n_{\max} = 100$ and $\xi_L = 0.5$. For the parameterized melting model, $\mathrm{d}F_t(T)$ is a monotonic continuous function and the iteration converges usually quickly. For the thermodynamic melting model, phase changes can be discontinuous and the amount of melting as a function of temperature might have abrupt jumps, especially from $\mathrm{d}F_t = 0$ to $\mathrm{d}F_t = \epsilon_L$ where ϵ_L is some small number >0. In this case the iteration does not easily converge or, indeed, there might be no solution at all for the iteration. If no convergence takes place after maximum number of relaxation adaptations (step 5), it is assumed that no melt is formed and no latent heat is thus consumed. Usually this leads to a scenario where the "unused" latent heat remains available for melting during the consequent time step(s) and thus, melting more easily commences (the degree of first melts is higher) and convergence of the latent heat loop happens more quickly.

2.4 Benchmarking

The finite element code Citcom has been widely used in mantle convection models (e.g. van Wijk et al., 2010; van Hunen et al., 2003; Bianco et al., 2011; Ballmer et al., 2009; Huang et al., 2003), and has been previously also benchmarked for its ability to solve the set of equations for the extended Boussinesq approximation (King et al., 2009). We have further benchmarked and analyzed features that are of special interest in models we have build.

2.4.1 Viscosity contrasts

Our models with feedback between melting and depletion stiffening via dewatering, and, on the other hand, between melting and melt weakening, could cause strong viscosity variations within the model (up to about two orders of magnitude at a length scale of one element).

The ability of the code to handle strong viscosity contrasts has been tested with the so called falling block benchmark (Gerya and Yuen, 2003; Gerya, 2010) and with a Rayleigh-Taylor instability benchmark with high viscosity contrast from van Keken et al. (1997).

Falling block benchmark

The falling block benchmark model setup consists of a 500 km x 500 km model domain with a negatively buoyant block of size 100 km x 100 km in the middle of the box. The block and the medium surrounding it have constant viscosities η_{block} and η_{medium}, respectively. The viscosity ratio between the block and the medium is varied and the maximum velocity of the block falling downwards is measured. It is expected that as the ratio increases, the deformation of the block during the fall tends to zero (i.e. the block keeps its original form), and so the velocity should approach a constant. Results of the benchmark (Fig 2.3) show that this kind of behaviour is indeed reached. Our code with a higher resolution shows a similar behaviour when the ratio decreases. Results shown by Gerya (2010) behave similarly, although the results from the program code provided by the author shows deviating behaviour (velocity continues to increase) when re-run. Our code with lower resolution shows similar behaviour to the results from the program

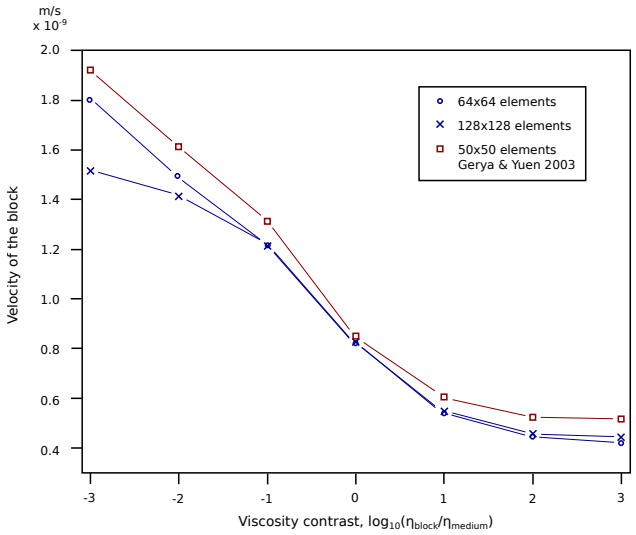

Figure 2.3: Results of the falling block benchmark. Boxes mark results from the finite difference code provided by Gerya (2010), circles and crosses show results from our code, with two different mesh resolutions.

code provided by Gerya (2010). For viscosity contrasts $\geq 10^{-1}$ the results from our code have consistently lower velocities with relatively consistent absolute error. The velocities from our two models with different resolutions show very good agreement with each other, except for viscosity contrasts $\leq 10^{-2}$.

Although a good measure for the capability of a mantle convection code to handle high viscosity contrasts, the falling block benchmark has not been yet widely used to benchmark mantle convection codes. Because of this lack of benchmark results from other codes and because of the discrepancies between the results from the MATLAB code provided by Gerya (2010) and the results shown by Gerya (2010) but based on a code implementation presented in Gerya and Yuen (2003), we think it is still unclear what should be taken as the correct result for the benchmark. However, we note that all the results, including both from our Citcom code, approach a constant value when $\eta_{\text{block}}/\eta_{\text{medium}}$ increases, as is intuitively expected.

Rayleigh-Taylor instability with high viscosity contrast

The benchmark from van Keken et al. (1997) consists of closed two-dimensional box with an aspect ratio of 1:0.9142 and free-slip boundary conditions. The bottom part ($y < 0.2$) of the isothermal model domain is a buoyant layer of material with a viscosity of η_0. The top part of the model domain ($0.2 < y < 1$) has a viscosity of η_r. The viscosity contrast between these layers is $\eta_0/\eta_r = 0.01$. The interface between the layers is initially disturbed to initialize the Rayleigh-Taylor instability. We run the benchmark with resolution 64x64 elements. The root mean square velocity of the model is recorded as a function of model time and compared to results reported in van Keken et al. (1997).

The results (Fig 2.4) show some variation depending on the resolution used. Our models record a maximum non-dimensional root mean square velocity of 0.01478 for the 64x64 elements model. This is slightly but not much higher than the average (0.01430) of the results from similar resolution (80x80) finite element models reported by van Keken et al. (1997). The time when the maximum

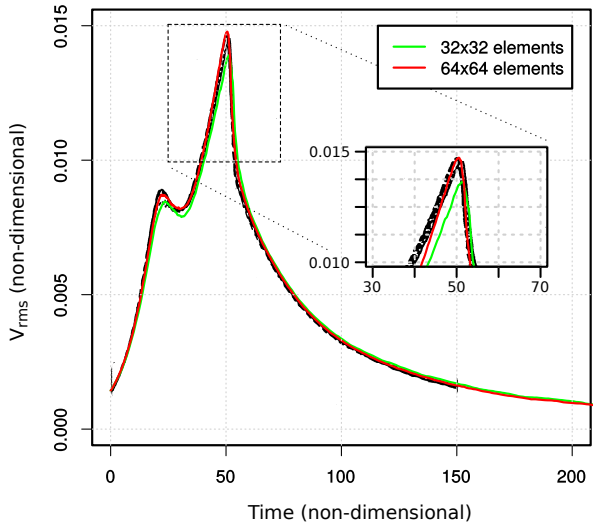

Figure 2.4: The root mean square velocities from the van Keken et al. (1997) benchmark. Red and green lines are results from our code, the black line shows results from selected mid- to high-resolution models presented by van Keken et al. (1997).

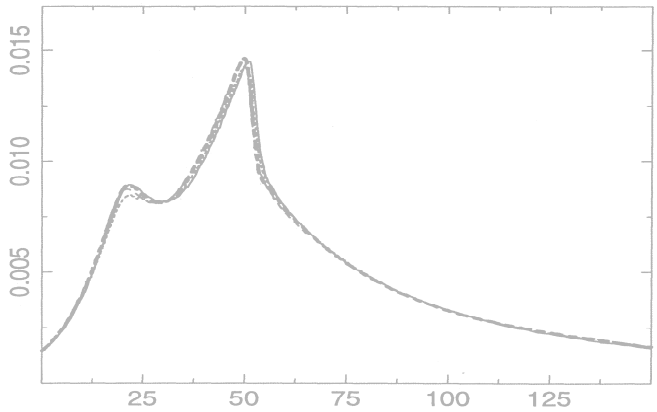

velocity occurs is 50.49 in our model, whereas the average from the same models reported by van Keken et al. is 51.26, i.e. slightly later than in our models. Same comparison for the 32x32 model (ours) and the average from those reported by van Keken et al. (resolutions 30x30 to 41x41) gives $V_{\mathrm{rms}} = 0.01391$ / $t = 51.33$ (ours) versus $V_{\mathrm{rms}} = 0.01474$ / $t = 49.60$ (van Keken et al., 1997). The resolution dependency of the results is comparable in both our models and results reported by van Keken et al.

2.4.2 Temperature in tracers

Temperature advection with the help of tracers is not regularly done in studies using Citcom. However, implementation of temperature advection in tracers greatly helps reducing problems related to the instability, or "overshooting", that appear in the streamline upwind Petrov-Galerkin scheme near strong contrasts in the temperature field (Bochev et al., 2004). Because of this, and because our code implementation heavily relies on having the temperature information available at tracers (as needed by the melting models) we use the implementation for temperature advection in tracers. Thus, we have made sure that the temperature advection in tracers does not affect the solution of the Stokes flow. For this purpose, we have run one of the benchmarks provided by Blankenbach et al. (1989), using both traditional advection scheme within the finite element formulation and advection scheme implemented with tracers.

The model setup consists of 2D unit box that is bottom heated with a constant bottom and surface temperatures, has closed free-slip boundaries and zero heat flow at the sides. Rayleigh number for the convection is 10^5 and the resolution used is 32x32 elements. A steady state convection cell is formed within the model domain, for which the root mean square velocity is measured as a function of time (Fig 2.5). Apart from slight offset in time at $t = 0.02 \ldots 0.04$, the root mean square velocities in the models with tracer advection scheme follow those produced by the finite element advection scheme. The two tracer advection schemes with different tracer densities are virtually indistinguishable. The tracer density 40 tracers per element has been used throughout the studies. The steady-state values of the root mean square velocities are: FE advection scheme, 194.2049; high density tracer advection scheme, 191.5011; low density tracer advection scheme, 191.5044; and the estimate for best value by Blankenbach et al. (1989), 193.2145. All the values from our code differ by less than 1 % from the given estimate for best value.

2.4.3 Melting models

To assert the correctness of the implementation of the parameterized melting model within the Citcom code, we have compared results from a simple 1D melting model run in Citcom and the solution of equation (2.50) solved independently in the computer software MATLAB. As the analytical equation (2.50) limits itself to only the melting degrees below clinopyroxene exhaustion and because our models do reach very high melting degrees (>25%), we only compare melting below the clinopyroxene exhaustion level. Our model in Citcom consists of a one-dimensional domain where the flow is prescribed and upwards with a constant velocity. Temperature for the material flowing in from the bottom is 1350°C. Thus, this setup resembles a very simple mid-ocean

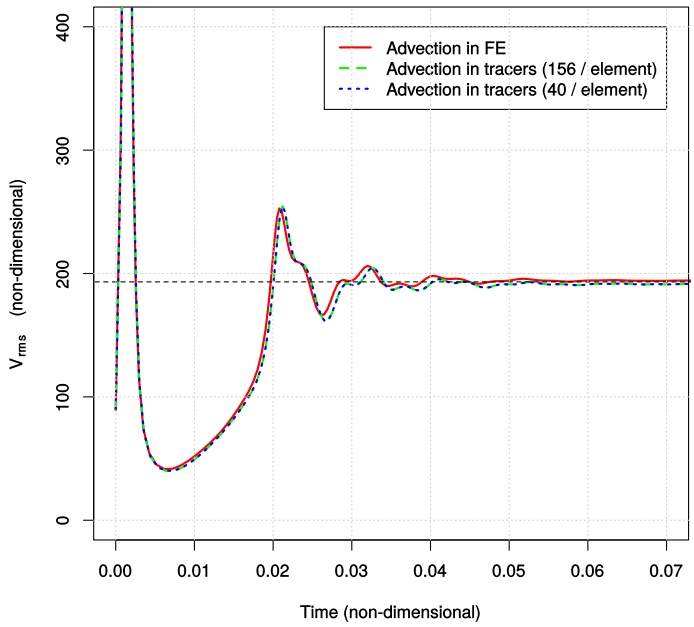

Figure 2.5: Time versus root mean square velocity in a Blankenbach et al. (1989) benchmark. Temperature advection by tracers (dashed lines) produces almost identical results with temperature advection in the finite element formulation (solid line). The dashed black line shows the estimate for the best steady-state V_{rms} value given by Blankenbach et al. (1989).

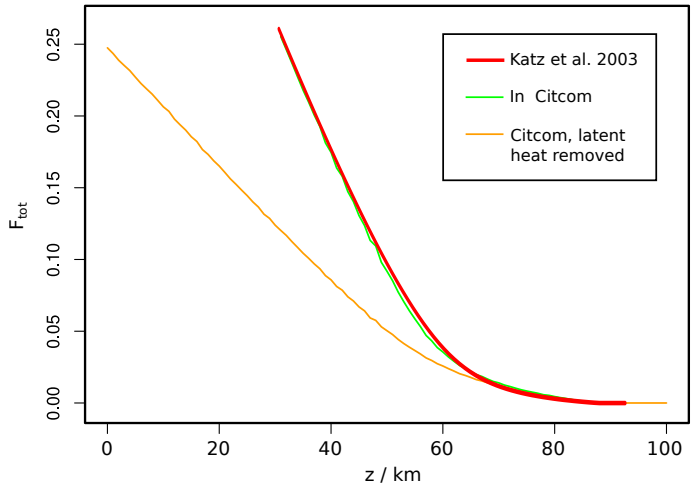

Figure 2.6: Amount of depletion (vertical axis) in the 1D column (horizontal axis), produced by solving equation (2.50) from Katz et al. (2003) independently in MATLAB (red line) and by using kinematic convection model in Citcom (green line). The orange line shows amount of depletion produced when latent heat of melting is removed in accordance with the amount of depletion (calculated in Citcom, no analytical solution available).

ridge model where the mantle is upwelling. Figure 2.6 shows that the total amount of depletion produced in the Citcom implementation of the melting model follows closely that produced by solving (2.50) independently in MATLAB.

References

Ballmer, M. D., J. van Hunen, G. Ito, T. A. Bianco, and P. J. Tackley (2009). "Intraplate volcanism with complex age-distance patterns: A case for small-scale sublithospheric convection". In: *Geochemistry, Geophysics, Geosystems* 10.Q06015.

Berman, R. G. (1988). "Internally consistent thermodynamic data for rock-forming minerals in the system SiO2-TiO2-Al2O3-Fe2O3-CaO-MgO-FeO-K2O-Na2O-H2O-CO2". In: *Journal of Petrology* 29.2, pp. 445–522.

Bianco, T. A., C. P. Conrad, and E. I. Smith (2011). "Time dependence of intraplate volcanism caused by shear-driven upwelling of low-viscosity regions within the asthenosphere". In: *Journal of Geophysical Research* 116.B11, B11103.

Blankenbach, B, F Busse, U Christensen, L Cserepes, D Gunkel, U Hansen, H Harder, G Jarvis, M Koch, G Marquart, et al. (1989). "A benchmark comparison for mantle convection codes". In: *Geophysical Journal International* 98.1989, pp. 23–38.

Bochev, P. B., M. D. Gunzburger, and J. N. Shadid (2004). "Stability of the SUPG finite element method for transient advection-diffusion problems". In: *Computer Methods in Applied Mechanics and Engineering* 193.23-26, pp. 2301–2323.

Brooks, A. N. (1981). "A Petrov-Galerkin Finite Element Formulation". PhD thesis. California Institute of Techonoly, Pasadena, California, p. 120.

Bunge, H.-P., M. A. Richards, and J. R. Baumgardner (1997). "A sensitivity study of three-dimensional spherical mantle convection at 10^8 Rayleigh number: Effects of depth-dependent viscosity, heating mode, and endothermic phase change". In: *Journal of Geophysical Research* 102.B6, pp. 11991–12007.

Christensen, U. (1984). "Convection with pressure- and temperature-dependent non-Newtonian rheology". In: *Geophysical Journal of the Royal Astronomical Society* 77, pp. 343–384.

Christensen, U. R. and D. A. Yuen (1985). "Layered Convection Induced by Phase Transitions". In: *Journal of Geophysical Research* 90.B12, pp. 10291–10300.

Connolly, J. A. D. (2005). "Computation of phase equilibria by linear programming: A tool for geodynamic modeling and its application to subduction zone decarbonation". In: *Earth and Planetary Science Letters* 236.1-2, pp. 524–541.

Connolly, J. A. D. and D. M. Kerrick (1987). "An algorithm and computer program for calculating composition phase diagrams". In: *CALPHAD* 11, pp. 1–55.

Dixon, J. E., T. H. Dixon, D. R. Bell, and R Malservisi (2004). "Lateral variation in upper mantle viscosity: role of water". In: *Earth and Planetary Science Letters* 222.2, pp. 451–467.

Ganguly, J. (2001). "Thermodynamic modelling of solid solutions". In: *EMU Notes in Mineralogy* 3.3, pp. 37–69.

– (2008). *Thermodynamics in Earth and Planetary Sciences*. Berlin: Springer-Verlag, p. 501.

Gerya, T. V. (2010). *Introduction to numerical geodynamic modelling*. Cambridge University Press, 345 pp.

Gerya, T. V. and D. A. Yuen (2003). "Characteristics-based marker-in-cell method with conservative finite-differences schemes for modeling geological flows with strongly variable transport properties". In: *Physics of the Earth and Planetary Interiors* 140.4, pp. 293–318.

Ghiorso, M. S., M. M. Hirschmann, P. W. Reiners, and V. C. Kress (2002). "The pMELTS: A revision of MELTS for improved calculation of phase relations and major element partitioning related to partial melting of the mantle to 3 GPa". In: *Geochemistry Geophysics Geosystems* 3.5.

Hestenes, M. R. and E. Stiefel (1952). "Methods of Conjugate Gradients for Solving Linear Systems". In: *Journal of Research of the National Bureau of Standards* 49.6, pp. 409–436.

Hirschmann, M. M., M. S. Ghiorso, L. E. Wasylenki, P. D. Asimow, and E. M. Stolper (1998). "Calculation of Peridotite Partial Melting from Thermodynamic Models of Minerals and Melts. I. Review of Methods and Comparison with Experiments". In: *Journal of Petrology* 39.6, pp. 1091–1115.

Hirschmann, M. M. (2000). "Mantle solidus: Experimental constraints and the effects of peridotite composition". In: *Geochemistry Geophysics Geosystems* 1.2000GC000070.

Hirschmann, M. M., C. Aubaud, and A. C. Withers (2005). "Storage capacity of H2O in nominally anhydrous minerals in the upper mantle". In: *Earth and Planetary Science Letters* 236.1-2, pp. 167–181.

Hirth, G. and D. Kohlstedt (2003). "Rheology of the Upper Mantle and the Mantle Wedge: A view from the Experimentalists". In: *Geophysical Monograph* 183, pp. 83–105.

Holland, T. J. B. and R. Powell (1998). "An internally consistent thermodynamic data set for phases of petrological interest". In: *Journal of Metamorphic Geology* 16.3, pp. 309–343.

Huang, J., S. Zhong, and J. van Hunen (2003). "Controls on sublithospheric small-scale convection". In: *Journal of Geophysical Research* 108.B8, p. 2405.

Hughes, T. J. R. (2000). *The Finite Element Method : linear static and dynamic finite element analysis*. New York: Dover Publications, 682 pp.

Karato, S.-i. (2010). "Rheology of the deep upper mantle and its implications for the preservation of the continental roots: A review". In: *Tectonophysics* 481.1-4, pp. 82–98.

Katz, R. F., M. Spiegelman, and C. H. Langmuir (2003). "A new parameterization of hydrous mantle melting". In: *Geochemistry Geophysics Geosystems* 4.9, p. 1073.

King, S. D., C. Lee, P. E. van Keken, W. Leng, S. Zhong, E. Tan, N. Tosi, and M. C. Kameyama (2009). "A Community Benchmark for 2D Cartesian Compressible Convection in the Earth's Mantle". In: *Geophy* 179, pp. 1–11.

Kohlstedt, D. L., H. Keppler, and D. C. Rubie (1996). "Solubility of water in the α, β and γ phases of $(\mathrm{Mg,Fe})_2\mathrm{SiO}_4$". In: *Contrib Mineral Petrol* 123, pp. 345–357.

Liu, L.-G. and W. A. Bassett (1986). *Elements, oxides, silicates. High-pressure phases with implications for the Earth interior*. New York, London: Oxford University Press.

Mei, S. and D. Kohlstedt (2000). "Influence of water on plastic deformation of olivine aggregates 1 . Diffusion creep regime". In: *Journal of Geophysical Research* 105, pp. 21457–21469.

Mei, S., W. Bai, T. Hiraga, and D. Kohlstedt (2002). "Influence of melt on the creep behavior of olivine-basalt aggregates under hydrous conditions". In: *Earth and Planetary Science Letters* 201.3-4, pp. 491–507.

Moresi, L.-N. and V. S. Solomatov (1995). "Numerical investigation of 2D convection with extremely large viscosity variations". In: *Physics of Fluids* 7.9, p. 2154.

Moresi, L. and M. Gurnis (1996). "Constraints on the lateral strength of slabs from three-dimensional dynamic flow models". In: *Earth and Planetary Science Letters* 138, pp. 15–28.

Niu, Y., M. J. O'Hara, and J. A. Pearce (2003). "Initiation of Subduction Zones as a Consequence of Lateral Compositional Buoyancy Contrast within the Lithosphere: a Petrological Perspective". In: *Journal of Petrology* 44.5, pp. 851–866.

Press, W. H., S. A. Teukolsky, W. T. Vetterling, and B. P. Flannery (2007). *Numerical recipes : the art of scientific computing*. Ed. by r. Edition. New York: Cambridge University Press.

Ramage, A. and A. J. Wathen (1994). "Iterative solution techniques for the Stokes and Navier-Stokes equations". In: *International Journal of Numerical Methods in Fluids* 19, pp. 67–83.

Robie, R. A., B. S. Hemingway, and J. R. Fisher (1979). "Thermodynamic properties of Minerals and Related Substances at 298.15 K and 1 Bar (10^5 Pascals) Pressure at Higher Temperatures". In: *U.S. Geological Survey Bulletin* 1452.

Schubert, G., D. L. Turcotte, and P. Olson (2001). *Mantle Convection in the Earth and Planets*. Cambridge: Cambridge University Press, p. 940.

Schutt, D. L. and C. E. Lesher (2006). "Effects of melt depletion on the density and seismic velocity of garnet and spinel lherzolite". In: *Journal of Geophysical Research* 111.B5, pp. 1–24.

Stixrude, L and C Lithgow-Bertelloni (2011). "Thermodynamics of mantle minerals - II. Phase equilibria". In: *Geophysical Journal International* 184.3, pp. 1180–1213.

Tackley, P. J. and S. D. King (2003). "Testing the tracer ratio method for modeling active compositional fields in mantle convection simulations". In: *Geochemistry, Geophysics, Geosystems* 4.4.

White, W. B., S. M. Johnson, and G. B. Dantzig (1958). "Chemical Equilibrium in Complex Mixtures". In: *The Journal of Chemical Physics* 28.5, p. 751.

Zhong, S. J., D. A. Yuen, and L. N. Moresi (2009). "Numerical methods for mantle convection". In: *Treatise on Geophysics, vol. 7, Mantle Dynamics*. Ed. by D. Bercovici and G. Schubert. Amsterdam: Elsevier B.V., pp. 227–252.

Zhong, S., M. T. Zuber, L. Moresi, and M. Gurnis (2000). "Role of temperature-dependent viscosity and surface plates in spherical shell models of mantle convection". In: *Journal of Geophysical Research* 105.B5, pp. 11063–11082.

van Hunen, J., S. Zhong, N. Shapiro, and M. Ritzwoller (2005). "New evidence for dislocation creep from 3-D geodynamic modeling of the Pacific upper mantle structure". In: *Earth and Planetary Science Letters* 238.1-2, pp. 146–155.

van Hunen, J., J. Huang, and S. Zhong (2003). "The effect of shearing on the onset and vigor of small-scale convection in a Newtonian rheology". In: *Geophysical Research Letters* 30.19, p. 1991.

van Keken, P. E., S. D. King, H. Schmeling, U. R. Christensen, D. Neumeister, and M.-P. Doin (1997). "A comparison of methods for the modeling of thermochemical convection". In: *Journal of Geophysical Research* 102.B10, pp. 22477–22495.

van Wijk, J. W., W. S. Baldridge, J. van Hunen, S. Goes, R. Aster, D. D. Coblentz, S. P. Grand, and J. Ni (2010). "Small-scale convection at the edge of the Colorado Plateau: Implications for topography, magmatism, and evolution of Proterozoic lithosphere". In: *Geology* 38.7, pp. 611–614.

van den Berg, A. P., P. E. van Keken, and D. A. Yuen (1992). *The effects of a composite non-Newtonian and Newtonian rheology on mantle convection*. Tech. rep. Minneapolis: University of Minnesota Supercomputer Institute, p. 57.

Chapter 3

Sub-lithospheric small-scale convection—a mechanism for collision zone magmatism[1]

3.1 Introduction

Compared with subduction-related magmatism, mantle-derived collision zone magmatism is still poorly understood. Suggested explanations include increased radiogenic heat production (England and Thompson, 1984), mantle lithosphere delamination (Bird, 1978), slab break-off (Davies and Blanckenburg, 1995), edge-driven convection (Missenard and Cadoux, 2012), and compressional melting due to breakdown of hydrous phases in the thickening mantle lithosphere (Allen et al., 2013). We have studied the dynamics of the post-subduction, syn-collisional mantle with the hypothesis that the upper mantle on the overriding plate side has been hydrated, leading to instability of the lithosphere-asthenosphere boundary, sub-lithospheric small-scale convection (SSC) (Hernlund et al., 2008) and consequent melting. We have compared our model to the volcanic record of the Turkish-Iranian Plateau to explain distinctive features of the volcanism: scattered centers with no clear temporal or spatial patterns and with varying geochemical signatures (e.g. Pearce et al., 1990; Dilek et al., 2010).

3.1.1 Collision Zone Magmatism of the Turkish-Iranian Plateau

Collision of the Arabian and Eurasian plates began at 25–35 Ma with the end of northwards oceanic subduction of Neo-Tethys (see McQuarrie and Hinsbergen, 2013, and references therein).

[1]This chapter has been previously published as Kaislaniemi L., van Hunen J., Allen M. B., Neill I. (2014). *Sub-lithospheric small-scale convection—a mechanism for collision zone magmatism.* Geology, 42 (4). DOI:10.1130/G35193.1. Copyright Geological Society of America, published under the terms of the Creative Commons CC-BY 3.0 license. The numerical experiments were conducted and the manuscript produced by L. Kaislaniemi. The co-authors have participated in the study by providing training, useful discussions and geological knowledge of the regions discussed.

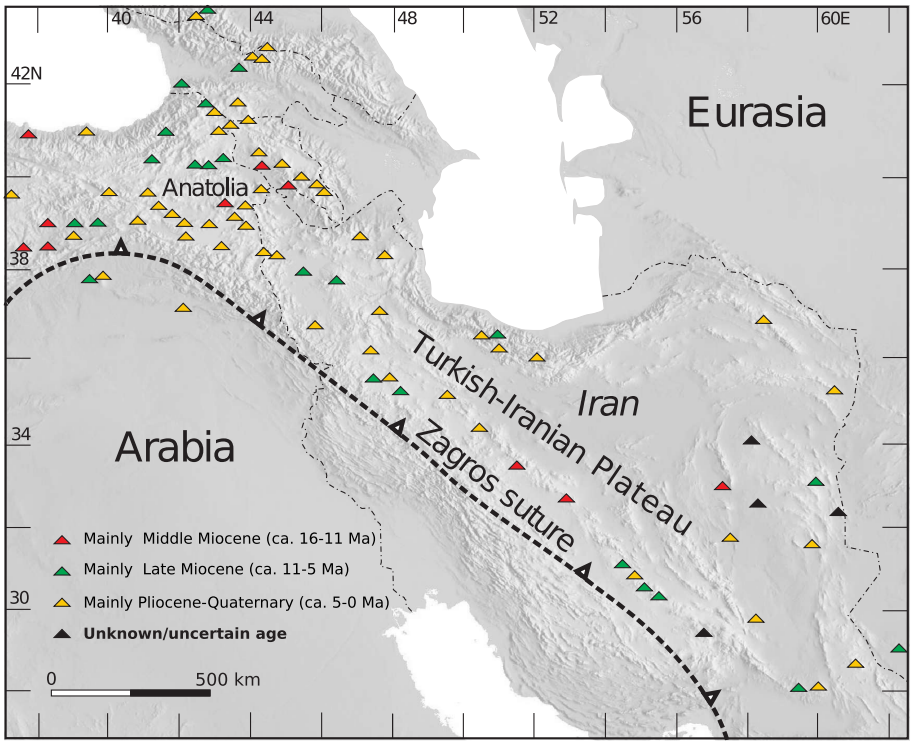

Figure 3.1: Distribution of Middle Miocene to recent (16–0 Ma) volcanic centers of Turkish-Iranian Plateau; background is topography map (modified after Neill et al., 2013). See the Supplemental material for numeric values and references for ages.

Collision has continued to the present day, witnessed by the frequent earthquakes in southwest Asia and current 15–25 mm/yr northwards convergence of Arabia with Eurasia (Vernant et al., 2004). Active crustal thickening and shortening take place at the plateau margins. Following a period of limited Oligocene-Miocene magmatism, there has been an upsurge in magmatic activity across the collision zone in the last few million years (Keskin et al., 1998; Chiu et al., 2013), with widespread if scattered centers focused on the high region with low relief known as the Turkish-Iranian Plateau (Fig. 3.1).

Collision magmatism of the plateau is highly variable in composition, varying from basaltic to rhyolitic, calc-alkaline to alkaline, arc-like to within-plate-like (e.g. Pearce et al., 1990; Keskin et al., 1998; Neill et al., 2013). The most voluminous volcanism is in eastern Anatolia, where thicknesses of the volcanic sequences locally exceed 1 km and cover two thirds of the region, with an average thickness of a few hundred meters (Keskin et al., 1998).

Trace element characteristics of the least-evolved magmas indicate subduction-modified lithospheric mantle sources (high Th/Yb, La/Nb) with or without an ocean island basalt (OIB) -like asthenospheric component (Pearce et al., 1990; Keskin et al., 1998; Neill et al., 2013). Rarer OIB-like centers with low Th/Yb and La/Nb are also found (Pang et al., 2012). Low degree melting ($<<$ 10%) occurred in the spinel stability field or in some cases deeper ($>$ 75 km) in the garnet stability field (Pang et al., 2012; Neill et al., 2013). Some more evolved centers show extensive Sr isotope evidence for crustal contamination (Pearce et al., 1990).

The magmatism has been attributed to slab break-off (Keskin, 2003) and/or lithospheric delamination (e.g. Pearce et al., 1990). Seismic studies give support to these ideas, as the lithosphere at a distance from the suture is relatively thin (< 100 km in eastern Anatolia and adjacent areas) with low shear wave velocities at 100 km depth (Maggi and Priestley, 2005; Angus et al., 2006). However, low seismic velocities could partly be explained by compositional variation (e.g., high fluid content, partial melts) of the lower lithosphere rather than by its absence (Kaviani et al., 2007). Magmatism also occurs in areas with lithosphere >100 km thick (Allen et al., 2013). The nature of slab break-off or delamination mechanisms is such that they would produce spatially and chronologically correlated patterns of magmatism. The propagation of the slab detachment is expected to produce more or less linear segments of magmatism, close to the trench, with a clear time-space relationship (Davies and Blanckenburg, 1995; van Hunen and Allen, 2011). The delamination of the lithospheric mantle as one coherent sliver (sensu Bird, 1978) causes the replacement of lithospheric mantle by asthenospheric mantle and consequent melting, propagating in the direction of the delamination, and waning as the lithosphere cools down. Such features are not clearly observed on the Turkish-Iranian Plateau (Fig. 3.1). Essentially "one-off" events like slab break-off and delamination cannot alone explain magmatism that has a long history and shows no clear patterns in space or in time.

Here we suggest that the irregularity of the long-term syn-collisional magmatism can be explained by small-scale sublithospheric convection, effectively a form of repeated and localized lithosphere delamination or "dripping" (as opposed to one-time regional "catastrophic" delamination), induced by the viscosity- and solidus-lowering effect of water added to the upper mantle by the pre-collision subduction, and possibly enhanced by asthenospheric stirring triggered by slab break-off.

3.2 Water in the mantle

Our model relies on the assumption that the mantle on the overriding plate side has been hydrated during subduction and retains some water left over from melting of the mantle wedge. We assume mantle water contents of 200–600 wt ppm, which lead to viscosity decrease, instability of the LAB, and thus to SSC. The chosen range of water contents exceeds ambient asthenospheric concentrations (i.e., ∼120 wt ppm H_2O for MORB-source mantle (Dixon et al., 2004)), for which no magmatism should be expected. Chosen water contents are still small compared to the amounts causing arc magmatism in active subduction (2,500–10,000 wt ppm, Dixon et al., 2004) and cannot produce arc-like magmatism.

More than 2,000 wt ppm of water can be incorporated into the nominally anhydrous minerals of the mantle peridotite at asthenospheric conditions (Hirschmann et al., 2005). Direct observations from lherzolitic xenoliths have confirmed concentrations of 28–175 wt ppm in the continental lithospheric mantle and based on these observations the maximum water content of primitive mantle is estimated to be 245 wt ppm and 290 wt ppm for garnet and spinel lherzolite, respectively (Bell and Rossman, 1992). The estimated partition coefficients of water led Bell et al. (2004) to conclude that ∼100–200 wt ppm of water could be retained in the wedge melting residues above subduction zones.

Distribution of the hydrated mantle after subduction is unclear, but two observations suggest that elevated upper mantle water contents may exist over a large area and persist for significant periods after subduction has ceased. Firstly, the source regions of the back-arc volcanism of active subduction zones show water content values above MORB source region values even up to 400 km away from the trench (a global compilation of glasses and olivine hosted melt inclusions, Kelley et al., 2006). Secondly, hydrous, potassic volcanism with arc affinities has been observed for tens of millions of years after active subduction thus implying that the mantle can remain hydrated on at least these timescales (e.g. Feldstein and Lange, 1999, and references therein). Wadsleyite, a high-pressure polymorph of olivine, is able to hold up to 20,000 wt ppm water at the mantle transition zone below subduction zones, and could also be a source of water in the upper mantle (Richard and Iwamori, 2010).

3.3 Geodynamic modelling

We quantify the role of lithospheric dripping on magmatism using geodynamic models for the upper mantle and crust, taking into account the role of increased water content on lithosphere stability and melting. The model comprises an initially 100 km thick (1350°C isotherm) lithosphere which represents the overriding plate after active subduction has ceased. The model domain is homogeneously hydrated with various amounts of water, taken to be left over from the previous subduction.

Mantle melting is parameterized using the hydrous peridotite melting model by (Katz et al., 2003), which takes into account the solidus lowering effect of water at varying pressure. Water is handled as an incompatible element with bulk distribution coefficient D = 0.01 and is removed with the melt at each timestep using a batch melting model. Melt depletion affects the mantle density by making it more buoyant (Schutt and Lesher, 2006).

We take into account the effect of water on mantle rheology (e.g. Hirth and Kohlstedt, 2003). We parameterize the weakening with

$$\eta_{\text{hydrous}} = W\eta_{\text{dry}}, \text{ where } W = 100^{-X_{\text{H}_2\text{O}}/(X_{\text{H}_2\text{O}}+a)}, \tag{3.1}$$

where $X_{\text{H}_2\text{O}}$ (wt ppm) is the bulk water content and a (wt ppm) is the water sensitivity parameter controlling how large $X_{\text{H}_2\text{O}}$ needs to be to decrease the viscosity by factor of 10. This parameterization is constrained by experimental results showing that viscosity in hydrous olivine aggregates decreases exponentially with the water fugacity, and that the maximum difference between dry and water saturated viscosities is about two orders of magnitude (Hirth and Kohlstedt, 2003). The water sensitivity parameter captures the effects of multiple physical parameters (value of the exponent; water content and water fugacity relationship; water partitioning between mantle minerals) and their uncertainties, but has a clear physical meaning (rheological sensitivity to water), thus allowing an easier parameter study of the effects of water on the formation of SSC. We use values of 200-500 ppm for a, leading to viscosity weakening of 0.7 to 1.4 orders of magnitude. The lower boundary is restricted by assuming that ambient mantle water contents should not lead to

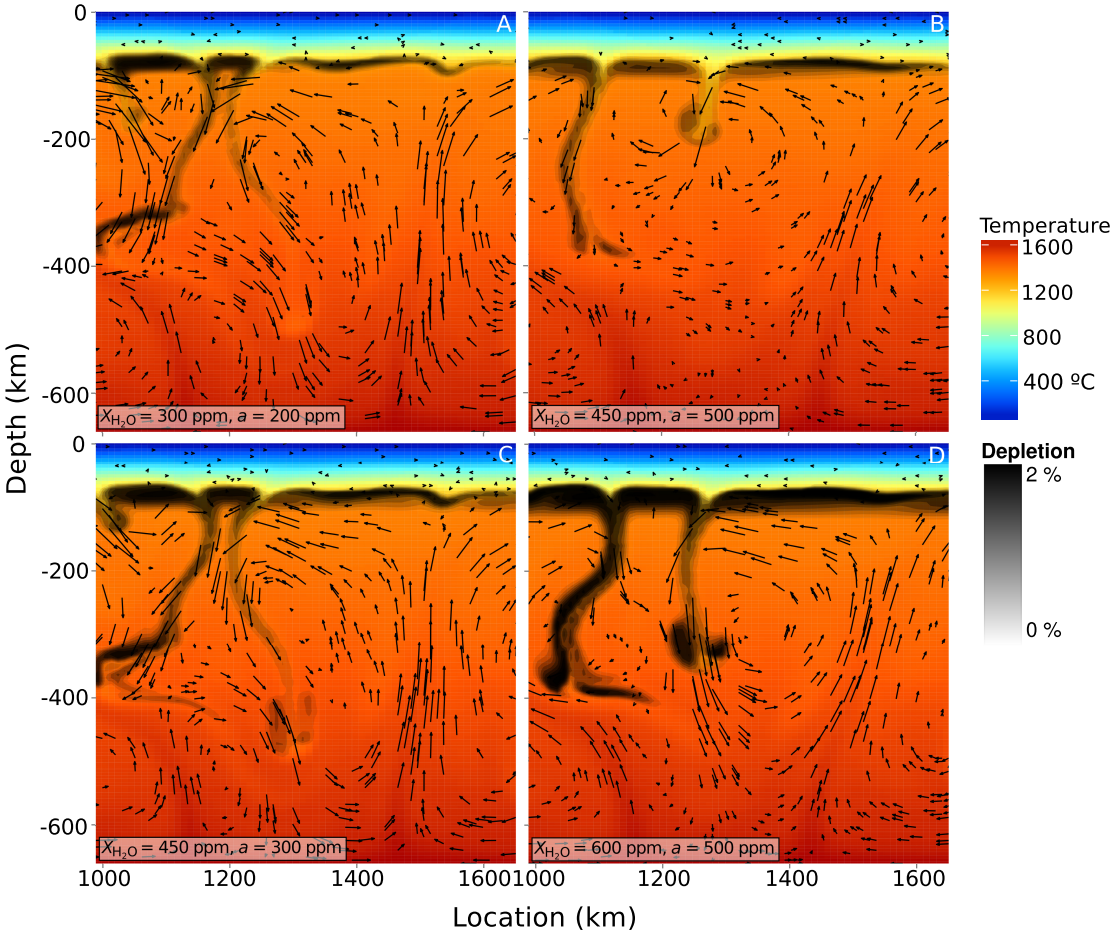

Figure 3.2: Detailed view of model domain showing temperature, velocity (arrows), and depletion fields at time = 15 Ma with different water sensitivity parameters (a) and water content. Models shown correspond to models circled in Figure 3.4.

significant weakening, whereas values of a $>$ 500 ppm do not change the results significantly compared to the case of a = 500 ppm. The viscosity parameterization leads to minimum effective dry asthenospheric viscosities of 5×10^{19} Pa s. For detailed method description, see the supplementary information.

3.4 Modeling results

Reduced viscosity, due to the elevated water content, increases the vigor of convection, leads to instability of the base of the lithosphere, and so to "dripping" of the lithosphere into the underlying asthenosphere. There is no significant permanent thinning of the lithosphere. A small scale convection (SSC) pattern forms at the lithosphere-asthenosphere boundary (Fig. 3.2), with convection cell diameters ranging from $<$ 100–300 km. This convection makes decompression melting of the asthenosphere possible. The viscosity of the melt-depleted mantle material increases because of the partial removal of the water with the partial melts. Depleted mantle, being more

viscous and more buoyant, adheres to the bottom of the lithosphere for a while before being removed by the convection. This can cause the melting in the convection cell to pause. The convection cells migrate laterally, so that the locations of decompression melting also change; the behavior is seemingly random.

Plotting the rate of volcanism against time and location (Fig. 3.3) shows a non-regular pattern, where the volcanic centers are active from less than couple of million years up to tens of millions of years, and can have significant time lags after the start of the post-subduction period. Production rates vary between less than 20 m/Ma up to hundreds of meters per Ma. In all estimates of the volume or production rate of the volcanism in our results, mantle melts are assumed to percolate directly and instantaneously to the surface, forming a volcanic layer with average thickness V_{avgthck}. In reality, only a certain proportion of the melts produced contribute to the extrusions visible at the surface. The total volume of melt produced for different values of a and $X_{\mathrm{H_2O}}$ is shown in Figure 3.4.

3.5 Discussion

The temporal and spatial patterns of magma production (Fig. 3.3) are irregular but all have dominating spatial wavelengths of ∼200 km (FFT analysis, see supplementary information). This corresponds to the typical distances (vertical axis in Fig. 3.3) between larger volcanic centers in the models. Reactivation time (distance in time, horizontal axis in Fig. 3) of the larger volcanic centers depends on the total viscosity decrease, but generally range from 5 to 20 Ma. With lower H_2O dependency of viscosity, the volcanic centers tend to have longer, more diffuse, lifespans, whereas higher H_2O dependency produces shorter lifespans with more frequent reactivation (e.g., Figure 3.3A vs 3.3B).

This irregular pattern of volcanism is the most striking feature common to both our models and the volcanism of the Turkish-Iranian Plateau. The appearance of a volcanic center millions of years after the initial collision can be simply explained by the chaotic nature of the SSC. The heterogeneous chemical signature of the volcanism, a result of variable asthenospheric and lithospheric mantle contributions to melting, can be explained by the SSC effectively mixing lithosphere with asthenosphere near the spinel-garnet transition zone. In addition to the decompression melting, convection advectively heats the lithosphere, and can aid the compressional melting of hydrous phases of the lithosphere as it is being "dripped" down to the asthenosphere.

The most voluminous volcanism of the plateau, in Eastern Anatolia, covers two thirds of the area and averages perhaps a few hundred meters in thickness (e.g. Keskin et al., 1998). These amounts can be reproduced with many combinations of water content and water sensitivity (Fig. 3.4), even if intrusive magmatism is significant in amount, showing that SSC is a viable mechanism for the volcanism, regardless of the uncertainties in water content and parameter a.

The thinning of the thermal lithosphere is too minor to produce significant uplift. More importantly, SSC can lead to localized thinning of the lithosphere, thus creating favorable conditions for the start of complete ("catastrophic") mantle delamination, as described by Morency and Doin (2004). Nevertheless, our results show that no whole mantle delamination is required to produce

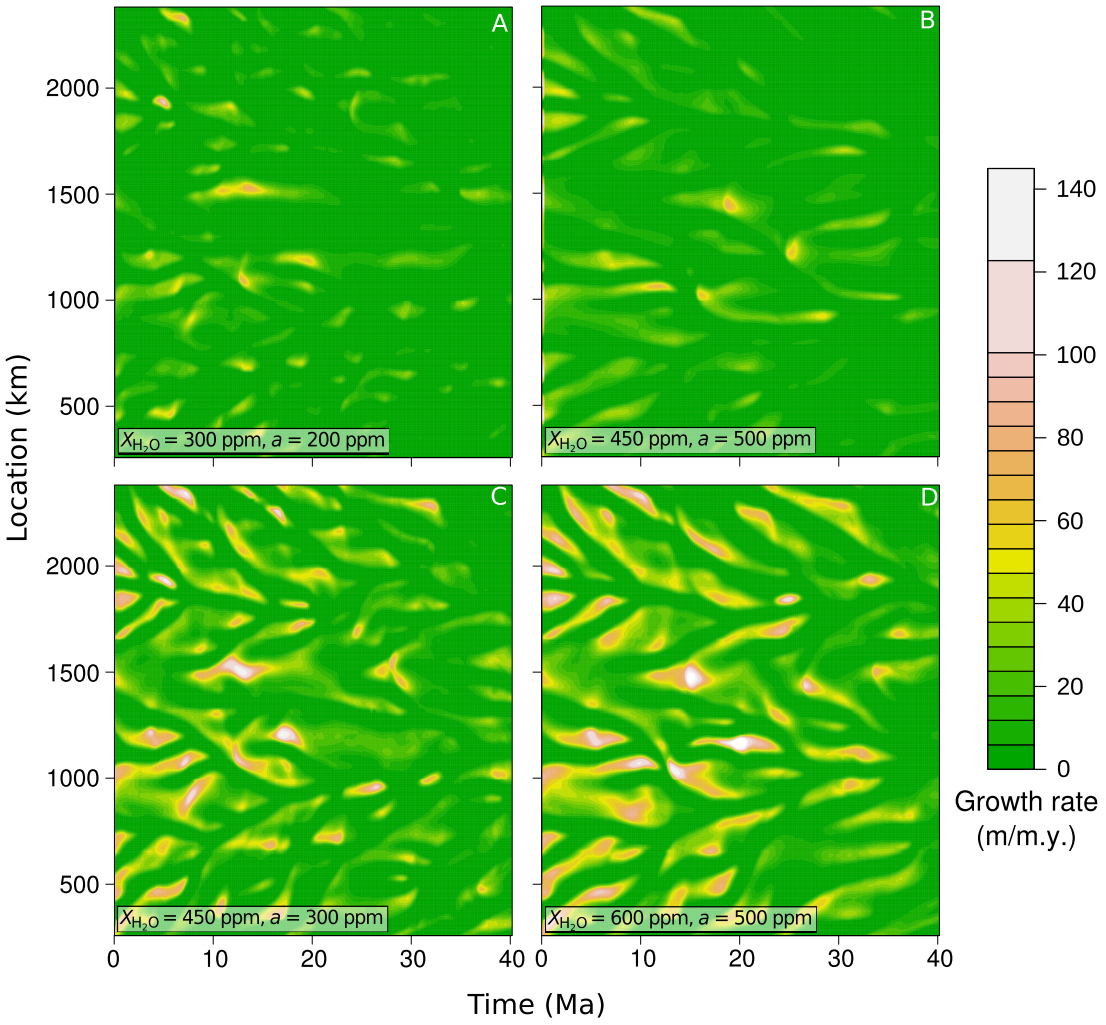

Figure 3.3: Rate of volcanism (assuming extrusive magmatism only) with different water sensitivity parameters (a) and water content. Magmatism distributed laterally over the model domain (vertical axis) is plotted against time (horizontal axis). Models shown correspond to those in Figure 3.2 and to models circled in Figure 3.4.

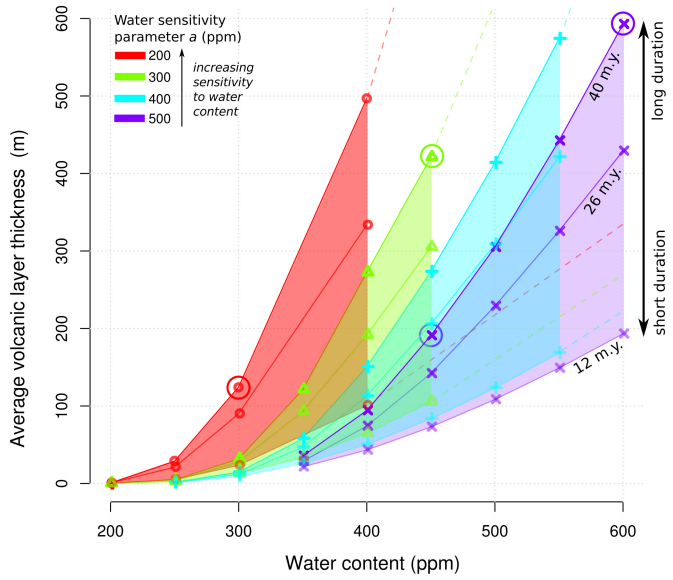

Figure 3.4: Average thickness of volcanic rocks as function of water sensitivity parameter a, initial amount of water in mantle, and model run duration. Dashed lines show extrapolation to unexplored region of parameter space. Models used in Figures 3.2 and 3.3 are circled.

voluminous collision zone volcanism. An extended period of magmatism (tens of millions of years) after the onset of continental collision is an inherent feature of the water-induced instability of the LAB and sub-lithospheric SSC, and requires no other explanation than the input of water to the lithospheric and asthenospheric mantle during previous subduction. SSC could be enhanced by slab break-off or wholesale lithospheric mantle delamination, but neither of these is prerequisite for SSC and the resultant magmatism.

The general mechanism of water weakening and volcanism produced by SSC could also be applied at a larger scale to the "anorogenic" igneous activity of the circum-Mediterranean region (Lustrino and Wilson, 2007), where large areas of mantle transition zone might have been hydrated by the Mediterranean subduction zones (Nolet and Zielhuis, 1994). We furthermore suggest applications of this model for the Tibetan Plateau, where localized magmatism has been a persistent feature of the India-Eurasia collision zone (Chung et al., 2005). More generally, occurrence of long-lasting magmatism without self-evident tectonic cause, sedimentation or faulting can be explained by the activation of the most basal lithosphere whenever enough water is present, without the need to involve different theories for the cause of each volcanic center separately.

References

Allen, M. B., M. Kheirkhah, I. Neill, M. H. Emami, and C. L. Mcleod (2013). "Generation of Arc and Within-plate Chemical Signatures in Collision Zone Magmatism: Quaternary Lavas from Kurdistan Province, Iran". In: *Journal of Petrology* 54.5, pp. 887–911.

Angus, D. A., D. C. Wilson, E. Sandvol, and J. F. Ni (2006). "Lithospheric structure of the Arabian and Eurasian collision zone in eastern Turkey from S -wave receiver functions". In: *Geophysical Journal International* 166.3, pp. 1335–1346.

Bell, D. R. and G. R. Rossman (1992). "Water in Earth's mantle: The Role of Nominally Anhydrous Minerals". In: *Science* 255.5050, pp. 1391–1397.

Bell, D. R., G. R. Rossman, and R. O. Moore (2004). "Abundance and Partitioning of OH in a High-pressure Magmatic System: Megacrysts from the Monastery Kimberlite, South Africa". In: *Journal of Petrology* 45.8, pp. 1539–1564.

Bird, P. (1978). "Initiation of intracontinental subduction in the Himalaya". In: *Journal of Geophysical Research* 85.B10, pp. 4975–4987.

Chiu, H.-Y., S.-L. Chung, M. H. Zarrinkoub, S. S. Mohammadi, M. M. Khatib, and Y. Iizuka (2013). "Zircon U-Pb age constraints from Iran on the magmatic evolution related to Neotethyan subduction and Zagros orogeny". In: *Lithos* 162-163, pp. 70–87.

Chung, S.-L., M.-F. Chu, Y. Zhang, Y. Xie, C.-H. Lo, T.-Y. Lee, C.-Y. Lan, X. Li, Q. Zhang, and Y. Wang (2005). "Tibetan tectonic evolution inferred from spatial and temporal variations in post-collisional magmatism". In: *Earth-Science Reviews* 68.3-4, pp. 173–196.

Davies, J. H. and F. von Blanckenburg (1995). "Slab breakoff: A model of lithosphere detachment and its test in the magmatism and deformation of collisional orogens". In: *Earth and Planetary Science Letters* 129.1-4, pp. 85–102.

Dilek, Y., N. Imamverdiyev, and c. Altunkaynak (2010). "Geochemistry and tectonics of Cenozoic volcanism in the Lesser Caucasus (Azerbaijan) and the peri-Arabian region: collision-induced mantle dynamics and its magmatic fingerprint". In: *International Geology Review* 52.4-6, pp. 536–578.

Dixon, J. E., T. H. Dixon, D. R. Bell, and R Malservisi (2004). "Lateral variation in upper mantle viscosity: role of water". In: *Earth and Planetary Science Letters* 222.2, pp. 451–467.

England, P. C. and A. B. Thompson (1984). "Pressure-Temperature-Time Paths of Regional Metamorphism I. Heat Transfer during the Evolution of Regions of Thickened Continental Crust". In: *Journal of Petrology* 25.4, pp. 894–928.

Feldstein, S. N. and R. A. Lange (1999). "Pliocene Potassic Magmas from the Kings River Region, Sierra Nevada, California: Evidence for Melting of a Subduction-Modified Mantle". In: *Journal of Petrology* 40.8, pp. 1301–1320.

Hernlund, J. W., P. J. Tackley, and D. J. Stevenson (2008). "Buoyant melting instabilities beneath extending lithosphere: 1. Numerical models". In: *Journal of Geophysical Research* 113.B4, B04405.

Hirschmann, M. M., C. Aubaud, and A. C. Withers (2005). "Storage capacity of H2O in nominally anhydrous minerals in the upper mantle". In: *Earth and Planetary Science Letters* 236.1-2, pp. 167–181.

Hirth, G. and D. Kohlstedt (2003). "Rheology of the Upper Mantle and the Mantle Wedge: A view from the Experimentalists". In: *Geophysical Monograph* 183, pp. 83–105.

Katz, R. F., M. Spiegelman, and C. H. Langmuir (2003). "A new parameterization of hydrous mantle melting". In: *Geochemistry Geophysics Geosystems* 4.9, p. 1073.

Kaviani, A., A. Paul, E. Bourova, D. Hatzfeld, H. Pedersen, and M. Mokhtari (2007). "A strong seismic velocity contrast in the shallow mantle across the Zagros collision zone (Iran)". In: *Geophysical Journal International* 171, pp. 399–410.

Kelley, K. A., T. Plank, T. L. Grove, E. M. Stolper, S. Newman, and E. Hauri (2006). "Mantle melting as a function of water content beneath back-arc basins". In: *Journal of Geophysical Research* 111.B9, B09208.

Keskin, M., J. A. Pearce, and J. G. Mitchell (1998). "Volcano-stratigraphy and geochemistry of collision-related volcanism on the Erzurum-Kars Plateau, northeastern Turkey". In: *Journal of Volcanology and Geothermal Research* 85.1-4, pp. 355–404.

Keskin, M. (2003). "Magma generation by slab steepening and breakoff beneath a subduction-accretion complex: An alternative model for collision-related volcanism in Eastern Anatolia, Turkey". In: *Geophysical Research Letters* 30.24, pp. 7–10.

Lustrino, M. and M. Wilson (2007). "The circum-Mediterranean anorogenic Cenozoic igneous province". In: *Earth-Science Reviews* 81.1-2, pp. 1–65.

Maggi, A. and K. Priestley (2005). "Surface waveform tomography of the Turkish-Iranian plateau". In: *Geophysical Journal International* 160.3, pp. 1068–1080.

McQuarrie, N. and D. J. J. van Hinsbergen (2013). "Retrodeforming the Arabia-Eurasia collision zone: Age of collision versus magnitude of continental subduction". In: *Geology* 41.3, pp. 315–318.

Missenard, Y. and A. Cadoux (2012). "Can Moroccan Atlas lithospheric thinning and volcanism be induced by Edge-Driven Convection?" In: *Terra Nova* 24.1, pp. 27–33.

Morency, C. and M.-P. Doin (2004). "Numerical simulations of the mantle lithosphere delamination". In: *Journal of Geophysical Research* 109.B3, B03410.

Neill, I., K. Meliksetian, M. Allen, G. Navarsardyan, and S. Karapetyan (2013). "Pliocene-Quaternary volcanic rocks of NW Armenia: Magmatism and lithospheric dynamics within an active orogenic plateau". In: *Lithos* 180-181, pp. 200–215.

Nolet, G. and A. Zielhuis (1994). "Low S velocities under the Tornquist-Teisseyre zone: Evidence for water injection into the transition zone by subduction". In: *Journal of Geophysical Research* 99.B8, pp. 15813–15820.

Pang, K.-N., S.-L. Chung, M. H. Zarrinkoub, S. S. Mohammadi, H.-M. Yang, C.-H. Chu, H.-Y. Lee, and C.-H. Lo (2012). "Age, geochemical characteristics and petrogenesis of Late Cenozoic intraplate alkali basalts in the Lut-Sistan region, eastern Iran". In: *Chemical Geology* 306-307, pp. 40–53.

Pearce, J. A., J. F. Bender, S. E. Delong, W. S. F. Kidd, P. J. Low, Y. Guner, F. Saroglu, Y. Yilmaz, S. Moorbath, and J. G. Mitchell (1990). "Genesis of collision volcanism in Eastern Anatolia, Turkey". In: *Journal of Volcanology and Geothermal Research* 44.1-2, pp. 189–229.

Richard, G. C. and H. Iwamori (2010). "Stagnant slab , wet plumes and Cenozoic volcanism in East Asia". In: 183, pp. 280–287.

Schutt, D. L. and C. E. Lesher (2006). "Effects of melt depletion on the density and seismic velocity of garnet and spinel lherzolite". In: *Journal of Geophysical Research* 111.B5, pp. 1–24.

Vernant, P., F. Nilforoushan, D. Hatzfeld, M. R. Abbassi, C. Vigny, F. Masson, H. Nankali, J. Martinod, A. Ashtiani, R. Bayer, et al. (2004). "Present-day crustal deformation and plate kinematics in the Middle East constrained by GPS measurements in Iran and northern Oman". In: *Geophysical Journal International* 157.1, pp. 381–398.

van Hunen, J. and M. B. Allen (2011). "Continental collision and slab break-off: A comparison of 3-D numerical models with observations". In: *Earth and Planetary Science Letters* 302.1-2, pp. 27–37.

Supplemental material

Following is the supplemental material published together with the original publication, Kaislaniemi et al., 2014, *Sub-lithospheric small-scale convection—a mechanism for collision zone magmatism*, Geology, 42 (4).

Supplemental information for "Sub-lithospheric small scale convection — a mechanism for collision zone magmatism"

L. Kaislaniemi[a,*], J. van Hunen[a], M. B. Allen[a], I. Neill[a]

[a] Department of Earth Sciences, Durham University, Science Labs, Durham, DH1 3LE, United Kingdom

Contents

1 Equations and numerical modelling

We solve the non-dimensional equations of conservation of mass, momentum, and energy using finite element mantle convection code Citcom (Moresi and Gurnis, 1996; Zhong et al., 2000). The extended Boussinesq approximation (Christensen and Yuen, 1985) is used to account for shear heating, adiabatic heating, and the latent heat of melting. Equations applied are:

$$\nabla \cdot \mathbf{u} = 0\,, \tag{1}$$

$$\nabla \left[\eta(\nabla \mathbf{u} + \nabla^{\mathrm{T}}\mathbf{u})\right] - \nabla \cdot P = -RaT \cdot \hat{\mathbf{e}}_{\mathbf{z}} - RbF \cdot \hat{\mathbf{e}}_{\mathbf{z}}\,, \text{ and} \tag{2}$$

$$\frac{\partial T}{\partial t} + \mathbf{u} \cdot \nabla T = \nabla^2 T + L\left(\frac{\partial F}{\partial t} + \mathbf{u} \cdot \nabla F\right) + \frac{Di}{Ra}\eta\dot{\epsilon}^2 + Di(T + T_s)u_z\,, \tag{3}$$

where $\mathbf{u}$ is the velocity vector, η viscosity, P deviatoric pressure, Ra thermal Rayleigh number, T temperature,$\hat{\mathbf{e}}_{\mathbf{z}}$ vertical unit vector, Rb compositional (depletion) Rayleigh number, F depletion, t time, L latent heat of melt, Di dissipation number, ϵ strain, and T_s the surface temperature. Used values of all the parameters are given in Table 1. The advection of compositional field (depletion and water content) and heat is implemented using the marker-in-cell method (e.g. Gerya and Yuen, 2003) with a second order Runge-Kutta scheme.

*Corresponding author. E-mail address: lars.kaislaniemi@iki.fi

Rayleigh numbers are defined as

$$Ra = \frac{\alpha T_0 \rho_0 g h^3}{\kappa \eta_0}\,, \tag{4}$$

$$Rb = \frac{\Delta\rho_F g h^3}{\kappa \eta_0}\,, \tag{5}$$

where α is the thermal expansivity, T_0 reference temperature, ρ_0 reference density, g gravity acceleration, h model height, κ thermal diffusivity, and η_0 reference viscosity. $\Delta\rho_F$ is the density change due to depletion, which is given by

$$\frac{\mathrm{d}\ln\rho}{\mathrm{d}F_{\%}} = -0.00020 \tag{6}$$

from Schutt and Lesher (2006), where $F_{\%} = 100F$ is the depletion in percentage, and $\rho = \rho_0$ (reference density) when $F_{\%} = 0$. The chosen value of -0.00020 is representative of asthenospheric conditions in our models (about 3 GPa).

The dissipation number is defined as

$$Di = \frac{\alpha g h}{C_p}\,, \tag{7}$$

where C_p is the constant pressure heat capacity of the mantle.

1.1 Viscosity parametrization and water weakening

Viscosity parametrization is linear with temperature dependency (Karato and Wu, 1993):

$$\eta_{dry} = A \exp\left(\frac{E + PV}{RT_{abs}}\right)\,, \tag{8}$$

where A is the rheological pre-exponent, E activation energy, V activation volume, R universal gas constant, and T_{abs} the absolute temperature. We use a low value of activation energy ($E = 150\,\mathrm{kJ/mol}$), in order to mimic the effect of dislocation creep. This is in line with the results of Christensen (1984), who proposes that 50 to 70 percent smaller values of activation enthalpy should be used, and van Hunen et al. (2005) who found that value $E = 120\,\mathrm{kJ/mol}$ produces similar lithospheric erosion effect to nonlinear viscosity models.

The effective hydrous viscosity

$$\eta_{hydrous} = W\eta_{dry} \tag{9}$$

with

$$W = 100^{\frac{-X_{H2O}}{X_{H2O+a}}} \tag{10}$$

produces exponential viscosity decrease and maximum weakening of two orders of magnitude (compared to the dry mantle), compatible with experimental results showing that for olivine aggregates the strain rate $\dot{\epsilon} \propto f_{H_2O}^r$, that is, the viscosity $\eta \propto f_{H_2O}^{-r}$, where r is constant, and f_{H_2O} is the water fugacity (Bai and Kohlstedt, 1992; Mei and Kohlstedt, 2000; Hirth and Kohlstedt, 2003). The experimental results have, to some extent, constrained the values of the exponent r (about 1.0 ± 0.2), the relationship between water content and water fugacity (nearly linear at low olivine water contents), and the partitioning of bulk water content between mantle minerals. However, uncertainties related to the effect of water on mantle rheology still remain, and by using a simpler relationship (eq. 10), we can adjust the sensitivity of mantle rheology to the water content in our models to more easily perform parameter studies. Additional advantage of our formulation is that, whereas in experimentally constrained relationships, two rheologies are needed (one for dry, one for hydrous rheology, because in hydrous rheology law viscosity approaches infinity as water fugacity approaches zero), we can model both wet and dry or nearly dry cases using the same law.

Symbol	Definition	Value
L	Latent heat of melt	$560\,\mathrm{kJ\,kg^{-1}}$
α	Coefficient of thermal expansion	$3.5 \cdot 10^{-5}\,\mathrm{K^{-1}}$
T_0	Reference temperature	1350°C
ρ_0	Reference density	$3300\,\mathrm{kg\,m^{-3}}$
h	Model height	660 km
κ	Thermal diffusivity	$10^{-6}\,\mathrm{m^2 s^{-1}}$
η_0	Reference viscosity	$10^{22}\,\mathrm{Pa\,s}$
C_p	Constant pressure heat capacity	$1250\,\mathrm{J\,kg^{-1}\,K^{-1}}$
A	Rheological pre-exponent	$1.82 \cdot 10^{14}\,\mathrm{Pa\,s}$
E	Activation energy	$150\,\mathrm{kJ\,mol^{-1}}$
V	Activation volume	$4\,\mathrm{cm^3\,mol^{-1}}$
a	Viscosity's sensitivity to water	200–500 ppm
X_{H_2O}	Mantle water content	200–600 ppm

Used model parameters and their dimensional values.

The range of a used in the models is determined by two factors: The lower boundary is chosen so that ambient mantle water contents (outside subduction modified regions) would not cause too high viscosity weakening, thus limiting the lower boundary to values clearly larger than 120 ppm (approximate MORB source region water contents). The upper boundary is chosen such that results with higher values do not significantly differ from the highest value used. This indifference of results to parameter a happens because as a grows, the form of W approaches linearity, and the greatest variation in the form of W is seen when values of a are in the range from zero to about 500 ppm.

1.2 Benchmarking

The code used has been succesfully benchmarked against the results of Blankenbach et al. (1989) (Boussinesq approximation) and King et al. (2010) (Extended Boussinesq approximation).

1.3 Model domain, boundary conditions

Our cartesian model domain is 660 km in height and 2640 km in width (aspect ratio 1:4). All the boundaries are closed with free-slip boundary conditions. Heat flow is zero at the horizontal boundaries, and $T = 0$ (0°C) at the surface and $T = 1.25254$ (1690°C) at the bottom. Initial temperature field is provided by running one of the models ($X_{H_2O} = 200$ ppm, $a = 200$ ppm) for $>$ 300 Ma model time to a statistical steady state, with melting disabled, resulting in a more or less flat, approximately 100 km thick high viscosity lithosphere, and restarting this model with new values of X_{H_2O} and a and with melting enabled. The initial temperature field has a mantle potential temperature of about 1300°C.

Model domain has been discretized in to 256 elements in x-direction and 128 elements in z-direction.

1.4 Processing of numerical results

The melt generation within the mantle has been recorded, excluding the proximity of horizontal boundaries, where closed boundaries tend to produce anomalously strong upwelling in some models, leading to high decompressional melting rate.

We analyze the resulting crust production array (rate of melting plotted against time on x-axis and location on y-axis) using multivariate (2D) Fast Fourier Transformation (FFT). For this we use the `fft` routine of the statistical computing software `R` (R Core Team, 2013; Singleton, 1979). Except for very low crust production models, the FFTs show clear maxima between 0.2 to 0.0 1/Ma (5 to Infinite Ma) and between 0.007 and 0.002 1/km (140 km to 500 km) (e.g. Figure S1). The point of maximum amplitude vary slightly among models but with no clear systematics. All models with enough crust production (more than about 50 m average overall crustal production after 40 Myrs) to do the FFT analysis, show a maximum at 0.005 1/km (200 km spatial wavelength), and the location of this maximum on the x-axis (time) vary between 0.05 1/Ma and 0.2 1/Ma (5 to 20 Ma temporal wavelength).

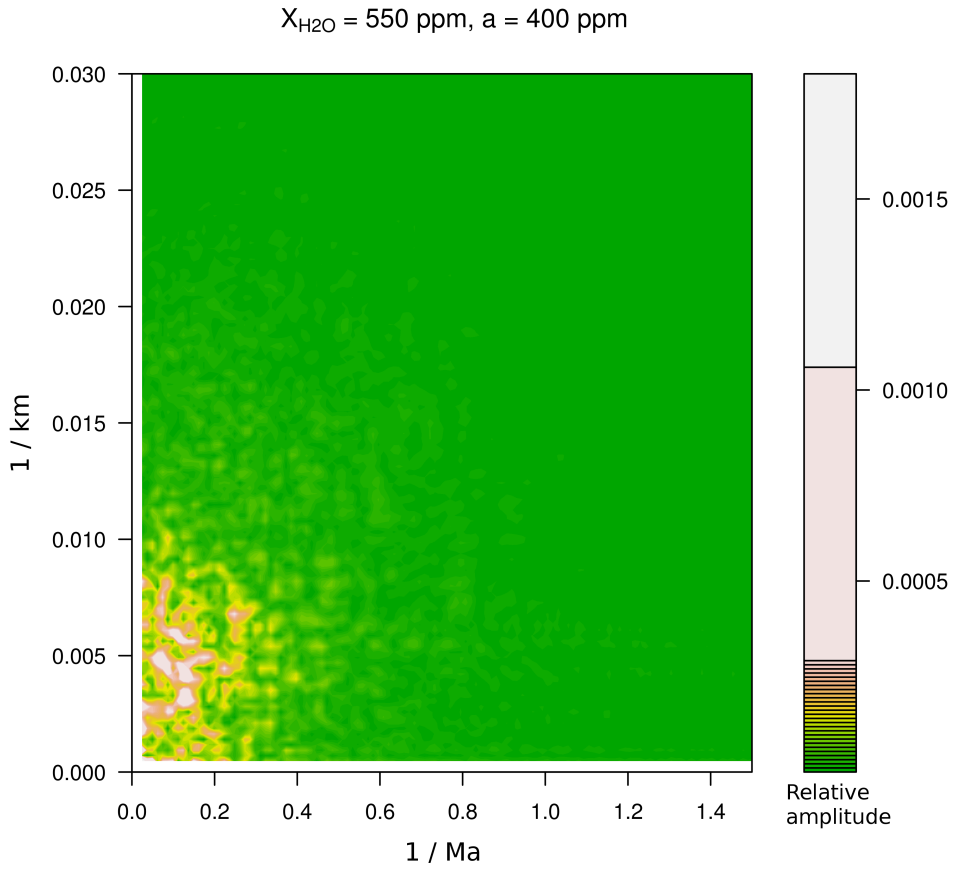

Figure S1: 2D FFT of the crust production array for the model $X_{H2O} = 550\,\text{ppm}$, $a = 400\,\text{ppm}$.

References

Bai, Q., Kohlstedt, D., May 1992. High-temperature creep of olivine single crystals, 2. dislocation structures. Tectonophysics 206 (1-2), 1–29.
URL http://linkinghub.elsevier.com/retrieve/pii/004019519290365D

Blankenbach, B., Busse, F., Christensen, U., Cserepes, L., Gunkel, D., Hansen, U., Harder, H., Jarvis, G., Koch, M., Marquart, G., Moore, D., Olson, P., Schmeling, H., Schnaubelt, T., 1989. A benchmark comparison for mantle convection codes. Geophysical Journal International 98 (1989), 23–38.

Christensen, U., 1984. Convection with pressure- and temperature-dependent non-Newtonian rheology. Geophysical Journal of the Royal Astronomical Society 77, 343–384.

Christensen, U. R., Yuen, D. A., 1985. Layered Convection Induced by Phase Transitions. Journal of Geophysical Research 90 (B12), 10291–10300.

Gerya, T. V., Yuen, D. a., Dec. 2003. Characteristics-based marker-in-cell method with conservative finite-differences schemes for modeling geological flows with strongly variable transport properties. Physics of the Earth and Planetary Interiors 140 (4), 293–318.
URL http://linkinghub.elsevier.com/retrieve/pii/S0031920103001900

Hirth, G., Kohlstedt, D., 2003. Rheology of the Upper Mantle and the Mantle Wedge: A view from the Experimentalists. Geophysical Monograph 183, 83–105.

Karato, S.-I., Wu, P., 1993. Rheology of the Upper Mantle: A Synthesis. Science 260 (5109), 771–778.

King, S. D., Lee, C., van Keken, P. E., Leng, W., Zhong, S., Tan, E., Tosi, N., Kameyama, M. C., 2010. A community benchmark for 2-D Cartesian compressible convection in the Earth's mantle.

Mei, S., Kohlstedt, D., 2000. Influence of water on plastic deformation of olivine aggregates 1 . Diffusion creep regime. Journal of Geophysical Research 105, 21457–21469.

Moresi, L., Gurnis, M., 1996. Constraints on the lateral strength of slabs from three-dimensional dynamic flow models. Earth and Planetary Science Letters 138, 15–28.

R Core Team, 2013. R: A Language and Environment for Statistical Computing. R Foundation for Statistical Computing, Vienna, Austria.
URL http://www.r-project.org

Schutt, D. L., Lesher, C. E., 2006. Effects of melt depletion on the density and seismic velocity of garnet and spinel lherzolite. Journal of Geophysical Research 111 (B5), 1–24.
URL http://www.agu.org/pubs/crossref/2006/2003JB002950.shtml

Singleton, R. C., 1979. Mixed Radix Fast Fourier Transforms. In: Committee, I. D. S. P. (Ed.), Programs for digital signal processing. IEEE Press, New York.

van Hunen, J., Zhong, S., Shapiro, N., Ritzwoller, M., Sep. 2005. New evidence for dislocation creep from 3-D geodynamic modeling of the Pacific upper mantle structure. Earth and Planetary Science Letters 238 (1-2), 146–155.
URL http://linkinghub.elsevier.com/retrieve/pii/S0012821X05004619

Zhong, S., Zuber, M. T., Moresi, L., Gurnis, M., 2000. Role of temperature-dependent viscosity and surface plates in spherical shell models of mantle convection. Journal of Geophysical Research 105 (B5), 11063–11082.

2 Volcanism of the Turkish-Iranian plateau

2.1 Numeric ages and their sources

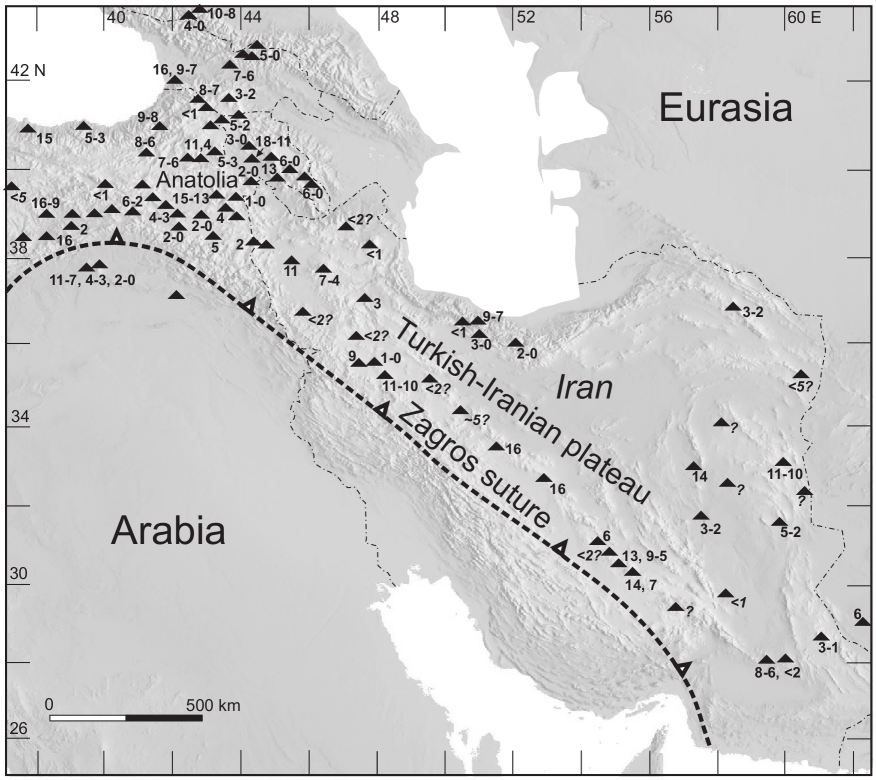

Figure S2: Ages of the volcanic centres shown in Figure 1 in the main text.

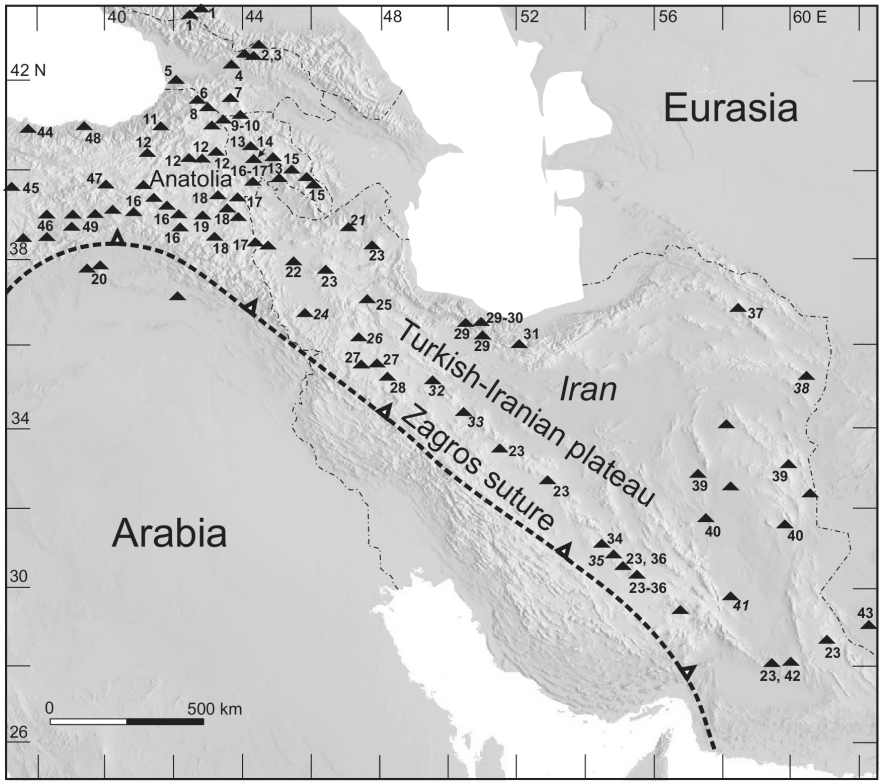

Figure S3: References of the volcanic centre ages shown in Figure S2 and Figure 1 in the main text.

Sources for the ages / references in Figure S2/S3:

1 – Lebedev et al (2006)	26 – Zahedi and Hajian (1985)
2 – Lebedev et al (2006)	27 – Boccaletti et al (1976)
3 – Lebedev et al (2011)	28 – Richards et al (2006)
4 – Lebedev et al (2013)	29 – Guest et al (2007)
5 – Lebedev et al (2009)	30 – Axen et al (2001)
6 – Lebedev et al (2012)	31 – Davidson et al (2004)
7 – Lebedev et al (2007)	32 – Alai-Mahabadi and Khalatbari-Jafari (2003)
8 – Chernyshev et al (2006)	33 – Emami (1981)
9 – Lebedev et al (2008a)	34 – Kouhestani et al (2012)
10 – Lebedev et al (2008b)	35 – Djokovic et al (1973)
11 – Eyuboglu et al (2012)	36 – McInnes et al (2005)
12 – Keskin et al (1998)	37 – Shabanian et al (2009)
13 – Mitchell and Westaway (1999)	38 – Saadat and Stern (2012)
14 – Karapetian et al (2001)	39 – Pang et al (2012)
15 – Arutyunyan et al (2007)	40 – Walker et al (2009)
16 – Pearce et al (1990)	41 – Milton (1977)
17 – Allen et al (2011)	42 – Saadat and Stern (2011)
18 – Lebedev et al (2010)	43 – Richards et al (2012)
19 – Innocenti et al (1976)	44 – Temizel et al (2012)
20 – Keskin et al (2012)	45 – Parlak et al (2001)
21 – Dabiri et al (2011)	46 – Kurum et al (2008)
22 – Pang et al (2013)	47 – Karsli et al (2008)
23 – Chiu et al (2013)	48 – Aydin et al (2008)
24 – Eftekharnezhad (1973)	49 – Arger et al (2000)
25 – Hassanzadeh et al (2008)	

2.2 References

Alai-Mahabadi, S., and Khalatbari-Jafari, B. M., 2003, Noubaran: Geological survey of Iran, scale 1:100,000.

Allen, M. B., Mark, D. F., Kheirkhah, M., Barfod, D., Emami, M. H., and Saville, C., 2011, 40Ar/39Ar dating of Quaternary lavas in northwest Iran: constraints on the landscape evolution and incision rates of the Turkish-Iranian plateau: Geophysical Journal International, v. 185, no. 3, p. 1175-1188.

Arger, J., Mitchell, J., and Westaway, R. W. C., 2000, Neogene and Quaternary volcanism of southeastern Turkey, in Bozkurt, E., Winchester, J. A., and Piper, J. D. A., eds., Tectonics and Magmatism in Turkey and the Surrounding Area, Volume 173: London, Geological Society, London, p. 459-487.

Arutyunyan, E. V., Lebedev, V. A., Chernyshev, I. V., and Sagatelyan, A. K., 2007, Geochronology of Neogene-Quaternary volcanism of the Geghama Highland (Lesser Caucasus, Armenia): Doklady Earth Sciences, v. 416, no. 7, p. 1042-1046.

Axen, G. J., Lam, P. S., Grove, M., Stockli, D. F., and Hassanzadeh, J., 2001, Exhumation of the west-central Alborz Mountains, Iran, Caspian subsidence, and collision-related tectonics: Geology, v. 29, p. 559-562.

Aydin, F., Karsli, O., and Chen, B., 2008, Petrogenesis of the Neogene alkaline volcanics with implications for post-collisional lithospheric thinning of the Eastern Pontides, NE Turkey: Lithos, v.104, p.249-266.

Boccaletti, M., Innocenti, F., Manetti, P., Mazzuoli, R., Motamed, A., Pasquare, G., Radicati di Brozolo, F., and Amin Sobhani, E., 1976, Neogene and quaternary volcanism of the Bijar Area (Western Iran): Bulletin of Volcanology, v. 40, p. 122-132.

Chernyshev, I. V., Lebedev, V. A., and Arakelyants, M. M., 2006, K-Ar dating of quaternary volcanics: Methodology and interpretation of results: Petrology, v. 14, no. 1, p. 62-80.

Chiu, H. Y., Chung, S. L., Zarrinkoub, M. H., Mohammadi, S. S., Khatib, M. M., and Iizuka, Y., 2013, Zircon U-Pb age constraints from Iran on the magmatic evolution related to Neotethyan subduction and Zagros orogeny: Lithos, v. 162-163, p. 70-87.

Dabiri, R., Emami, M. H., Mollaei, H., Chen, B., Abedini, M. V., Omran, N. R., and Ghaffari, M., 2011, Quaternary post-collision alkaline volcanism NW of Ahar (NW Iran): geochemical constraints of fractional crystallization process: Geologica Carpathica, v. 62, no. 6, p. 547-562.

Davidson, J., Hassanzadeh, J., Berzins, R., Stockli, D. F., Bashukooh, B., Turrin, B., and Pandamouz, A., 2004, The geology of Damavand volcano, Alborz Mountains, northern Iran: Geological Society Of America Bulletin, v. 116, no. 1-2, p. 16-29.

Djokovic, I., Cvetic, S., and Dimitrijevic, M. D., 1973, Dehaj: Geological Survey of Iran, scale 1:100,000.

Eftekharnezhad, J., 1973, Geological Map of Mahabad: Geological Survey of Iran Press, scale 1:250,000.

Emami, M. H., 1981, Geological Quadrangle map of Iran, 1:250,000 scale, sheet E6 (Qom), Geological Survey of Iran.

Eyuboglu, Y., Santosh, M., Yi, K., Bektas, O., and Kwon, S., 2012, Discovery of Miocene adakitic dacite from the Eastern Pontides Belt (NE Turkey) and a revised geodynamic model for the late Cenozoic evolution of the Eastern Mediterranean region: Lithos, v. 146, p. 218-232.

Guest, B., Horton, B. K., Axen, G. J., Hassanzadeh, J., and McIntosh, W. C., 2007, Middle to late Cenozoic basin evolution in the western Alborz Mountains: Implications for the onset of collisional deformation in northern Iran: Tectonics, v. 26, DOI: 10.1029/2006TC002091.

Hassanzadeh, J., Stockli, D. F., Horton, B. K., Axen, G. J., Stockli, L. D., Grove, M., Schmitt, A. K., and Walker, J. D., 2008, U-Pb zircon geochronology of late Neoproterozoic-Early Cambrian granitoids in Iran: Implications for paleogeography, magmatism, and exhumation history of Iranian basement: Tectonophysics, v. 451, no. 1-4, p. 71-96.

Innocenti, F., Mazzuoli, R., Pasquare, G., Radicatidibrozolo, F., and Villari, L., 1976, Evolution of volcanism in area of interaction between Arabian, Anatolian and Iranian plate (Lake Van, eastern Turkey): Journal of Volcanology and Geothermal Research, v. 1, no. 2, p. 103-112.

Karapetian, S. G., Jrbashian, R. T., and Mnatsakanian, A. K., 2001, Late collision rhyolitic volcanism in the north-eastern part of the Armenian Highland: Journal of Volcanology and Geothermal Research, v. 112, p. 189-220.

Karsli, O., Chen, B., Uysal, I., Aydin, F., Wijbrans, J. R., and Kandemir, R., 2008, Elemental and Sr-Nd-Pb isotopic geochemistry of the most recent Quaternary volcanism in the Erzincan Basin, Eastern Turkey: framework for the evaluation of basalt-lower crust interaction: Lithos, v. 106, no. 1-2, p. 55-70.

Keskin, M., Chugaev, A. V., Lebedev, V. A., Sharkov, E. V., Oyan, V., and Kavak, O., 2012, The geochronology and origin of mantle sources for late cenozoic intraplate volcanism in the frontal part of the Arabian plate in the Karacadag neovolcanic area of Turkey. Part 1. The results of isotope-geochronological studies: Journal of Volcanology and Seismology, v. 6, no. 6, p. 352-360.

Keskin, M., Pearce, J. A., and Mitchell, J. G., 1998, Volcano-stratigraphy and geochemistry of collision-related volcanism on the Erzurum-Kars Plateau, northeastern Turkey: Journal of Volcanology and Geothermal Research, v. 85, p. 355-404.

Kouhestani, H., Ghaderi, M., Zaw, K., Meffre, S., and Emami, M. H., 2012, Geological setting and timing of the Chah Zard breccia-hosted epithermal gold-silver deposit in the Tethyan belt of Iran: Mineralium Deposita, v. 47, no. 4, p. 425-440.

Kurum, S., Onal, A., Boztug, D., Spell, T., and Arslan, M., 2008, (40)Ar/(39)Ar age and geochemistry of the post-collisional Miocene Yamadag volcanics in the Arapkir area (Malatya Province), eastern Anatolia, Turkey: Journal of Asian Earth Sciences, v. 33, no. 3-4, p. 229-251.

Lebedev, V. A., Bubnov, S. N., Chernyshev, I. V., Chugaev, A. V., Dudauri, O. Z., and Vashakidze, G. T., 2007, Geochronology and genesis of subalkaline basaltic lava rivers at the Dzhavakheti highland, Lesser Caucasus: K-Ar and Sr-Nd isotopic data: Geochemistry International, v. 45, no. 3, p. 211-225.

Lebedev, V. A., Bubnov, S. N., Chernyshev, I. V., and Gol'tsman, Y. V., 2006a, Basic magmatism in the geological history of the Elbrus neovolcanic area, Greater Caucasus: Evidence from K-Ar and Sr-Nd isotope data: Doklady Earth Sciences, v. 406, no. 1, p. 37-40.

Lebedev, V. A., Bubnov, S. N., Chernyshev, I. V., Gol'tsman, Y. V., Chugaev, A. V., and Vashakidze, G. T., 2006b, Pliocene granitoid massif in the Kazbek volcanic center: First geochronological and isotope-geochemical data: Doklady Earth Sciences, v. 411, no. 9, p. 1393-1397.

Lebedev, V. A., Bubnov, S. N., Dudauri, O. Z., and Vashakidze, G. T., 2008a, Geochronology of Pliocene volcanism in the Dzhavakheti Highland (the Lesser Caucasus). Part 1: Western part of the Dzhavakheti Highland: Stratigraphy and Geological Correlation, v. 16, no. 2, p. 204-224.

-, 2008b, Geochronology of Pliocene volcanism in the Dzhavakheti Highland (the Lesser Caucasus). Part 2: Eastern part of the Dzhavakheti Highland. Regional geological correlation: Stratigraphy and Geological Correlation, v. 16, no. 5, p. 553-574.

Lebedev, V. A., Chernyshev, I. V., Dudauri, O. Z., Vashakidze, G. T., Goltsman, Y. V., Bairova, E. D., and Yakushev, A. I., 2013, Manifestations of Miocene acid intrusive magmatism on the southern slope of the Greater Caucasus: First evidence from isotope geochronology: Doklady Earth Sciences, v. 450, no. 1, p. 550-555.

Lebedev, V. A., Chernyshev, I. V., and Sharkov, E. V., 2011, Geochronological scale and evolution of late Cenozoic magmatism within the Caucasian segment of the alpine belt: Doklady Earth Sciences, v. 441, no. 2, p. 1656-1660.

Lebedev, V. A., Chernyshev, I. V., Vashakidze, G. T., Gudina, M. V., and Yakushev, A. I., 2012, Geochronology of miocene volcanism in the northern part of the Lesser Caucasus (Erusheti Highland, Georgia): Doklady Earth Sciences, v. 444, no. 1, p. 585-590.

Lebedev, V. A., Sakhno, V. G., and Yakushev, A. I., 2009, Late Cenozoic volcanic activity in western Georgia: Evidence from new isotope geochronological data: Doklady Earth Sciences, v. 427, no. 1, p. 819-825.

McInnes, B. I. A., and Evans, N. J., 2005, Application of thermochronology to hydrothermal ore deposits: Low-Temperature Thermochronology: Techniques, Interpretations, and Applications, v. 58, p. 467-498.

Milton, D. J., 1977, Qal'eh Hasan Ali Maars, central Iran: Bulletin of Volcanology, v. 40, p. 201–208.

Mitchell, J., and Westaway, R., 1999, Chronology of Neogene and Quaternary uplift and magmatism in the Caucasus: constraints from K-Ar dating of volcanism in Armenia: Tectonophysics, v. 304, no. 3, p. 157-186.

Pang, K. N., Chung, S. L., Zarrinkoub, M. H., Lin, Y. C., Lee, H. Y., Lo, C. H., and Khatib, M. M., 2013, Iranian ultrapotassic volcanism at ~11 Ma signifies the initiation of post-collisional magmatism in the Arabia–Eurasia collision zone: Terra Nova, v. 25, p. 405-413.

Pang, K. N., Chung, S. L., Zarrinkoub, M. H., Mohammadi, S. S., Yang, H. M., Chu, C. H., Lee, H. Y., and Lo, C. H., 2012, Age, geochemical characteristics and petrogenesis of Late Cenozoic intraplate alkali basalts in the Lut-Sistan region, eastern Iran: Chemical Geology, v. 306, p. 40-53.

Parlak, O., Delaloye, M., Demirkol, C., and Unlugenc, U. C., 2001, Geochemistry of Pliocene/Pleistocene basalts along the Central Anatolian Fault Zone (CAFZ), Turkey: Geodinamica Acta, v. 14, no. 1-3, p. 159-167.

Pearce, J. A., Bender, J. F., Delong, S. E., Kidd, W. S. F., Low, P. J., Guner, Y., Sargolu, F., Yilmaz, Y., Moorbath, S., and Mitchell, J. G., 1990, Genesis of collision volcanism in eastern Anatolia, Turkey: Journal of Volcanology and Geothermal Research, v. 44, p. 189-229.

Richards, J. P., Spell, T., Rameh, E., Razique, A., and Fletcher, T., 2012, High Sr/Y Magmas Reflect Arc Maturity, High Magmatic Water Content, and Porphyry Cu +/- Mo +/- Au Potential: Examples from the Tethyan Arcs of Central and Eastern Iran and Western Pakistan: Economic Geology, v. 107, no. 2, p. 295-332.

Richards, J. P., Wilkinson, D., and Ullrich, T., 2006, Geology of the Sari Gunay epithermal gold deposit, northwest Iran: Economic Geology, v. 101, no. 8, p. 1455-1496.

Saadat, S., and Stern, C. R., 2011, Petrochemistry and genesis of olivine basalts from small monogenetic parasitic cones of Bazman stratovolcano, Makran arc, southeastern Iran: Lithos, v. 125, p. 607-619.

Saadat, S., and Stern, C. R., 2012, Petrochemistry of a xenolith-bearing Neogene alkali olivine basalt from northeastern Iran: Journal of Volcanology and Geothermal Research, v. 225, p. 13-29.

Shabanian, E., Bellier, O., Siame, L., Arnaud, N., Abbassi, M. R., and Cocheme, J. J., 2009, New tectonic configuration in NE Iran: Active strike-slip faulting between the Kopeh Dagh and Binalud mountains: Tectonics, v. 28, TC5002, doi: 10.1029/2008TC002444.

Temizel, I., Arslan, M., Ruffet, G., and Peucat, J. J., 2012, Petrochemistry, geochronology and Sr-Nd isotopic systematics of the Tertiary collisional and post-collisional volcanic rocks from the Ulubey (Ordu) area, eastern Pontide, NE Turkey: Implications for extension-related origin and mantle source characteristics: Lithos, v. 128, p. 126-147.

Walker, R. T., Gans, P., Allen, M. B., Jackson, J., Khatib, M., Marsh, N., and Zarrinkoub, M., 2009, Late Cenozoic volcanism and rates of active faulting in eastern Iran: Geophyical Journal International, v. 177, p. 783-805.

Zahedi, M., and Hajian, J., 1985, Sanandaj: Geological Survey of Iran, scale 1:250,000.

Chapter 4

Dynamics of lithospheric thinning and mantle melting by edge-driven convection: Application to Moroccan Atlas mountains[1]

4.1 Introduction

Edge-driven convection (EDC) is a term coined for convection patterns forming at locations of significant lithosphere thickness gradients, e.g. craton edges. First described as a craton edge flow instability by Elder (1976) in his laboratory experiments, EDC has since been studied by numerical experiments (e.g. King and Anderson, 1995; King and Anderson, 1998). Two styles of EDC can be distinguished, termed here as EDC *sensu stricto* (EDC s.s.) and EDC with shear (EDC w.s.). EDC s.s. is dominated by cold downward flow caused by the relatively cold sloping boundary (the edge) of the thicker lithosphere cooling the sub-lithospheric mantle next to it (Fig 4.1a). EDC w.s. is caused by horizontal flow from below the thicker lithosphere to the direction of the thinner lithosphere, as a consequence of a long wavelength horizontal temperature difference between the mantle underneath the thicker lithosphere and the thinner lithosphere. The shear caused by this large scale flow induces a small secondary convection cell in the corner between the thicker and thinner lithospheres (Fig 4.1b).

The upward flow, inherently present in both styles of EDC, is a potential cause for decompression mantle melting and dynamic topography effects. Consequently, EDC has been proposed in many locations where there is a clear lithosphere gradient present. For example, EDC has been suggested

[1]This chapter has been previously published as Kaislaniemi L. and van Hunen J. (2014). *Dynamics of lithospheric thinning and mantle melting by edge-driven convection: Application to Moroccan Atlas mountains*. Geochemistry, Geophysics, Geosystems, 15. DOI:10.1002/2014GC005414. The numerical experiments were conducted and the manuscript produced by L. Kaislaniemi. J. van Hunen has participated in the study by providing training, feedback, and useful discussions.

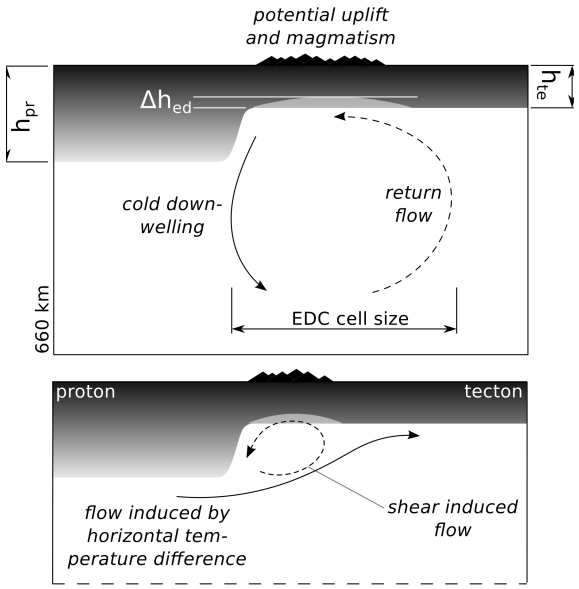

Figure 4.1: Two styles of edge-driven convection. a) EDC *sensu stricto*, where the boundary of the cold thick lithosphere on the left (the proton or archon) cools down the asthenosphere next to it. This leads to downwellings at the edge and a return flow further away underneath the thinner lithosphere (or tecton) on the right. b) EDC with shear, where the higher than horizontal average temperature below the proton leads to horizontal mantle flow to underneath the tecton, and causes a small convection cell to form next to the edge.

to be the cause for the African and South American intraplate volcanism (King and Ritsema, 2000), the high topography and volcanism surrounding the Colorado plateau in southwestern United States (van Wijk et al., 2010), the seismic structure of the mantle and increased heat flow in the Canadian Cordillera (Hardebol et al., 2012), and the alternating low-high-low topography of the Bermuda Rise in the western Atlantic (Shahnas, 2004). Generally, EDC can be expected to be present where two lithospheric domains of different thicknesses meet. These thicknesses often reflect the different tectonothermal ages of the lithospheric terranes, and, for convenience, we shall refer to these domains as *protons* and *tectons* (Griffin et al., 2003; Janse, 1994), where proton refers to the thicker, more viscous, lithosphere being older than Neoproterozoic in age, and tecton refers to the thinner lithosphere.

The inherent differences between the two styles of EDC (Fig 4.1) have been given little attention, and many studies either assume EDC s.s. or do not explicitly mention which style of EDC they have intended to study. As noted by King and Anderson (1998), EDC s.s. is very sensitive to long wavelength mantle temperature perturbations and there seems to be a continuum from EDC s.s. to EDC w.s.: if the temperature difference between sub-lithospheric mantles of the proton and tecton exceeds 0.1 to 1 %, the EDC s.s. is overruled by the large scale flow and can even switch to EDC w.s. The difference in sub-lithospheric mantle temperatures could be caused by large-scale mantle flow patterns (e.g. mantle plumes), and can also be triggered by the thermal insulating effect of the thick lithosphere above (e.g. Gurnis, 1988).

Additionally, EDC s.s. is sensitive to relative velocity of the lithosphere and the asthenosphere. Plate movements, relative to the asthenosphere below, exceeding 1 cm/yr can suppress the EDC s.s. (King and Anderson, 1998), and, depending on the direction of the plate movement relative to the thickness gradient, cause convection similar to EDC w.s., also referred to as shear-driven upwelling (Conrad et al., 2010).

The convection cell caused by EDC s.s. dominates a large portion of the upper mantle height (∼300-500 km diameter) (e.g. van Wijk et al., 2010; King and Ritsema, 2000). Much smaller

convection cell sizes are observed in the case of EDC w.s., usually in the order of 150-200 km, as shown by King and Anderson (1998). In this respect, EDC s.s. is a viable mechanism to explain observations spanning many hundreds of kilometers in horizontal direction, e.g. the aforementioned high topography of the Western Atlantic, spanning over 1000 kilometers in width (Shahnas, 2004). However, due to its large convection cell size, EDC s.s. (in the sense of King and Anderson (1995)) is hardly able to produce very local effects, such as those observed in NW African Atlas mountains in Morocco: Here, intraplate orogeny close to the West African craton edge is associated with Cenozoic volcanism and localized strong thinning of the lithosphere along the craton edge. Missenard and Cadoux (2012) were first to suggest the existence of EDC under the Atlas mountains. Due to strong lithospheric thickness gradient in this area, it is an ideal location for an EDC to take place. As the thinned, narrow lithospheric corridor is very close to the craton edge, it is more probably caused by the EDC w.s. rather than EDC s.s.

We have studied the features of combined EDC w.s. and EDC s.s. using numerical models and applied those to the Moroccan Atlas mountains to test the hypothesis of EDC in this area.

4.1.1 Cenozoic volcanism in the Moroccan Atlas mountains

The Moroccan Atlas mountains (High and Middle Atlas) are an intraplate orogeny, uplifted in the Cenozoic by combination of lithospheric thinning and crustal shortening (Missenard et al., 2006). They are formed as tectonically inverted basins, deformed along the inherited zones of weaknesses that were created during the opening of the Atlantic ocean in the late Triassic to early Jurassic (Frizon de Lamotte et al., 2000, and references therein). The amount of shortening in Atlas mountains is modest (15-30 % for the High Atlas and 10 % for the Middle Atlas, Beauchamp et al. (1999), Teixell et al. (2003), Gomez et al. (1998), and Teixell et al. (2009)) and it has been suggested that lithospheric thinning is responsible for one third of the elevation in western high Atlas, most of the elevation in Anti-Atlas, and about half of the elevation in the central High Atlas and middle Atlas (Missenard et al. (2006), see also Miller and Becker (2014)). To the south and southeast of the Atlas mountain chain lies the West African Craton and Saharan platform (Piqué et al., 2002).

The Atlas mountains region has experienced widespread volcanism in the Cenozoic (Fig 4.2). The volcanism can be roughly divided into two phases (Missenard and Cadoux, 2012): the first pulse of volcanism started in the beginning of the Cenozoic and the second, more voluminous phase, at about 11 Ma in the Miocene. These were separated by about a 20 Myrs gap in which no volcanic activity took place. The volcanism shows an alkaline intraplate chemical affinity (Mokhtari and Velde, 1988; Rachdi et al., 1997; El Azzouzi et al., 2010; El Azzouzi et al., 1999; Wagner et al., 2003), except for the three provinces in the North, closest to the Mediterranean Sea (Fig 4.2), which are calc-alkaline to alkaline and related also to the Rif subduction system (Coulon et al., 2002; Maury et al., 2000).

An anomalously thin lithosphere exists beneath the Atlas mountains as a semi-continuous zone from the Atlantic margin to the Africa-Eurasia plate boundary in the northeast, named the "Moroccan Hot Line" (Frizon de Lamotte et al., 2000) and situated beneath most of the Cenozoic volcanic provinces of the region. The width of this zone varies from 200 to 500 km and the lithosphere

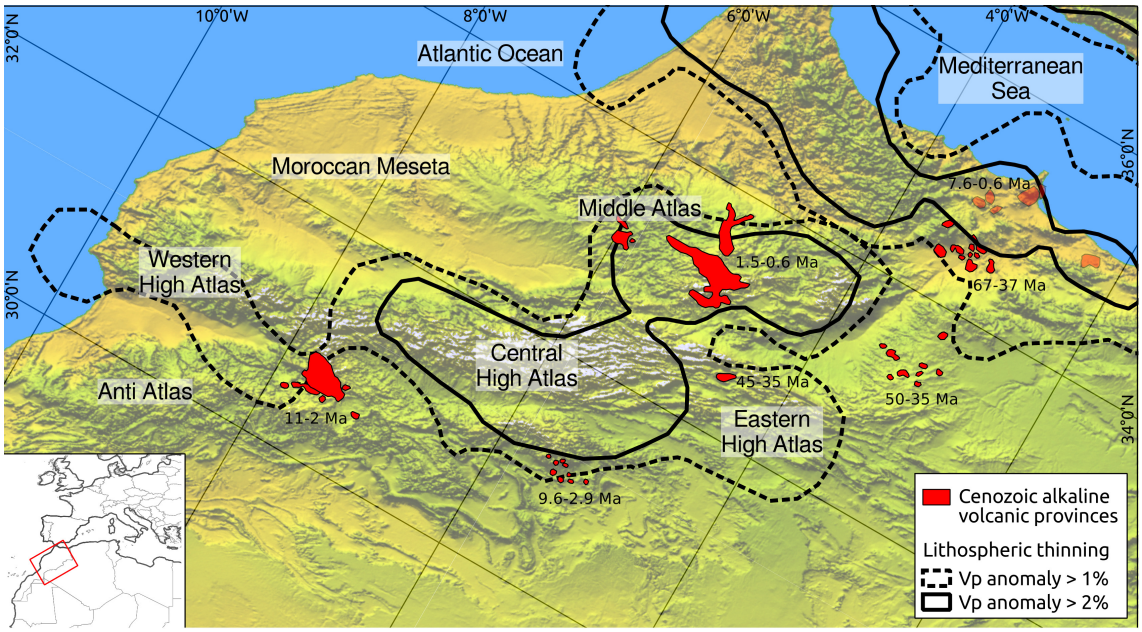

Figure 4.2: The topography of the Moroccan Atlas mountains (background map, NASA Shuttle Radar Topography Mission, Farr et al., 2007) overlaid by the Cenozoic alkaline volcanic provinces (in red, from Missenard and Cadoux, 2012). The three volcanic provinces in the North (transparent colour) have transitional calc-alkaline to alkaline chemical affinity and are partly related to the Rif subduction system. Black contour lines delineate the area of thinned lithosphere, where Vp velocities at 50 km depth are slower by 1 % (dashed line) or 2 % (solid line) (from Bezada et al., 2014).

thickness is 60 to 90 km according to geopotential field studies (Fullea et al., 2010; Missenard et al., 2006). Seismic studies also show thin lithosphere in this area with high Sn attenuation and low Pn velocities, some suggesting lithosphere-asthenosphere boundaries as shallow as 50 km (Palomeras et al., 2014; Seber et al., 1996; Calvert et al., 2000). S/SKS splitting shows localized asthenospheric flow in the Middle Atlas and Central High Atlas parallel to the trend of the mountain chains (Miller et al., 2013). The thinning has been attributed to delamination of the Atlas mountain root (Duggen, 2005; Bezada et al., 2014; Ramdani, 1998) and edge-driven convection (Missenard and Cadoux, 2012). The observation that the Cenozoic volcanism of the region is similar in composition to the plume derived volcanism at the Canary Islands (Duggen et al., 2009) has led to the proposition that the thinned zone acts as a corridor for the hot plume material, causing the volcanism in the Atlas region.

4.2 Methods

To model the EDC we solve the non-dimensional equations of conservation of mass, momentum, and energy using finite element mantle convection code Citcom (Moresi and Gurnis, 1996; Zhong et al., 2000). The effects of shear heating, adiabatic heating, and latent heat of melting are accounted for via the extended Boussinesq approximation (Christensen and Yuen, 1985). The models consist of 3960 km (x 3960 km) x 660 km domain (x-z in 2D and x-y-z in 3D case) representing upper mantle and crust. An area of high lithosphere thickness is imposed with an artificially high (100 times

larger) viscosity block on the left of the model domain, from $x = 0\,\text{km}$ to $x = 990\,\text{km}$, extending to depth of $z = 200\,\text{km}$, representing the more viscous cratonic lithosphere, the proton. The tecton with thin lithosphere has normal mantle viscosity. The initial thermal structure (thickness) of the lithosphere is the steady state thickness, attained after prolonged model run time prior to examination of EDC related processes (see also discussion in 4.4.2). The steady state is defined to be reached when the average lithosphere thickness grows by less than 0.1% in one million years. This test for steady state is performed on each of the models separately so that each model with different parameters has its own initial temperature field consistent with the imposed parameters.

Parameter	Symbol & units	Value(s) used
Water content	$X_{\text{H}_2\text{O}}$, ppm wt	100, 200, 300, 400
Activation energy	E, kJ mol^{-1},	120, 150, 180, 210, 240, 270
Radiogenic heating	Q, $10^{-12} \times \text{W kg}^{-1}$	12, 19, 27
Activation volume	V, $\text{m}^3\,\text{mol}^{-1}$	6×10^{-6}
Reference temperature	$T_{\text{abs},0}$, K	1623
Reference pressure	P_0, Pa	21.4×10^9 (660 km depth)
Reference viscosity	η_0, Pa s	10^{24}
Reference density	ρ_0, kg m^{-3}	3300
Thermal diffusivity	κ, $\text{m}^2\,\text{s}^{-1}$	10^{-6}
Latent heat of melting	L, kJ kg^{-1}	560
Coefficient of thermal expansion	α, K^{-1}	3.5×10^{-5}

Table 4.1: Model input parameters used.

We have imposed closed free-slip stress boundary conditions at each boundary and zero heat flow at each boundary except for the surface for which $T = 0°\text{C}$. To maintain a stable realistic mantle potential temperature without additional heating from the bottom boundary, we have increased the radiogenic heating values of the mantle (Table 4.1) to between 1.5 and 3.7 times higher than the modern-day mantle values ($7.38 \times 10^{-12}\,\text{W kg}^{-1}$ (Schubert et al., 2001)). The advantage of using internal heating to maintain the model temperature instead of bottom heating is that the rate of thermal plume generation at the transition zone is greatly diminished. This helps in identifying the thermal anomalies at lithosphere-asthenosphere boundary caused by EDC alone. The higher values of radiogenic heating can also be used to reflect the style of EDC in the early Earth. The lack of bottom heating means that the background convection of the Earth's mantle is slightly underestimated in the models, and the convection produced by the EDC is not being as easily disturbed, i.e. that the convection patterns produced by the EDC can live for indefinitely long times in the models, whereas in reality they would most probably be destroyed at some point by other large-scale convection patterns of the mantle.

We have incorporated the hydrous peridotite melting parameterization of (Katz et al., 2003) to study the amounts of melts produced by the EDC. The compositional fields (water content and depletion) are advected using a marker-in-cell method (e.g. Gerya and Yuen, 2003) with a second order Runge-Kutta scheme. The amount of melting in each marker is calculated each time step, and any melt produced is removed assuming instantaneous percolation to the surface. The amount of water removed with the melts is calculated assuming batch melting and water incompatibility with bulk partition coefficient of $D = 0.01$. After melting, the depletion value $F_{\%} = 100F$ of

each marker is adjusted. The depletion affects the buoyancy of the mantle using the following parameterization:

$$\frac{\mathrm{d}\ln\rho}{\mathrm{d}F_{\%}} = -0.00020 \tag{4.1}$$

from (Schutt and Lesher, 2006), which is applicable at pressures of about 3 GPa.

Linear, temperature and pressure dependent viscosity parameterization for olivine rheology (Karato and Wu, 1993) is applied:

$$\eta_{\mathrm{dry}} = \eta_0 \exp\left(\frac{E+PV}{RT_{\mathrm{abs}}}\right) \exp\left(-\frac{E+P_0V}{RT_{\mathrm{abs},0}}\right), \tag{4.2}$$

where E and V are the activation energy and volume, respectively, R is the gas constant, T_{abs} is the absolute temperature, and P the pressure (see Table 4.1 for values.) $T_{\mathrm{abs},0}$ and P_0 are the reference temperature and pressure in which conditions the viscosity has the reference value η_0. Because adiabatic heating has been used, there is no single location in the model domain where $T = T_0$ and $P = P_0$, and thus η_0 does not represent mantle viscosity directly at any particular location.

Reduced values for activation energy E have been used to 'mimic' the behaviour of non-linear rheology at the shallow level of the mantle, the lithosphere-asthenosphere boundary. This circumvents the added complexity of finding suitable rheology parameters for a long-term steady state model in a non-linear viscosity case. The initial conditions for non-linear rheology models of small-scale convection are even more critical than those of linear rheology models (Sleep, 2007). As shown by Christensen (1984), multiplying the activation enthalpy ($H = E + PV$) value of the Newtonian rheology formulation by a factor of $\beta < 1$ produces similar steady state convection patterns than a non-linear rheology with normal activation enthalpy. The exact value of β depends on the ratio of E and V. In a temperature dominated rheology (high E/V), such as ours, Christensen (1984) suggests that $\beta = 0.3 \ldots 0.5$ would be a suitable value. Furthermore, van Hunen et al. (2005) have shown that lowering the activation energy from $360\,\mathrm{kJ\,mol^{-1}}$ to $120\,\mathrm{kJ\,mol^{-1}}$ in a Newtonian rheology increases the thermomechanical erosion of the lithosphere and causes thermal boundary layer instability similar to non-Newtonian ($n = 3.5$, $E = 540\,\mathrm{kJ\,mol^{-1}}$) rheology. In our parameter study we have used low values for the activation energy but varied them to study the effect of rheology on EDC dynamics (Table 4.1).

To account for the viscosity lowering effect of water, we use a water weakening parameterization

$$\eta_{\mathrm{hydrous}} = W\eta_{\mathrm{dry}},\ W = 100^{\frac{-X_{\mathrm{H_2O}}}{X_{\mathrm{H_2O}}+a}}, \tag{4.3}$$

as used by Kaislaniemi et al. (2014, Chapter 3). $X_{\mathrm{H_2O}}$ is the water content (wt ppm), and a (wt ppm) is a parameter controlling the sensitivity of water weakening (i.e. how large $X_{\mathrm{H_2O}}$ needs to be to decrease viscosity by one order of magnitude). This parameterization conforms to the boundary conditions set by experimental results (Kohlstedt et al., 1995; Hirth and Kohlstedt, 1996; Mei and Kohlstedt, 2000; Bai and Kohlstedt, 1992): viscosity is inversely proportional to the water fugacity, and, at low water contents, water fugacity is proportional to the water content. I.e., $\eta \propto C_{\mathrm{OH}}^{-r}$, where C_{OH} is the water (hydroxyl ion) concentration in olivine, and r is a constant close to one. Also,

there should be a maximum limit for the weakening. Karato (2010) reports maximum viscosity weakening by water of four orders of magnitude, whereas Fei et al. (2013) reports maximum weakening by less than one order of magnitude. We use a commonly used value from Hirth and Kohlstedt (1996) who report maximum weakening of about two orders of magnitude. Our parameterization asymptotically approaches this value as water content increases. The water weakening parameterization used here has an additional advantage that it allows the water content to approach zero during melt removal, while still producing finite viscosity estimations values.

The lower end of the used water content values represent asthenospheric background concentrations, i.e. those present in mid-oceanic ridge basalt source mantle (∼120 wt ppm, Dixon et al., 2004). High water content values are used to test the effect of mantle hydration on edge-driven convection in scenarios where the edge is situated near to a source of water, e.g. a recent subduction zone.

The amount of melting (volcanism) is calculated by assuming that all melt percolates instantly to the surface. The amount of uplift is estimated by calculating the corresponding layer thickness (with $\rho = 2800\,\mathrm{kg\,m^3}$) needed to compensate the vertical stress at the upper boundary of the model.

4.3 Results

4.3.1 General convection patterns of the EDC

An edge-driven convection pattern forms at the transition from the thin tecton lithosphere to the thicker proton lithosphere (Fig 4.3). The style of the convection periodically changes from what looks like EDC s.s. (Fig 4.3a), but with a smaller convection cell size, to purely EDC w.s. style convection (Fig 4.3b) where the horizontal flow completely overrules the downwelling cold flow. This competition between horizontal flow and the cold downwelling produces periodic behaviour in the flow. The horizontal flow is initially caused by the insulating effect of the thicker proton lithosphere, which keeps the mantle below the proton warmer than elsewhere. Once the horizontal flow is formed it causes a large-scale convection cell and a return flow to below the proton in the lower part of the upper mantle, which maintains the flow induced by continental insulation.

In the EDC convection cell the upwelling mantle material erodes the bottom of the lithosphere. Upwellings also make decompression melting possible. Where any melts are removed, a layer of depleted material (in black in Fig 4.3) is left behind. This drier (more viscous) and depleted (more buoyant) material tends to stick to the bottom of the lithosphere, from where it and pieces of lithosphere are later being partly delaminated by the erosional effect of the EDC convection cell (Fig 4.4).

4.3.2 Parameter study results

The chosen model input parameters (Table 4.1) result in models with a range of different mantle potential temperatures (1290−1472°C) and different average (statistically steady state) lithospheric

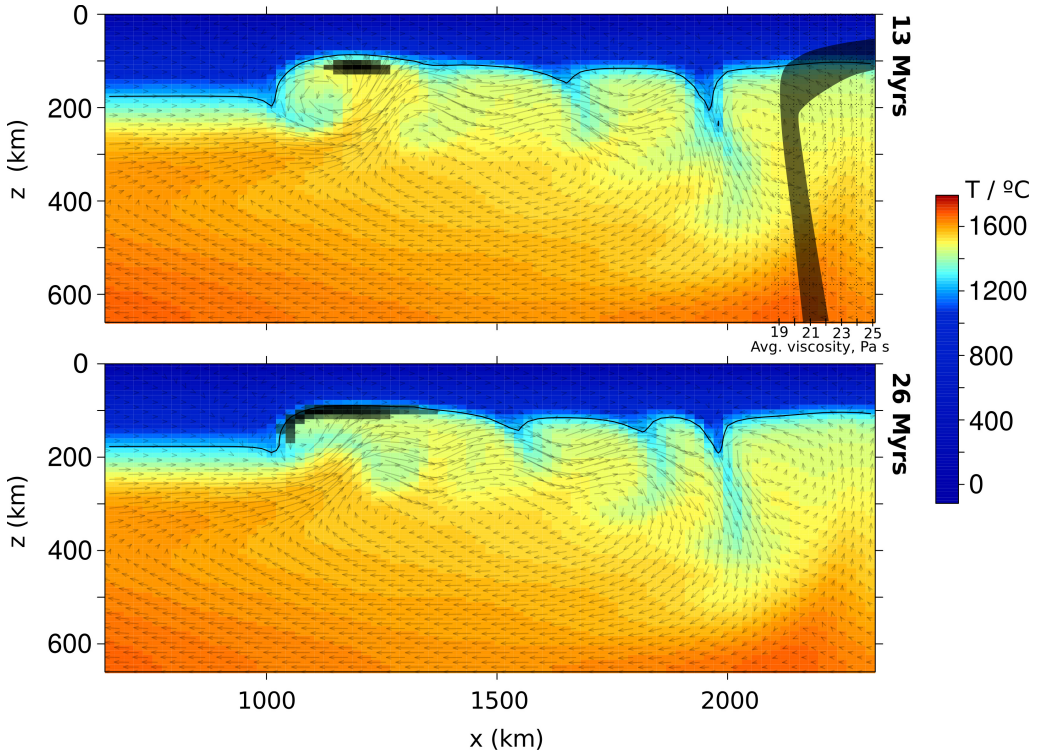

Figure 4.3: Two end-members of the EDC: downwelling dominated (above, similar to EDC s.s.) and upwelling dominated (below, EDC with shear), occurring in same model but separated by about 13 Myrs. Regions of melting depleted mantle in black. The shaded profile on the right in the upper figure shows the range of horizontal average viscosity values of the tecton domain in all of the 2D models.

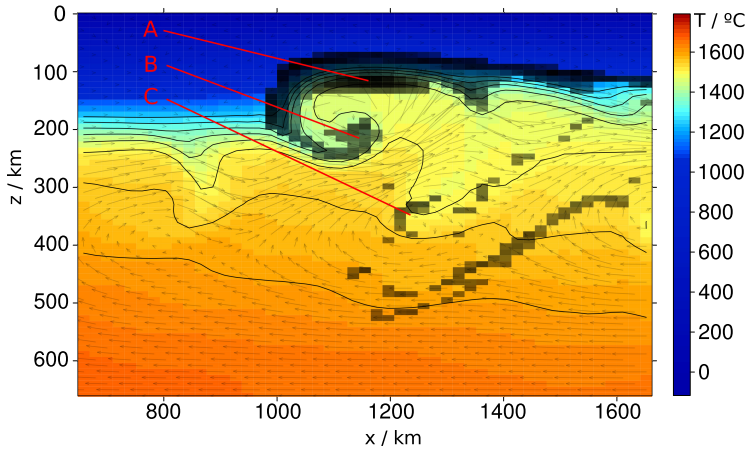

Figure 4.4: Temperature and depletion field in detail near the edge. Depleted material (in black) forms after decompression melting at the upper part of the EDC convection cell ("A"). It then sticks to the bottom of the lithosphere where it is being dragged horizontally by the asthenospheric flow. The shear caused by the EDC convection cell delaminates pieces of lithosphere together with depleted material ("B"). Relatively cold delaminated pieces with depleted material in them can sink deep into the mantle ("C") before being mechanically mixed with rest of the mantle by the background mantle flow. For comparison to tomography results, see Discussion, 4.4.1.

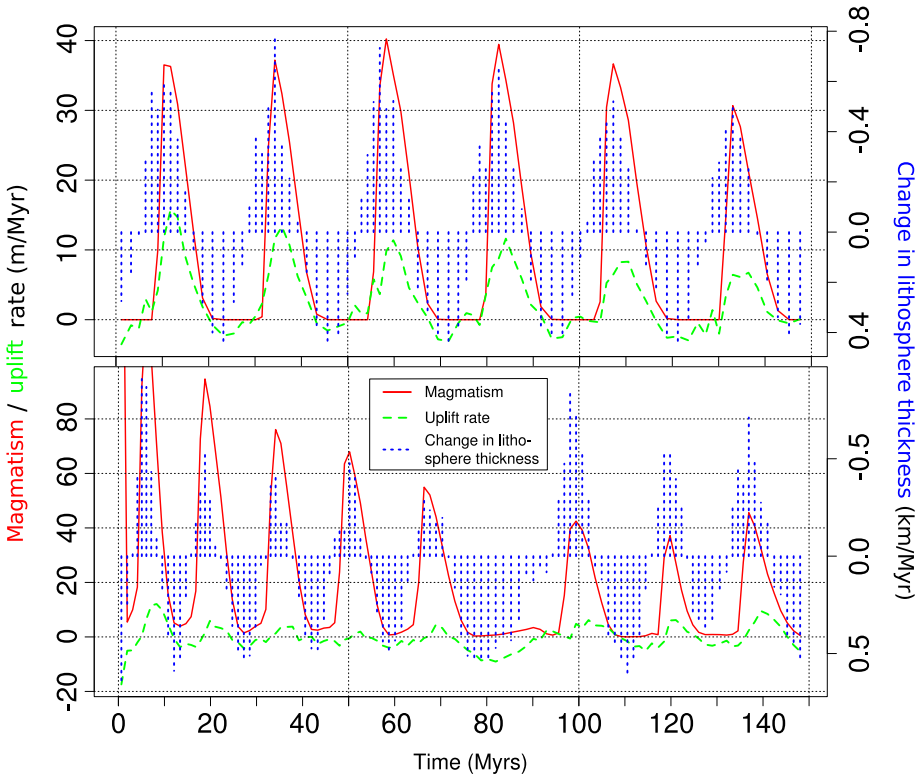

Figure 4.5: The history of uplift and magmatism in two of the models, discussed in relation to the Moroccan Atlas mountains (Section 4.4.1). Values are measured at the location of maximum lithospheric thinning (Δh_{ed}) near the edge. Models not plotted here show varying amounts of correlation between these periods (see Fig 4.6b), but all show that the change in the lithosphere thickness systematically precedes the maximum of the magmatism. The models shown here are marked with circles in all panels in Fig 4.6. Models have following parameters: a) $X_{\mathrm{H_2O}} = 200\,\mathrm{ppm}, Q = 19 \times 10^{-12}\mathrm{W\,kg^{-1}}, E = 120\,\mathrm{kJ\,mol^{-1}}$, b) same as (a) but with $X_{\mathrm{H_2O}} = 400\,\mathrm{ppm}$. Resulting temperatures are: a) $T_{\mathrm{pot}} = 1388°\mathrm{C}$, $\Delta T_{\mathrm{pot,pr/te}} = 41°\mathrm{C}$, b) $T_{\mathrm{pot}} = 1358°\mathrm{C}$, $\Delta T_{\mathrm{pot,pr/te}} = 25°\mathrm{C}$.

thicknesses (1250°C isotherm at $h_{\mathrm{te}} = 96 - 184\,\mathrm{km}$ and $h_{\mathrm{pr}} = 158 - 206\,\mathrm{km}$ for tecton and proton lithospheres, respectively). The EDC convection pattern is present in all of the models. The horizontal potential temperature differences between the sub-lithospheric mantles of the tecton and the proton, $\Delta T_{\mathrm{pr/te}}$, range between $8 - 61°\mathrm{C}$. The amount of lithospheric thinning, Δh_{ed} (see Fig 4.1a), which is the difference between the tecton lithosphere thickness (h_{te}) and the thickness (h_{ed}) at the thinnest part of lithosphere next to the proton-tecton edge, ranges between $11 - 51\,\mathrm{km}$. The horizontal width of this thinned region is about 200 km.

Models show very clear pulsating nature in the EDC. This is evident as periodic uplift, lithospheric thinning/thickening, and magmatism at the edge (Fig 4.5), and from the convection patterns (Fig 4.3).

The periodicity of the melting varies between 14 and 26 Myrs among the models and is negatively correlated with the root mean square velocity of the model domain (Fig 4.6b). The periodicity of the lithosphere erosion has a larger variability among the models, but show similar trends to the melting periodicity, and often even equal periods as well. A correlation between the root mean square velocity and the model average mantle potential temperature and water contents can be

found empirically (Fig 4.6d). Thus, the periods of uplift rate and melting (Fig 4.6b) negatively correlate with mantle potential temperature and water contents.

The amount of lithospheric thinning above the EDC convection cell is related to the activation energy of the viscosity parameterization (Fig 4.6a) and lithosphere thickness difference across the edge (Fig 4.6c). However, once melts are produced in the upper part of the EDC convection cell, the more viscous, slightly buoyant and colder depleted material gathers in the eroded lithosphere pocket (see Fig 4.3) and re-thickens the lithosphere (i.e. reduces Δh_{ed}), as is evident from Fig 4.6a for models where magmatism $> 0\,\mathrm{m\,Myr^{-1}}$.

The effect of lithosphere thickness difference across the edge on the amount of lithospheric thinning at the edge is clearest with relatively cold models (Fig 4.6c). Models with high potential temperature (and thus also with lowest viscosities) show little variation in the amount of thinning and the thinning in these models is generally minor. However, because of high temperatures, not so much thinning is required to allow the asthenospheric flow cross the solidus and melt. The three separate groups are formed by different internal heating values, and the negative trends within these groups are formed by the variation of the activation energy E (lowest values producing thinnest tecton thicknesses).

The amount of melt produced by EDC is mainly a function of the tecton lithosphere thickness. This tecton lithosphere thickness, on the other hand, depends on the effective average viscosity of the mantle, or, in other words, mantle potential temperature, mantle water contents, and mantle's rheological activation energy. A negative correlation is found between amount of lithosphere thinning by EDC (Δh_{ed}) and amount of melt produced (Fig 4.6a). This counter-intuitive relationship is caused by two factors: 1) models with thin average tecton lithosphere cannot produce much more thinning via EDC as the thinning is even more effectively balanced by conductive cooling of the lithosphere; 2) melting consumes heat, cooling down the mantle, and produces high viscosity, slightly lower temperature depleted layer in the thinned lithosphere pocket, increasing the apparent thickness of the lithosphere (cf. Fig 4.6a). Amounts of melt produced (if produced at all) vary between zero and 60 $\mathrm{m\,Myr^{-1}}$ (average over 150 Myrs model time) for lithosphere average thinning amounts of about 40 to 20 km, respectively. If restricted to models with reasonable potential temperatures for today's Earth (1300 to 1400 deg C), amounts of melting and lithosphere thinning vary much less (5 to 20 $\mathrm{m\,Myr^{-1}}$, 30 to 36 km, respectively).

4.3.3 Three-dimensional structure of EDC

Results from a 3D model show the presence of the EDC but in addition indicates that the flow produced by the horizontal sub-lithospheric temperature difference produces convection rolls under the thinner tecton lithosphere with their axes perpendicular to the edge of the two lithospheric domains (Fig 4.7). In these rolls there is upflow on one side and downflow on the other side, while the overall flow is dominated by the horizontal sub-lithospheric flow. The horizontal flow is oriented away from the thicker proton lithosphere as in the 2D case, but there is also, especially near the edge, a significant horizontal velocity component parallel to the proton edge. This velocity component forms the upper part of the convection rolls or tubes that shape the lithosphere bottom. The existence of these rolls also affects the properties of the EDC along the edge. EDC is present

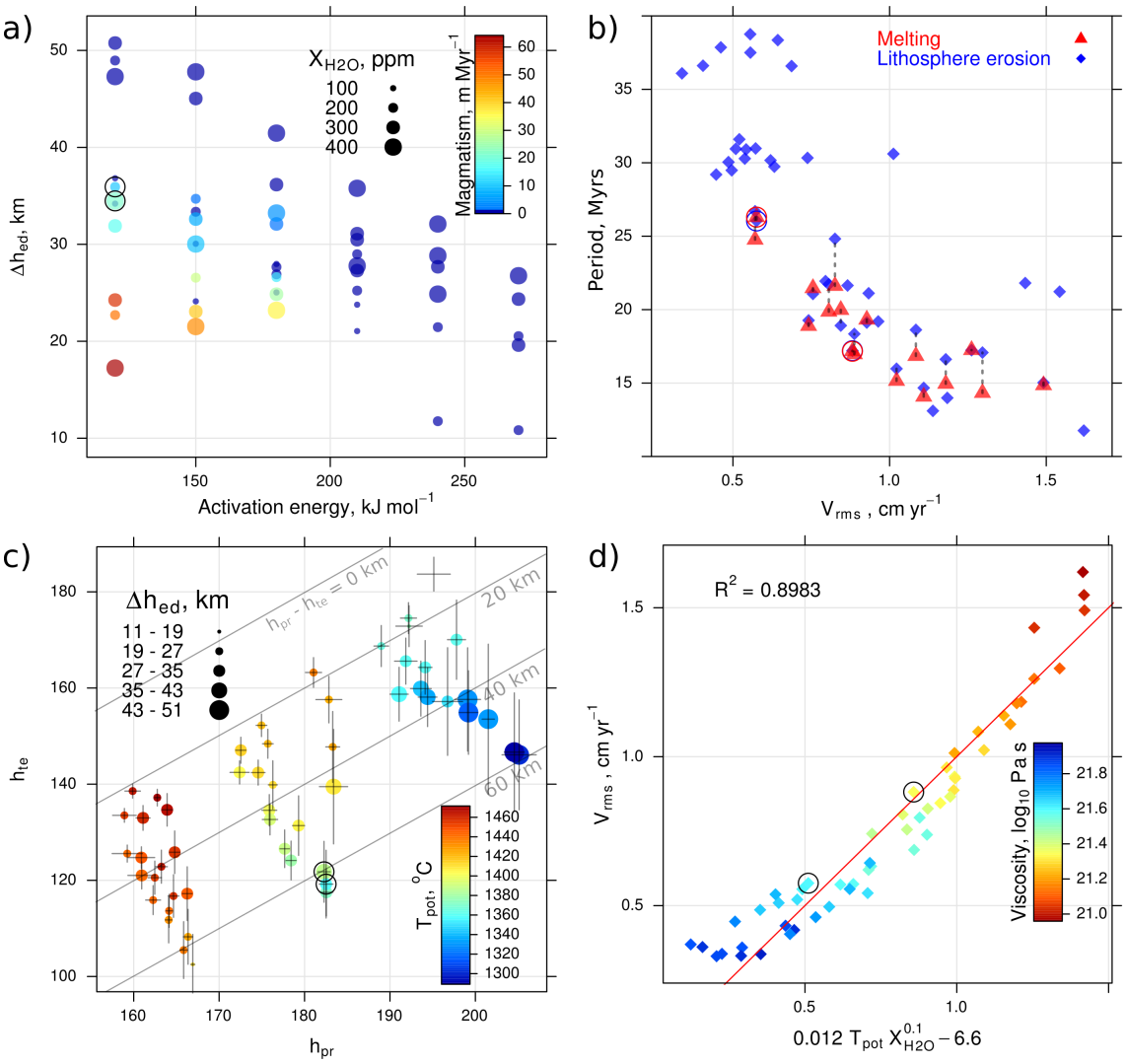

Figure 4.6: Parameter study results from the 2D models. *(a)* The negative correlation between the activation energy value in the viscosity parameterization and the produced lithosphere thinning near the edge. Models where melts are produced start to deviate from the linear relationship as the melt residue at the top of the EDC convection cell decreases the thermal lithosphere thickness. Models with low water contents produce generally less thinning. *(b)* Relationship between the model root mean square velocity and the period of melting events or lithosphere thickness variation near the edge. Dashed lines connect models with same set of input parameters. Note that the melting period has been only plotted for models where melts are produced. There are eight models in which lithospheric erosion period is either non-existent or too long to be determined within the 150 Myrs model run time. *(c)* Amount of lithosphere thinning near the edge as a function of proton and tecton lithosphere thicknesses and average mantle potential temperature. Error bars show the variation (standard deviation) in the lithosphere thicknesses. Isolines of lithosphere thickness difference (proton-tecton) has been plotted in the background. *(d)* Model data points and best empirical fit of model root mean square velocity as a function of mantle potential temperature and water content. The linear relationship is good and indicates that horizontal axis in (b) could be expressed also in terms of potential temperature and water content. *(a-d)* Circled models are those shown in Fig 4.5 and discussed in Discussion in relation to the Moroccan Atlas mountains.

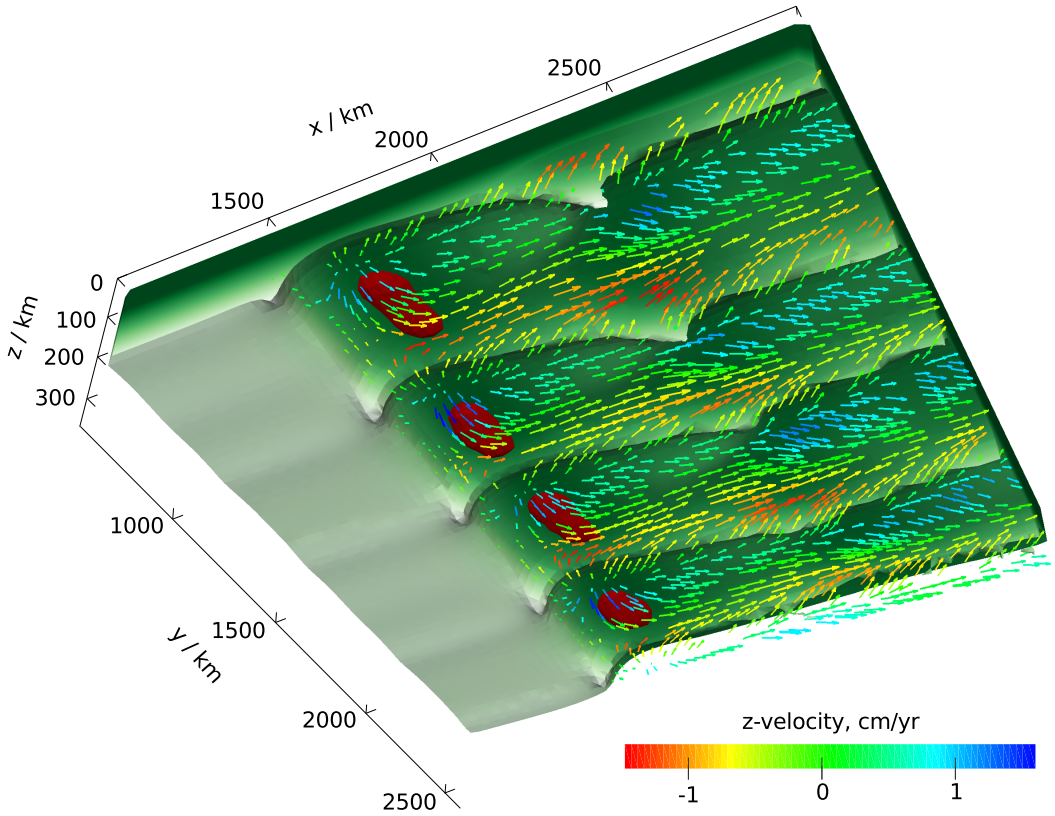

Figure 4.7: Three-dimensional structure of the EDC. The bottom of the lithosphere ($1200°\mathrm{C}$ isotherm) is shown in green. Dark red shows areas of active melting. Arrows show the velocity field at depth $z = 145\,\mathrm{km}$, colours of the arrows indicating the velocity's z-component. The edge-parallel flow (see text for discussion) can be seen near the melting pockets. Used model parameters are $E = 150\,\mathrm{kJ\,mol^{-1}}$, $Q = 19 \times 10^{-12}\,\mathrm{W\,kg^{-1}}$, $X_{\mathrm{H_2O}} = 300\,\mathrm{ppm}$.

in the middle of these rolls whereas in between the rolls the downwelling ridges effectively prohibits the formation of lithosphere erosion by EDC. This causes the melting regions of the EDC to be split into separate pockets along the edge.

4.4 Discussion

The style of the edge-driven convection shown in the results differs from the style envisaged by most previous studies on EDC. The cold downwelling at the edge of the lithosphere thickness gradient dominates the EDC *sensu stricto*, whereas in the results shown here the flow is governed by cold downwellings and hot upwellings in turns, resulting in the periodic nature of the EDC where EDC s.s. and EDC with shear alternate. For EDC w.s. to take place, higher sub-lithospheric mantle temperatures are needed beneath the thicker (proton) lithosphere. The horizontal temperature difference is modest, from 0.5 % to 4 % of the mantle potential temperature. This is in range of values found to be produced by continental insulation (Heron and Lowman, 2014). Although it is unclear whether this amount of excess heat can account for supercontinent dispersion, our results show that even modest effect of insulation may change the mantle dynamics at the edge of the thick lithosphere. In our models the thicker lithosphere covers 25 % of the surface area, or, assuming symmetricity over z-axis, represents a craton of 2000 km in width. This surface coverage is at lower end of the scale used by Heron and Lowman (2014). Larger coverage, with higher horizontal temperature difference, might have a strengthening effect on the EDC w.s.

We found a negative correlation between V_{rms} and $\Delta T_{\mathrm{pot,pr/te}}$, which, although weaker than that found by Heron and Lowman (2014), is consistent with their observation that "the influence of continental insulation is seen to decrease as the vigor of convection is increased". The weakness of the correlation in our results is probably due to the other factors being varied in the input parameters (changes in viscous activation energy and water contents affecting effective viscosity).

A flow field similar to EDC w.s. could be produced by combination of purely downwelling driven EDC (EDC s.s.) combined with lithospheric plate movement relative to the underlying mantle (i.e. lithosphere moving to the left in Fig 4.1b) (cf. Conrad et al., 2010). In this case no horizontal temperature difference (continental insulation) would be needed. However, in case of the Moroccan Atlas mountains (see below), this scenario is unlikely as the African plate has been moving (in fixed hotspot reference frame) more or less parallel to the craton edge (Morgan and Morgan, 2007).

Some of the models result in mantle potential temperatures that exceed values generally accepted for today's Earth. These results can be used to reflect the EDC process to earlier times in Earth's history or in a vicinity of a thermal anomaly in the modern Earth's mantle. Consistent with the negative correlation between V_{rms} and $\Delta T_{\mathrm{pot,pr/te}}$, the models with higher temperatures (and thus, generally higher V_{rms}) show smaller amounts of lithospheric erosion due to EDC (Fig 4.6c). Largest amount of lithospheric thinning is produced in the colder models, although these often show exceptionally high (tecton) lithospheric thicknesses. For EDC to be most effective in lithospheric thinning, a low value of viscous activation energy is needed ('mimicking' non-linear rheology, see Methods). Using low values of activation energy thickens the rheological transition layer between

asthenosphere and lithosphere, making the lithosphere-asthenosphere viscosity change more gradual and thus allowing easier erosion into this boundary layer (see discussion in 4.4.2 below).

No model with the smallest amount of water (100 ppm) produced melting (see Fig 4.6a), but models with 200 ppm or more water produce significant amounts of melting, suggesting that there is a rather abrupt change from no-melting domain to melt producing domain. This is due to the effect of water which lowers the mantle solidus but also enhances the lithosphere thinning near the edge via the exponential effect on mantle viscosity. A threshold for melting caused by the mantle water contents could also explain why volcanism by edge-driven convection is not a global phenomenon: mantle regions close to recent subduction zones might be slightly more hydrated than those far away, e.g. passive margins.

4.4.1 Application to Moroccan Atlas mountains and the 3D structure

The results support the hypothesis that the Cenozoic magmatism and related uplift in the Moroccan Atlas mountains has been produced by edge-driven convection (Missenard and Cadoux, 2012). It seems plausible that the style of EDC operating at the West African craton boundary is a combination of EDC *sensu stricto* and EDC with shear. These conclusions are supported by the following observations:

1) Estimated lithospheric thicknesses at the Atlas mountains area are: northwestern domain (Moroccan Meseta) 100-120 km, the craton side of the Atlas mountains about 180 km, and the lithosphere underneath the Atlas mountains about 80 km (Teixell et al., 2005). This combination of lithospheric thicknesses (proton ∼180 km, tecton ∼110-120 km) and erosion (30-40 km) can be found among the models. (These two models are circled in all panels in Fig 4.6 and used to plot Fig 4.5. Parameters for these models can be found in the caption of Fig 4.5). This thinned part of the lithosphere in the middle varies in width between 300 to 400 km, compatible with results shown here (cf. Fig 4.3a). It is noteworthy that no tecton lithospheric thicknesses were imposed in any of the models, and that they and the amount of lithospheric thinning are purely functions of imposed parameters $X_{\mathrm{H_2O}}$, Q and E.

2) The eruption rates in the volcanic provinces of the Atlas mountains vary between 1 and 30 $\mathrm{m\,Myr^{-1}}$ (total volume over covered area and duration of volcanism) during the volcanic phases (Missenard and Cadoux, 2012). Results here show magmatic production rates up to 60 $\mathrm{m\,Myr^{-1}}$ averaged over the total model time (including non-volcanic periods). The two models with compatible lithosphere thicknesses (point one above) show magmatic production rates of about 35 and 40-60 $\mathrm{m\,Myr^{-1}}$ during the volcanic phases. Even if not all of the mantle magmatism erupt at the surface, the volumes produced are compatible with those observed in the field.

3) The periodicity of the mantle magmatism varies between 14 and 26 Myrs. For the two example models discussed the periods are 26 and 17 Myrs. These periods match well with the duration of the $\sim$ 20 Myrs quiet gap between the volcanic episodes in the Atlas mountains (Missenard and Cadoux, 2012). Missenard and Cadoux (2012) suggest this quiet gap is caused by the changes in the velocity of the African plate, but our results show that such episodicity is an inherent feature in the EDC w.s. and can be explained without external forcing from plate movements. Observations

from duration of only one such volcanic period does not provide enough data to determine with certainty mechanisms responsible for it.

4) The three-dimensional structure of the EDC (Fig 4.7) shows that along the edge lithospheric erosion is not a continuous feature, but that the eroded "melting pockets" are separated by ridges of thicker lithosphere. This structure corresponds well to the tomographic results from the Atlas area (Bezada et al., 2014, see Fig 4.2) that shows distinct areas of thinning along the Atlas mountains axis (the Western High Atlas, the Central High Atlas and the Middle Atlas). Distinct areas of thinning under Central High Atlas and Middle Atlas are also observable from the geophysical models of Fullea et al. (2010) (based on elevation, gravity, surface heat flow, and geoid height data). The non-existence of single continuous thinned area under the Atlas mountains casts doubt on the hypothesis of a lithospheric corridor where the material of the Canarian mantle plume would flow northeast, as proposed by Duggen et al. (2009) on the basis of similar geochemistry of the volcanic rocks in the Atlas mountains region and the Canary island. However, the existence of a nearby plume could contribute to the decompression melting in the EDC by bringing in more fertile mantle material and more heat.

5) Based on their tomography results, Bezada et al. (2014) have suggested that the lithosphere underneath the Atlas mountains has experienced piecewise delamination. A fast Vp anomaly is located at 400 km depth in between the High and Middle Atlas, thought to represent a piece of delaminated lithosphere. Our models show that pieces of cold lithosphere with depleted asthenosphere incorporated in it can indeed be delaminated and brought into relatively deep mantle levels of 300-400 km (see Fig 4.4). The episodicity of the EDC w.s. can explain how the delamination under the Atlas mountains can take place piecewise. While our models utilize linear rheology parameterization, it is possible that a non-linear rheology can produce avalanche-like behaviour, where the erosion and delamination of the lithosphere is more punctuated than in linear rheology models (van Hunen et al., 2005).

The existence of partial melts in the melting pockets near the edge might also explain why the tomographic and gravity studies on lithosphere thickness in Atlas area generally agree but show small discrepancies in the absolute values of the lithosphere thickness (Palomeras et al., 2014): The partial melts (and depleted asthenospheric material) might have effects of different scale on seismic velocities and on gravity field, having especially strong effect on seismic S velocities. Observations of seismic S/SKS velocity splitting (Miller et al., 2013), aligned parallel to the lithospheric edge and the Atlas mountains, can be understood if regarded as manifestation of the horizontal flow present in the upper part of the convection rolls shown in the three-dimensional EDC model (Figure 4.7).

The tearing of the Betic-Alboran slab along the northern edge of the African plate from the Middle Miocene onwards (Thurner et al., 2014; Spakman and Wortel, 2004) may have contributed to the second, stronger pulse of the volcanism in the Atlas mountains. By allowing flow of hydrous mantle material from the overriding plate side of the subduction to the Atlas mountains area it could have enhanced the edge-driven convection, lithosphere erosion and melting.

4.4.2 Relations to steady state stagnant-lid convection scaling laws

Paying attention to the initial conditions of edge-driven convection models has been shown to be important (Sleep, 2007). Models with laterally homogeneous lithosphere thicknesses can cause instabilities of similar magnitude as those caused by thickness variation in the lithosphere if unrealistic initial conditions are applied. Initial conditions have to provide a mature stagnant-lid convection regime before edge-driven convection processes are examined, so that the thickness of the thermal boundary layer below the lithosphere is in a statistical steady state condition. An unrealistically thick thermal boundary layer drives excess sub-lithospheric small-scale convection (effectively a collapse of this overthickened lithosphere), which could be mistaken for an instability caused by the edge in the lithosphere.

Because the effective viscosity (water content) and the activation energy in our viscosity parameterization (controlling the thermal boundary layer thickness) are varied, we ensure that the rheology used in the models with different parameters produces steady-state stagnant lid convection. Test models with the same rheology as in the edge-driven convection models but with no imposed high-viscosity block (i.e. a laterally homogeneous lithosphere) has been run and resulting steady-state heat flow compared to expected heat flow for stagnant-lid convection. The steady state heat flow to the bottom of the continental lithosphere and, in the absence of radiogenic heating, at the surface of the lithosphere has been suggested to scale as

$$q_{\mathrm{ss}} = C_q k T_\eta^{4/3} \left[\frac{\rho g \alpha}{\kappa \eta_H}\right]^{1/3}, \tag{4.4}$$

where C_q is a constant with value ≈ 0.47, k is heat conductivity, T_η is a material property telling the temperature decrease needed to increase the viscosity by a factor of e, and η_H is the viscosity of the adiabatic half-space (Sleep, 2011; Davaille and Jaupart, 1993a; Davaille and Jaupart, 1993b). This scaling is for bottom-heated convection. Our models are internally heated, so we modify the equation to account for the heat flow component generated within the conductive lithosphere:

$$q_{\mathrm{ss,h}} = C_q k T_\eta^{4/3} \left[\frac{\rho g \alpha}{\kappa \eta_H}\right]^{1/3} + Q \rho h_L \,, \tag{4.5}$$

where h_L is the thickness of the stagnant lid, defined as the upper part of the model where average velocities are less than 0.01% of the maximum velocity within the whole model.

Our test models produce a good fit with the steady state stagnant lid heat flow (black line in Figure 4.8) although with different value of constant C_q and an intercept point of vertical axis different from zero. These discrepancies are largely explained by the effect of radiogenic heating within the lithosphere: if radiogenic heating within the lithosphere is reduced from the measured surface heat flow values, i.e. Equation (4.5) is applied, a slope much closer to $C_q = 0.47$ is found and the intercept with vertical axis is close to zero (red in Figure 4.8). The (thinner) tecton side of the actual edge-driven convection models are thus in a steady state stagnant lid convection regime at their initial stages and any additional instabilities are produced by the imposed edge in the lithosphere. Additionally, it can be concluded, that internally heated models of stagnant-lid convection adhere to the same scaling law as bottom-heated models.

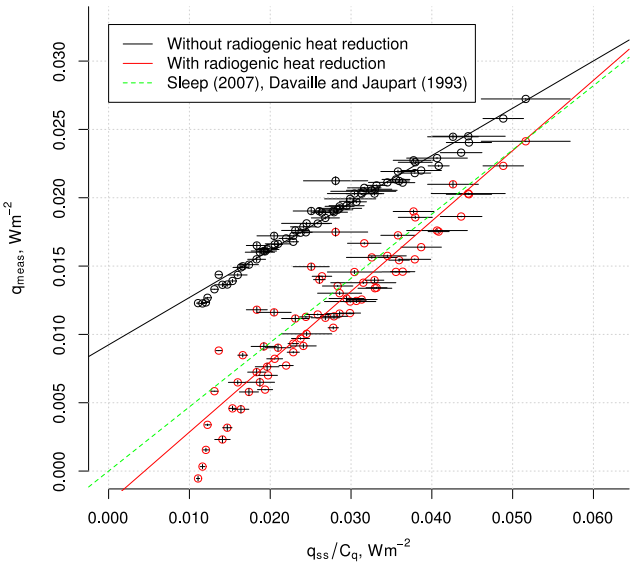

Figure 4.8: Stagnant lid heat flow, from scaling relationship versus measured surface values from the test models with no imposed lithosphere thickness variation. Circles represent time averaged values from models with different run parameters. Solid lines are best fit lines. Error bars show one standard deviation in time averaging. In red is shown the values from which the radiogenic heat production of the lithosphere (second term on the right in equation (4.5)) has been reduced. Green dashed line shows the slope $C_q = 0.47$, previously determined for bottom heated stagnant lid convection.

Melting during the model run changes the amount of water, and thus viscosity, and buoyancy of the mantle via Equations (4.1) and (4.3). This changes the values of ρ and T_η and/or η_H in Equations (4.4, 4.5). As the degree of melting and total depletion in the models turns out to be small and buoyancy is only linearly dependent on the depletion, the effect on buoyancy/density is small. However, the effect of depletion on viscosity is large, because the viscosity is inversely dependent on water content, which in turn has an exponential dependence on depletion. Viscosity increase caused by depletion is typically a factor of 2 to 5 in the models (locally). If depleted material remains in the convecting asthenosphere, η_H is affected, but the viscosity difference is quickly diluted via mechanical mixing, and the exponent $\frac{1}{3}$ in Equation (4.4) makes the change in η_H to contribute to q_{ss} only in minor amounts. If, however, depleted material stays part of the lithosphere at its bottom, the effective value of T_η at the depleted region is decreased, as compositional viscosity increase replaces some of the temperature change needed to increase the viscosity. From scaling relationships given by Sleep (2007), the value of T_η can be related to the thickness ΔZ_{rheo} of the thermal boundary layer that participates in the sub-lithospheric small-scale convection:

$$\Delta Z_{\text{rheo}} \propto T_\eta^{-\frac{1}{3}} . \tag{4.6}$$

This relationship becomes almost linear in the range of interest ($50 < T_\eta < 150\,\text{K}$). As the erosion and accretion of the thermal boundary layer produces most of the lithosphere thickness variation measured in the models, we can locally, next to the lithosphere edge, relate $\Delta Z_{\text{rheo}} \propto \Delta h_{\text{ed}}$, with negative proportionality constant. Thus

$$\Delta h_{\text{ed}} \propto T_\eta^{-\frac{1}{3}} , \tag{4.7}$$

also with negative proportionality constant. The periodicity seen in the models (Figure 4.5) can

now be understood as a repetition of following events: 1) Large ΔZ_{rheo} causes enhanced small-scale convection; 2) small-scale convection erodes the thermal boundary layer (ΔZ_{rheo} locally decreases, Δh_{ed} increases); 3) erosion allows decompression melting and gathering of depleted material; 4) more viscous depleted layer suppresses convective heating, allows conductive cooling, and thus an increase in ΔZ_{rheo}, decrease in T_η, and decrease in Δh_{ed} (4.7). This leads to 5) a situation similar to step 1, where the thermal boundary layer has thickened under the depleted layer. The depleted layer will be partially removed during subsequent lithosphere erosion (step 2 above). Similar chain of events can be recognized in sub-lithospheric small-scale convection (Kaislaniemi et al., 2014, Chapter 3) where no lithospheric edge is present. However, the edge in the lithosphere localizes the instabilities and allows more pronounced lithospheric erosion.

The effect of varying the activation energy on the amount of lithosphere thinning Δh_{ed} (Figure 4.6a), can be understood by examining the effect of E on T_η. The definition of T_η, that decreasing temperature from T_2 to T_1 increases viscosity by a factor of e, gives

$$\frac{\eta_0 \exp \frac{E+PV}{RT_1}}{\eta_0 \exp \frac{E+PV}{RT_2}} = e\,, \tag{4.8}$$

where

$$T_\eta = T_2 - T_1\,. \tag{4.9}$$

This leads to

$$T_\eta = T_2 - \left(\frac{R}{E+PV} + T_2^{-1}\right)^{-1}\,, \tag{4.10}$$

Increasing E thus produces decreasing T_η and, by (4.7), (almost linearly) decreasing Δh_{ed}, as in Figure 4.6a, where doubling E leads to reduction of Δh_{ed} by factor of $\sim \frac{1}{3}$, as shown by (4.7). Empirically, an inverse proportionality between E and T_η can be found in the range of interest ($120\,\mathrm{kJ} \leq E \leq 270\,\mathrm{kJ}$).

4.5 Conclusions

Numerical models support the hypothesis that the primary reason for the Cenozoic volcanism and its spatial and temporal distribution in the Atlas mountains region is the sub-lithospheric edge-driven convection with a shearing component induced by continental insulation. These two different styles of edge-driven convection, alternating in a periodic manner, can explain the volcanism with ∼20 Myrs quiet gap in the middle and the piecewise delamination of the lithosphere under the Atlas mountains. The three-dimensional lithospheric structure of the Atlas mountains region can be produced by edge-driven convection, causing non-continuous zone of thinned lithosphere parallel to the mountain chain, with pockets of lithosphere erosion and associated mantle melting.

References

Bai, Q. and D. L. Kohlstedt (1992). "Substantial hydrogen solubility in olivine and implications for water storage in the mantle". In: *Nature* 357, pp. 672–674.

Beauchamp, W., R. W. Allmendinger, M. Barazangi, A. Demnati, M. El Alji, and M. Dahmani (1999). "Inversion tectonics and the evolution of the High Atlas Mountains, morocco, based on a geological-geophysical transect". In: *Tectonics* 18.2, pp. 163–184.

Bezada, M. J., E. D. Humphreys, J. Davila, R. Carbonell, M. Harnafi, I. Palomeras, and A. Levander (2014). "Piecewise delamination of Moroccan lithosphere from beneath the Atlas Mountains". In: *Geochemistry, Geophysics, Geosystems* 15, pp. 975–985.

Calvert, A., E. Sandvol, D. Seber, M. Barazangi, S. Roecker, T. Mourabit, F. Vidal, G. Alguacil, and N. Jabour (2000). "Geodynamic evolution of the lithosphere and upper mantle beneath the Alboran region of the western Mediterranean: Constraints from travel time tomography". In: *Journal of Geophysical Research* 105.B5, pp. 10871–10898.

Christensen, U. (1984). "Convection with pressure- and temperature-dependent non-Newtonian rheology". In: *Geophysical Journal of the Royal Astronomical Society* 77, pp. 343–384.

Christensen, U. R. and D. A. Yuen (1985). "Layered Convection Induced by Phase Transitions". In: *Journal of Geophysical Research* 90.B12, pp. 10291–10300.

Conrad, C. P., B. Wu, E. I. Smith, T. A. Bianco, and A. Tibbetts (2010). "Shear-driven upwelling induced by lateral viscosity variations and asthenospheric shear: A mechanism for intraplate volcanism". In: *Physics of the Earth and Planetary Interiors* 178.3-4, pp. 162–175.

Coulon, C., M. Megartsi, S. Fourcade, R. C. Maury, H. Bellon, A. Louni-hacini, J. Cotten, A. Coutelle, and D. Hermitte (2002). "Post-collisional transition from calc-alkaline to alkaline volcanism during the Neogene in Oranie (Algeria): magmatic expression of a slab breakoff". In: *Lithos* 62, pp. 87–110.

Davaille, A. and C. Jaupart (1993a). "Thermal convection in lava lakes". In: *Geophysical Research Letters* 20.17, pp. 1827–1830.

– (1993b). "Transient high-Rayleigh-number thermal convection with large viscosity variations". In: *Journal of Fluid Mechanics* 253, pp. 141–166.

Dixon, J. E., T. H. Dixon, D. R. Bell, and R Malservisi (2004). "Lateral variation in upper mantle viscosity: role of water". In: *Earth and Planetary Science Letters* 222.2, pp. 451–467.

Duggen, S. (2005). "Post-Collisional Transition from Subduction- to Intraplate-type Magmatism in the Westernmost Mediterranean: Evidence for Continental-Edge Delamination of Subcontinental Lithosphere". In: *Journal of Petrology* 46.6, pp. 1155–1201.

Duggen, S., K. A. Hoernle, F. Hauff, A. Klugel, M. Bouabdellah, and M. Thirlwall (2009). "Flow of Canary mantle plume material through a subcontinental lithospheric corridor beneath Africa to the Mediterranean". In: *Geology* 37.3, pp. 283–286.

El Azzouzi, M., J. Bernard-Griffiths, H. Bellon, R. C. Maury, A. Piqué, S. Fourcade, J. Cotten, and J. Hernandez (1999). "Évolution des sources du volcanisme marocain au cours du Néogène". In: *Comptes Rendus de l'Académie des Sciences - Series IIA - Earth and Planetary Science* 329, pp. 95–102.

El Azzouzi, M., R. C. Maury, H. Bellon, N. Youbi, J. Cotten, and F. Kharbouch (2010). "Petrology and K-Ar chronology of the Neogene-Quaternary Middle Atlas basaltic province, Morocco". In: *Bulletin de la Société Géologique de France* 181.3, pp. 243–257.

Elder, J. (1976). *The Bowels of the Earth*. Oxford: Oxford University Press, p. 222.

Farr, T. G., P. A. Rosen, E. Caro, R. Crippen, R. Duren, S. Hensley, M. Kobrick, M. Paller, E. Rodriguez, L. Roth, et al. (2007). "The Shuttle Radar Topography Mission". In: *Reviews of Geophysics* 45.RG2004.

Fei, H., M. Wiedenbeck, D. Yamazaki, and T. Katsura (2013). "Small effect of water on upper-mantle rheology based on silicon self-diffusion coefficients". In: *Nature* 498.13 June, pp. 213–215.

Frizon de Lamotte, D., B. S. Bezar, and R. Bracène (2000). "The two main steps of the Atlas building and geodynamics of the western Mediterranean". In: *Tectonics* 19.4, pp. 740–761.

Fullea, J., M. Fernàndez, J. C. Afonso, J. Vergés, and H. Zeyen (2010). "The structure and evolution of the lithosphere-asthenosphere boundary beneath the Atlantic-Mediterranean Transition Region". In: *Lithos* 120.1-2, pp. 74–95.

Gerya, T. V. and D. A. Yuen (2003). "Characteristics-based marker-in-cell method with conservative finite-differences schemes for modeling geological flows with strongly variable transport properties". In: *Physics of the Earth and Planetary Interiors* 140.4, pp. 293–318.

Gomez, F., R. Allmendinger, M. Barazangi, A. Er-Raji, and M. Dahmani (1998). "Crustal shortening and vertical strain partitioning in the Middle Atlas Mountains of Morocco". In: *Tectonics* 17.4, pp. 520–533.

Griffin, W. L., S. Y. O'Reilly, N. Abe, S. Aulbach, R. M. Davies, N. J. Pearson, B. J. Doyle, and K. Kivi (2003). "The origin and evolution of Archean lithospheric mantle". In: *Precambrian Research* 127, pp. 19–41.

Gurnis, M. (1988). "Large-scale mantle convection and the aggregation and dispersal of supercontinents". In: *Nature* 332, pp. 695–699.

Hardebol, N. J., R. N. Pysklywec, and R. Stephenson (2012). "Small-scale convection at a continental back-arc to craton transition: Application to the southern Canadian Cordillera". In: *Journal of Geophysical Research* 117.B1, B01408.

Heron, P. J. and J. P. Lowman (2014). "The impact of Rayleigh number on assessing the significance of supercontinent insulation". In: *Journal of Geophysical Research: Solid Earth* 119, pp. 711–733.

Hirth, G. and D. L. Kohlstedt (1996). "Water in the oceanic upper mantle: implications for rheology, melt extraction and the evolution of the lithosphere". In: *Earth and Planetary Science Letters* 144, pp. 93–108.

Janse, A. J. A. (1994). "Is Clifford's rule still valid? Affirmative examples from around the world". In: *Diamonds: Characterization, Genesis and Exploration*. Ed. by H. Meyer and O Leonardos. Dept. Nacional da Prod. Mineral., Brazilia, pp. 215–235.

Kaislaniemi, L., J. van Hunen, M. B. Allen, and I. Neill (2014). "Sublithospheric small-scale convection–A mechanism for collision zone magmatism". In: *Geology* 42.4, pp. 291–294.

Karato, S.-i. (2010). "Rheology of the deep upper mantle and its implications for the preservation of the continental roots: A review". In: *Tectonophysics* 481.1-4, pp. 82–98.

Karato, S.-i. and P. Wu (1993). "Rheology of the Upper Mantle: A Synthesis". In: *Science* 260.5109, pp. 771–778.

Katz, R. F., M. Spiegelman, and C. H. Langmuir (2003). "A new parameterization of hydrous mantle melting". In: *Geochemistry Geophysics Geosystems* 4.9, p. 1073.

King, S. D. and J. Ritsema (2000). "African Hot Spot Volcanism: Small-Scale Convection in the Upper Mantle Beneath Cratons". In: *Science* 290, pp. 1137–1140.

King, S. D. and D. L. Anderson (1995). "An alternative mechanism of flood basalt formation". In: *Earth and Planetary Science Letters* 136.3-4, pp. 269–279.

– (1998). "Edge-driven convection". In: *Earth and Planetary Science Letters* 160.3-4, pp. 289–296.

Kohlstedt, D. L., B. Evans, and S. J. Mackwell (1995). "Strength of the lithosphere: Constraints imposed by laboratory experiments". In: *Journal of Geophysical Research* 100.B9, pp. 17587–17602.

Maury, R. C., S. Fourcade, C. Coulon, M. El Azzouzi, H. Bellon, A. Coutelle, A. Ouabadi, B. Semroud, M. Megartsi, J. Cotten, et al. (2000). "Post-collisional Neogene magmatism of the Mediterranean Maghreb margin: a consequence of slab breakoff". In: *Comptes Rendus de l'Académie des Sciences - Series IIA - Earth and Planetary Science* 331.3, pp. 159–173.

Mei, S. and D. Kohlstedt (2000). "Influence of water on plastic deformation of olivine aggregates 1 . Diffusion creep regime". In: *Journal of Geophysical Research* 105, pp. 21457–21469.

Miller, M. S. and T. W. Becker (2014). "Reactivated lithospheric-scale discontinuities localize dynamic uplift of the Moroccan Atlas Mountains". In: *Geology* 42.1, pp. 35–38.

Miller, M. S., A. A. Allam, T. W. Becker, J. F. Di Leo, and J. Wookey (2013). "Constraints on the tectonic evolution of the westernmost Mediterranean and northwestern Africa from shear wave splitting analysis". In: *Earth and Planetary Science Letters* 375, pp. 234–243.

Missenard, Y. and A. Cadoux (2012). "Can Moroccan Atlas lithospheric thinning and volcanism be induced by Edge-Driven Convection?" In: *Terra Nova* 24.1, pp. 27–33.

Missenard, Y., H. Zeyen, D. Frizon de Lamotte, P. Leturmy, C. Petit, M. Sébrier, and O. Saddiqi (2006). "Crustal versus asthenospheric origin of relief of the Atlas Mountains of Morocco". In: *Journal of Geophysical Research* 111.B3, B03401.

Mokhtari, A. and D. Velde (1988). "Xenocrysts in Eocene camptonites from Taourirt, northern Morocco". In: *Mineralogical Magazine* 52, pp. 587–601.

Moresi, L. and M. Gurnis (1996). "Constraints on the lateral strength of slabs from three-dimensional dynamic flow models". In: *Earth and Planetary Science Letters* 138, pp. 15–28.

Morgan, W. J. and J. P. Morgan (2007). "Geological Society of America Special Papers". In: *Geological Society of America Special Papers* 430, pp. 65–78.

Palomeras, I., S. Thurner, A. Levander, K. Liu, A. Villasenor, R. Carbonell, and M. Harnafi (2014). "Finite-frequency Rayleigh wave tomography of the western Mediterranean: Mapping its lithospheric structure". In: *Geochemistry, Geophysics, Geosystems* 15.1, pp. 140–160.

Piqué, A., P. Tricart, R. Guiraud, E. Laville, S. Bouaziz, M. Amrhar, and R. A. Ouali (2002). "The Mesozoic-Cenozoic Atlas belt (North Africa): an overview". In: *Geodinamica Acta* 15.3, pp. 185–208.

Rachdi, H., M. Berrahma, M. DeLaloye, A. Faure-Muret, and M. Dahmani (1997). "Le volcanisme tertiaire du Rekkame (Maroc): pétrologie, géochimie et géochronologie". In: *Journal of African Earth Sciences* 24.3, pp. 259–269.

Ramdani, F. (1998). "Geodynamic implications of intermediate-depth earthquakes and volcanism in the intraplate Atlas mountains (Morocco)". In: *Physics of the Earth and Planetary Interiors* 108, pp. 245–260.

Schubert, G., D. L. Turcotte, and P. Olson (2001). *Mantle Convection in the Earth and Planets.* Cambridge: Cambridge University Press, p. 940.

Schutt, D. L. and C. E. Lesher (2006). "Effects of melt depletion on the density and seismic velocity of garnet and spinel lherzolite". In: *Journal of Geophysical Research* 111.B5, pp. 1–24.

Seber, D., M. Barazangi, B. A. Tadili, M. Ramdani, A. Ibenbrahim, and D. B. Sari (1996). "Three-dimensional upper mantle structure beneath the intraplate Atlas and interplate Rif mountains of Morocco". In: *Journal of Geophysical Research* 101.B2, pp. 3125–3138.

Shahnas, M. H. (2004). "Anomalous topography in the western Atlantic caused by edge-driven convection". In: *Geophysical Research Letters* 31.L18611.

Sleep, N. H. (2007). "Edge-modulated stagnant-lid convection and volcanic passive margins". In: *Geochemistry, Geophysics, Geosystems* 8.Q12004.

– (2011). "Small-scale convection beneath oceans and continents". In: *Chinese Science Bulletin* 56.13, pp. 1292–1317.

Spakman, W. and M. J. R. Wortel (2004). "Tomographic View on Western Mediterranean Geodynamics". In: *The TRANSMED Atlas. The Mediterranean Region from Crust to Mantle.* Ed. by W Cavazza, F Roure, W Spakman, G. M. Stampfli, and P Ziegler. Berlin, Heidelberg: Springer, pp. 31–52.

Teixell, A., M.-L. Arboleya, M. Julivert, and M. Charroud (2003). "Tectonic shortening and topography in the central High Atlas (Morocco)". In: *Tectonics* 22.5, p. 1051.

Teixell, A., P. Ayarza, H. Zeyen, M. Fernandez, and M.-L. Arboleya (2005). "Effects of mantle upwelling in a compressional setting: the Atlas Mountains of Morocco". In: *Terra Nova* 17.5, pp. 456–461.

Teixell, A., G. Bertotti, D. Frizon de Lamotte, and M. Charroud (2009). "The geology of vertical movements of the lithosphere: An overview". In: *Tectonophysics* 475.1, pp. 1–8.

Thurner, S., I. Palomeras, A. Levander, R. Carbonell, and C.-T. Lee (2014). "Ongoing lithospheric removal in the western Mediterranean: Evidence from Ps receiver functions and thermobarometry of Neogene basalts (PICASSO project)". In: *Geochemistry, Geophysics, Geosystems* 15, pp. 1113–1127.

Wagner, C., A. Mokhtari, E. Deloule, and F. Chabaux (2003). "Carbonatite and Alkaline Magmatism in Taourirt (Morocco): Petrological, Geochemical and Sr-Nd Isotope Characteristics". In: *Journal of Petrology* 44.5, pp. 937–965.

Zhong, S., M. T. Zuber, L. Moresi, and M. Gurnis (2000). "Role of temperature-dependent viscosity and surface plates in spherical shell models of mantle convection". In: *Journal of Geophysical Research* 105.B5, pp. 11063–11082.

van Hunen, J., S. Zhong, N. Shapiro, and M. Ritzwoller (2005). "New evidence for dislocation creep from 3-D geodynamic modeling of the Pacific upper mantle structure". In: *Earth and Planetary Science Letters* 238.1-2, pp. 146–155.

van Wijk, J. W., W. S. Baldridge, J. van Hunen, S. Goes, R. Aster, D. D. Coblentz, S. P. Grand, and J. Ni (2010). "Small-scale convection at the edge of the Colorado Plateau: Implications for

topography, magmatism, and evolution of Proterozoic lithosphere". In: *Geology* 38.7, pp. 611–614.

Chapter 5

Crustal melting due to lithospheric thinning after continental collision: Application to the Variscan and Svecofennian orogenies

5.1 Introduction

The traditional classification of an orogenic sequence into synorogenic, late orogenic, post-orogenic and anorogenic is blurred by the fact that the radiometric datings of associated rocks overlap (Väisänen et al., 2000). Bonin et al. (1998) uses nomenclature where post-collisional (i.e. late orogenic) marks the end of the main collision event but implies still continuing convergence and forming of orogenic plateaux. The end of the post-collisional stage is marked by extensional episodes accompanied by lithospheric thinning and gravitational collapse of the crust. This marks also the transition into the post-orogenic stage where high-K calc-alkaline to ultrapotassic bimodal magmatic suites shift into more clearly alkaline within-plate magmatic suites (Bonin, 2004).

Generation of post-collisional mafic magmatism has invoked a multitude of explanations, from slab break-off (Davies and Blanckenburg, 1995) and whole mantle delamination (Bird, 1979; Pearce et al., 1990) to small-scale convection (Kaislaniemi et al., 2014). The source of these rocks, however, is generally agreed to be in the subduction-modified depleted lithospheric and/or asthenospheric mantle, based on the isotopic and rare Earth element characteristics of the rocks (e.g. Dilek and Altunkayanak, 2007; Miller et al., 1999; Williams, 2004). The generation of the felsic magmatism, however, remains a debated issue. A review by Bonin (2004) argues for a same mantle source for the post-orogenic mafic and felsic rocks and, with transition from post-collisional to post-orogenic, for a

decreasing role of the crust in this magmatism, evolving to the direction of intra-plate (anorogenic) magmatism. Contrary to this, Liégeois et al. (1998) suggest that the differences between post-collisional high-K suites and post-orogenic alkaline suites are linked to the sources themselves, and only to a lesser degree to the differentiation process.

In addition, the heat source for the crustal melt production in post-collisional setting has been a subject of extensive research. It is now generally agreed that unless a significant crustal thickening (∼doubling the thickness) takes place, the increased radiogenic heating alone cannot produce extensive crustal melting (Bea, 2012; Thompson and Connolly, 1995). It is probable that the anomalously >70 km thick crust of the Tibet contains partially molten layers (Nelson et al., 1996; Holt and Wallace, 1990). Also, thermal modelling (Kukkonen and Lauri, 2009) of the Paleoproterozoic Svecofennian orogeny has shown that a rapid thickening of the crust up to 70 km total thickness could produce temperatures high enough for partial crustal melting and granite production. However, in cases like the Variscan orogeny, with high temperature and low pressure metamorphism, implying only modest amounts of crustal thickening, lithospheric thinning (e.g. Franke, 2000) and underplating of mafic magmas (Williamson et al., 1992) have been considered perhaps more probable causes for crustal melting. Seismic studies showing strong reflections at the moho level have been used to argue for magmatic underplating, as for example is the case in the south-west of the Svecofennian orogeny (Korsman et al., 1999). It is well established that intrusion of mafic magma into the crust will cause crustal anatexis (Huppert and Sparks, 1988), but the volume of crustal melting, in magnitude similar to the volume of intruding mafic melt, is too small to explain all the crustal melts. Arguments for and against advective mantle derived heating have also been based on the fact that some of the Variscan granitoids show signatures of mixing of mantle- and crustal-derived magmas, while most of them do not (Gerdes et al., 2000). Mafic enclaves within post-collisional granitoids (e.g. Couzinié et al., 2014), called vaugnerites in the French Massif Central, evidense mingling of mafic and felsic magmas, interpreted to show coeval crustal anatexis and intrusion of mantle-derived melts.

Inherently associated with continental collisions is the formation of migmatite-granite terranes, exposed at locations of eroded mountain belts. The formation of these terranes is caused by the heating during the orogenic event, whether by radiogenic or mantle derived heating, as discussed above. Migmatitic domains are best exposed in so called metamorphic core complexes and multi-diapiric domes, allowing the lower to mid-crust to be exhumed. Thus, interest has risen as to what was the exhumation process of these formations. Two main hypotheses have been put forward (e.g. Vanderhaeghe et al., 1999): 1) an extensional stress field causing lithosphere scale shear zone, or 2) the ductile middle/lower crust localizes extensional stress field in the upper brittle crust. In both cases, a late-orogenic "collapse" of the orogen follows, with rapid exhumation of the middle crust.

In the French Massif Central, the Velay dome (Ledru et al., 2001) is a good example of such post-orogenic migmatitic domain, relating to the collapse of the Variscan orogen: Migmatization of the crust took place during about 340 Ma to 310 Ma, after collisional nappe stacking and regional foliation during about 340-335 Ma (Couzinié et al., 2014; Faure et al., 2009; Ledru et al., 2001). This was followed by a period of granitic magmatism at about 310-300 Ma. The granitic suites are closely associated with vaugnerites, Mg-K-rich diorites, cropping out as intrusive bodies or

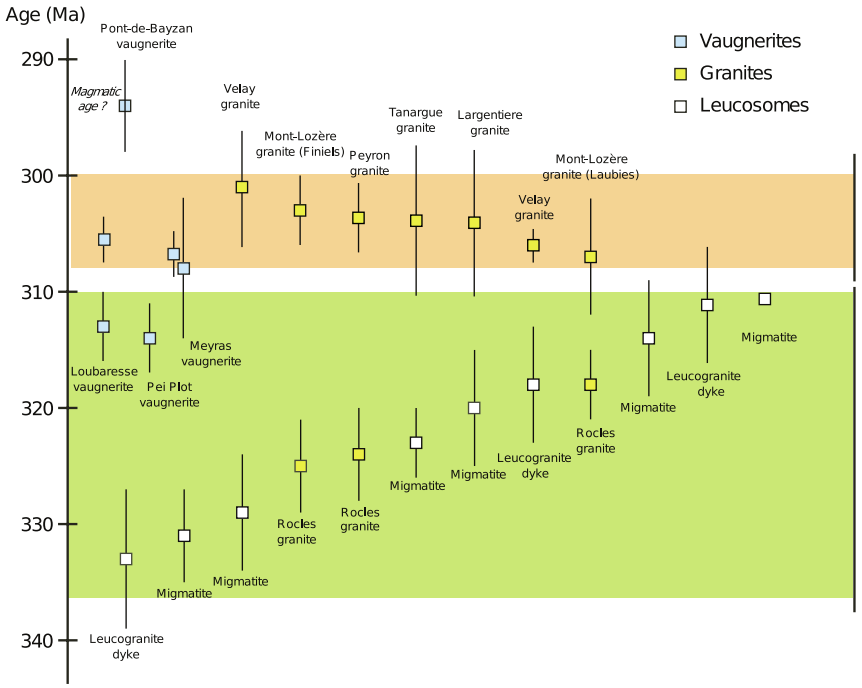

Figure 5.1: Magmatic history of the Velay dome region. Figure modified from Couzinié et al. (2014) and data collected by Couzinié et al. themselves or from references therein. Datings are by U-Pb method. Migmatization and anatexis is followed by pervasive crustal melting and production of granitic plutons from 310 Ma onwards. Mantle-derived vaugnerites are dated to the time of the transition.

enclaves within the felsic rocks. The vaugnerites were emplaced during the time of transition from migmatite to granite formation. Granulite facies metamorphism of base of the Variscan crust took place at about 300 Ma (Costa and Rey, 1995). Couzinié et al. (2014) interpret the events as long-lived partial melting of different crustal source that at about 310 Ma reached the critical melt percentage and was extracted, forming the plutonic bodies. It is unclear whether the associated mantle-derived vaugnerites were the cause of this enhanced melting or whether they were a consequence of the same process causing the destabilization of the partially molten crust and sudden pulse of magmatism at 310-300 Ma. The exhumation of the Velay dome, i.e. the doming, is thought to take place at the same time via a large scale detachment (Bouilhol et al., 2006).

In the southern part of the Paleoproterozoic Svecofennian orogeny, a >500 km long granite-migmatite zone comprises the southern Finland (Väisänen et al., 2000). The main collisional stage took place at 1.89-1.87 Ga, but a late orogenic metamorphic peak took place at 1.83 to 1.81 Ga. High temperature low pressure granulites, indicating high heat flow, and bimodal shoshonitic magmatism with is present throughout the migmatite zone. Seismic studies have been interpreted to show mafic underplating in the western part of the zone (Korsman et al., 1999). Extension of crust took place at about 1.83-1.82 Ga (Nironen and Kurhila, 2008; Skyttä and Mänttäri, 2008). U-Pb ages of the leucogranites within the belt show emplacement during a 70 Myrs period from 1.86 Ga to 1.79 Ga (Kurhila et al., 2010).

Common to both the Variscan Velay migmatite dome and the Svecofennian southern Finland

migmatite belt are an extended period of partial crustal melting ending in formation of granitic plutons and extensional tectonics (orogenic collapse). Both have closely associated mantle-derived mafic rocks implying involvement of mantle melting in the generation of the crustal melts.

The aim of this study is to produce a general model of post-collisional/-orogenic lithosphere-asthenosphere dynamics, combined with a chemical model to examine the effects of mantle melt intrusion at crust-mantle transition zone (moho) to the production of partial crustal melts. We present a new tool for coupled modelling of mantle convection and mantle/crustal melting with dynamic feedback mechanisms between melting, depletion, melt weakening, depletion stiffening and residue/melt composition evolution during melt removal. We inspect the consequences of lithospheric thinning caused by post-collisional sub-lithospheric small-scale convection (Kaislaniemi et al., 2014), and especially its effects on production of crustal anatexis.

5.2 Methods and model setup

We use numerical finite element methods (Moresi and Gurnis, 1996; Zhong et al., 2000) to investigate the dynamics of mantle and lower crust after continental collision. We investigate small-scale convection taking place at the asthenosphere-lithosphere boundary, caused by the addition of small amounts of viscosity reducing water in to the upper mantle during the pre-collisional subduction stage. This small-scale convection leads to localized non-permanent mantle thinning and, in some cases, to decompression melting of the asthenospheric rocks (Kaislaniemi et al., 2014, Chapter 3). We assume an initial water content of the mantle (400 wt ppm), assumed to be left over from the previous subduction. This leads to relatively strong localized intermittent thinning of the lithosphere but is not itself enough to lower the viscosity to an extent that the lithospheric mantle as whole would be destabilized.

We have run models with different parameters to study the effects of melt weakening, underplating of magmas, and depletion induced residue stiffening (Table 5.1).

Model	Melt weakening	Mantle melt extraction	Crustal melt extraction
A	Off	Off	Off
B	On	Off	Off
C	On	On	Off
D	On	On	On

Table 5.1: Varied parameters in the models presented. For details of melt weakening and melt extraction, see below.

The model set-up (Fig 5.2) consists of 2640 by 660 km domain divided into 128 and 64 elements for the finite element calculation. Domain boundaries are closed, having free-slip stress boundary conditions. Constant temperature at the surface and at the bottom (adiabatic temperature) is described. A compositional buoyancy of the crust and of the lithospheric mantle is used as the buoyancy of the lithospheric mantle might be an important factor when considering the stability of the lithospheric mantle (Poudjom Djomani et al., 2001). The initial domain is divided into crust and mantle, for which different melting models are used (see below). The man-

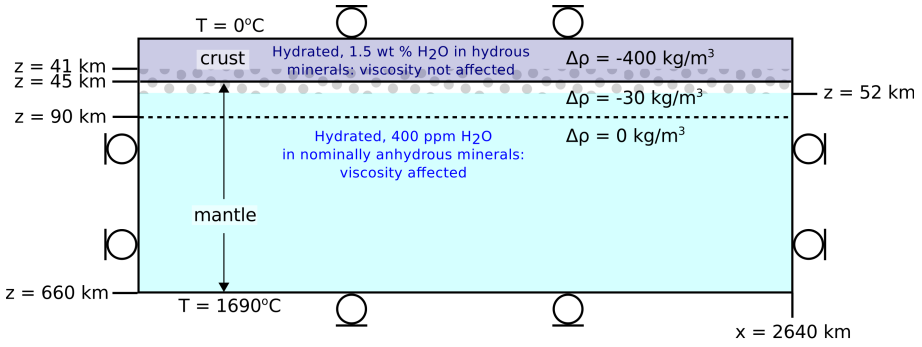

Figure 5.2: Model set-up (not to scale). See text for details.

tle is hydrated with 400 ppm of water contributing to the viscosity and the solidus temperature of the rock. The crust has a initial water content of 1.5 wt-% stored in the hydrous minerals, assumed not to lower the viscosity. A tracer advection or marker-in-cell method (Gerya and Yuen, 2003) is used and the material boundaries described are implemented with these tracers. As the tracers are advected with the velocity field during the model run, the boundaries may move as the model evolves: each tracer is identified as having a crustal or mantle lithology, carrying related information (density, chemical composition). The region between z=41 km and z=52 km is the depth where possible mantle melts from larger depths are advected to (magmatic underplating, see below).

5.2.1 Mantle convection model

We solve the non-dimensional equations for conservation of mass, momentum and energy (Moresi and Gurnis, 1996; Zhong et al., 2000). Adiabatic heating, shear heating and heating by radioactive elements is taken into account (extended Boussinesq approximation, Christensen and Yuen, 1985). A linear temperature, pressure and water content dependent rheology is used, similar to the one used in Kaislaniemi et al. (2014), extended with a melt weakening parameterization:

$$\eta = \eta_0 \eta_\phi 100^{\frac{X_{\mathrm{H_2O}}}{a+X_{\mathrm{H_2O}}}} \exp\left(\frac{E+PV}{RT_{\mathrm{abs}}}\right) \exp\left(-\frac{E+P_0V}{RT_{\mathrm{abs},0}}\right) , \tag{5.1}$$

where η is the effective viscosity, η_0 reference viscosity, η_ϕ melt weakening coefficient (see below), $X_{\mathrm{H_2O}}$ water content of the nominally anhydrous minerals in the mantle, a a parameter controlling how large $X_{\mathrm{H_2O}}$ has to be to lower the viscosity by one order of magnitude, E activation energy, lithostatic P pressure, V activation volume, R gas constant, T_{abs} temperature, P_0 reference pressure, and $T_{\mathrm{abs},0}$ reference temperature. See Table 5.2 for values of these parameters.

Parameter a is chosen so that background concentrations of water ($X_{\mathrm{H_2O}} \approx 120\,\mathrm{wt\,ppm}$, Dixon et al., 2004) in the mantle do not lead to considerably lower mantle viscosities, but increased values of $X_{\mathrm{H_2O}}$ do enhance the sub-lithospheric small-scale convection.

Melt weakening of the rock, caused by the partial melts occupying grain boundaries, is parameterized with a relation

Parameter	Symbol	Value used
Activation energy	E, $\mathrm{kJ\,mol^{-1}}$	120
Activation volume	V, $\mathrm{m^3\,mol^{-1}}$	6×10^{-6}
Radiogenic heating	Q, $10^{-12} \times \mathrm{W\,kg^{-1}}$	19
Reference temperature	$T_{\mathrm{abs},0}$, K	1623
Reference pressure	P_0, Pa	21.4×10^9
Reference viscosity	η_0, Pa s	10^{22}
Reference density	ρ_0, $\mathrm{kg\,m^{-3}}$	3300
Latent heat of melting	L, $\mathrm{kJ\,kg^{-1}}$	560
Coefficient of thermal expansion	α, $\mathrm{K^{-1}}$	3.5×10^{-5}

Table 5.2: Values of physical parameters used in the models.

$$\frac{\dot{\epsilon}(\phi)}{\dot{\epsilon}(0)} = \exp(\alpha\phi) \tag{5.2}$$

(Mei et al., 2002), where $\dot{\epsilon}$ is the strain rate, ϕ is the melt fraction and $\alpha \approx 26$ in diffusion creep regime. With a linear rheology, this converts to

$$\frac{\eta(\phi)}{\eta(0)} = \exp(-\alpha\phi) = \eta_\phi\,, \tag{5.3}$$

which is then used in Eq (5.1).

For the lithospheric/crustal structure we used the so called "jelly sandwich" rheology model where the middle to lower crust is significantly weaker than the upper crust and the lithospheric mantle (Ranalli and Murphy, 1987; Kohlstedt et al., 1995; Wang et al., 2012). The cause of this weak layer is the thermally activated creep of the wet quartz and feldspars below the brittle/ductile transition depth (Rybacki et al., 2006) but we simplify the rheological model by using same diffusion creep rheology for both the crust and the mantle and lowering the effective viscosity of the crust by two orders of magnitude. Together with the high temperature dependency of the viscosity this leads to an effective viscosity profile where there is a significant weakening in the transition from mantle to lower crust but then at the shallower depths viscosity is quickly increased again.

5.2.2 Dynamic integration of melting models

During the calculation of the mantle convection model, at each time step, melting models are used to determine whether crustal or mantle melts are formed. For mantle melts, the experiment-based hydrous melting parameterization by Katz et al. (2003) is used. This parameterization estimates the extent of melting and the melt's water content as a function of pressure, temperature and bulk water content of the peridotitic rock.

For crustal lithologies, a thermodynamic code *PerpleX* (Connolly, 2005) is used. Using thermodynamic information of the rock's constituent minerals, the equilibrium mineralogical assemblage, including any melt phases, is calculated using Gibbs energy minimization strategy. As an input data, the bulk composition of the rock, the temperature and the pressure are needed. *PerpleX* calculates the amounts (wt-%) of the stable minerals in given conditions and the composition of

these minerals and of any melts, if present. The following major oxides are used in the calculations: H_2O, SiO_2, MgO, CaO, Al_2O_3, Na_2O, K_2O, FeO, and TiO_2. Thermodynamic data for minerals including solid solutions and their end-members are from Holland and Powell (1998), except for feldspars (Fuhrman and Lindsley, 1988), melt (White et al. (2001) with modified pressure dependency of sillimanite liquid from Bouilhol et al. (2014)) and the equation of state of water (Holland and Powell, 1991). A general averaged composition estimate (Rudnick and Fountain, 1995) for the lower crust of platform/shield areas has been used (Table 5.3). Initially water-undersaturated conditions are imposed with a water content of 1.5 %.

Oxide	Wt %
SiO_2	52.4
MgO	7.1
CaO	9.5
Al_2O_3	16.5
Na_2O	2.7
K_2O	0.6
FeO_T	8.2
TiO_2	0.8
H_2O	1.5

Table 5.3: Composition of the lower crust used in the models for thermodynamic phase equilibria calculations.

If melts are formed they may be removed or left in place, depending on the model parameters. If melts are left in place, the bulk composition of the rock is not modified and the latent heat of fusion remains available for (re-)melting during the subsequent time steps; a thermal and chemical equilibrium is assumed between the melt and surrounding solid rock. If melt is removed, the bulk composition of the residue is modified accordingly and corresponding amount of latent heat is removed. For mantle rocks, the water content of the residue is decreased by the amount incorporated in the melt (assuming water behaves as an incompatible element with bulk distribution coefficient D=0.01). For the crustal rocks, the whole major element composition is modified according to the composition of the melt removed, and melt composition is given by the thermodynamic phase equilibria calculation performed with *PerpleX*.

Melts are either removed out of the model domain (to the surface, in case of crustal rocks) or from mantle to the moho level. Melt advection from mantle to the moho level causes the heat content of these melts to be distributed at the moho level, in a zone of 5 km in depth, comprising both the uppermost mantle and lowermost crust. This represents the underplating, crystallization, and thermal (but not chemical) equilibration of the mantle melts at the moho level.

Melt removal threshold is used for crustal rocks. In models where crustal melts are extracted, an 8% partial melt threshold is used; once partial melting exceeds this degree all the crustal melts produced are extracted. If the threshold is not exceeded, melts are left in place and are available for re-melting next time step. The 8% threshold represents a liquid percolation threshold (Vigneresse et al., 1996) at which point melt pockets become connected. Thus, the threshold used is a minimum estimation and the models, in this sense, give a maximum estimate for the amount of crustal melt extracted. No threshold is imposed for mantle melts; in models where mantle melts are extracted, any amount of melt is immediately advected to the crust-mantle transition zone.

When melts are extracted, the depletion parameter F is increased by the amount (wt-%) of melt extracted. Because depleted lherzolite is more buoyant than undepleted, the F in our models affects directly the buoyancy of the mantle residue, according to a relation given by Schutt and

Lesher (2006):

$$\frac{\mathrm{d}\ln\rho}{\mathrm{d}F_{\%}} = -0.00020 \ , \tag{5.4}$$

where $F_{\%} = 100F$.

Melt production rates are calculated during model runs. In models where melts are extracted, a production rate is expressed in units of m/Myr. This gives the change in the total thickness of the melt layer produced by extraction of melts. In models where melts are not extracted, a concept of *potential* melting volume is used. Melt production rate is expressed in the same units, but as no melts are extracted and the already melted rock remains available for re-melting during the next time steps, the resulting number in m/Myrs does not represent any real physical quantity. It merely describes how much, and by which rate, fertile rock could have been melted with the heat available. Potential melting amounts are therefore used to make comparisons between models.

5.3 Results

A complex interplay between melt weakening, depletion stiffening and chemical depletion can be observed in the models. All models produce sub-lithospheric small-scale convection patterns due to the decreased asthenospheric viscosity by small amounts of water in the mantle. This produces local temporal thinning of the lithosphere and asthenospheric decompression melting. Lithosphere thinning also raises the lithosphere geotherm, thus producing partial melts at the lower crust level. In models where melt weakening is enabled, partial crustal and asthenospheric melting with their viscosity lowering effects enhance the lithospheric thinning, producing a positive feedback (Fig 5.3), where crustal melting, once initiated by lithospheric thinning, sustains higher potential melt volumes than in models where no melt weakening takes place.

Extraction of melts from asthenospheric level to the moho level advects heat with them to the moho level, providing more energy for crustal melting. However, because extraction of the melts disables the melt weakening effect and because melt depletion dehydrates the asthenosphere and increases its effective viscosity, the thinning of the lithosphere is hindered by the asthenospheric melt extraction. Thus, the total effect of asthenospheric upward melt advection (underplating at crust-mantle transition zone) to the crustal melting is minor or even negative (Fig 5.4), considering the full dynamics of the system. The depleted mantle layer produced at the former thinned lithosphere region “shields” the lower crust from further melting. This effect is more clear in models with higher mantle water contents (i.e. where more mantle melts are produced). However, the shielding effect of the depleted layer will cease to exist if the layer is being convected back to the asthenosphere, re-exposing the fresh lithosphere to the convecting mantle. This can be seen in the increasing melting rate in Fig. 5.4 (red line) towards the end of the time line. Also, it is noteworthy, that the direct heating effect of the underplating is not changed, but that the prerequisities of underplating (extraction of mantle melts thus formation of a depleted layer) hinder further thinning of the lithosphere, indirectly preventing further underplating.

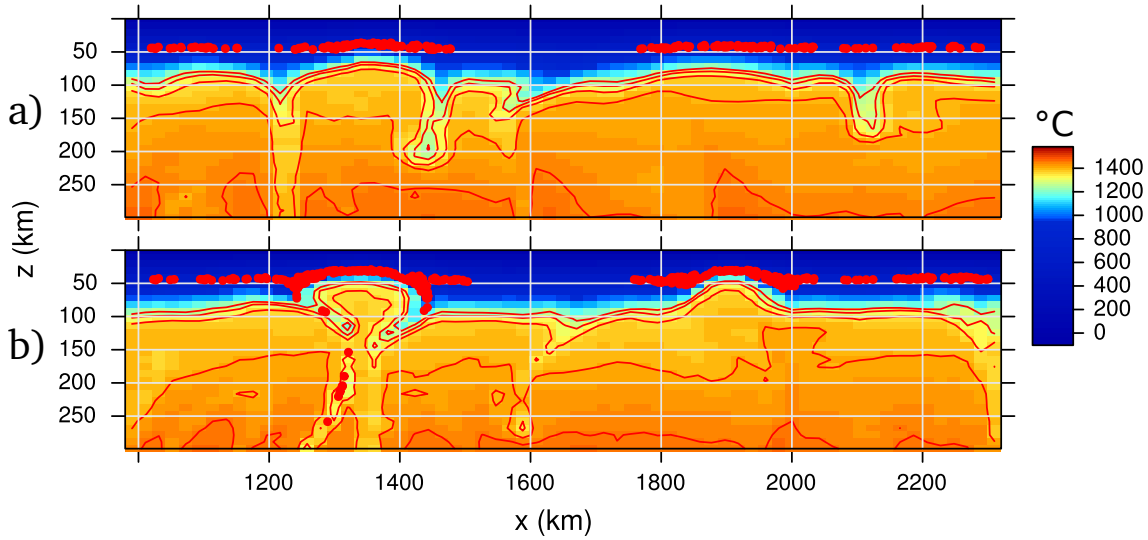

Figure 5.3: Temperature field of two models (A and B, Table 5.1) at t=68 Myrs. a) Model with melt weakening effects disabled. b) Model with melt weakening effects enabled. Both models show thinning caused by sub-lithospheric small-scale convection. Melt weakening (b) causes positive feedback and enhances lithospheric thinning.

Extraction of the crustal melts has a similar negative feedback effect on the continuance of the crustal melting, because melt removal leaves a residue that is more refractory in composition. However, partial melts, if not extracted, can continue to form. This explains the quiet period of few tens of millions of years before partial melt degrees exceed the limit for melt extraction (Fig 5.5). During this time, partial melts exist in the lower crust but with too low degree to be extracted. The residue composition is only affected at the end of this period when the melts are extracted.

The composition of the crustal melts overlap mainly with dacite and rhyolite fields of the diagram for total alkali vs silica content (Fig 5.6) and are produced by amphibole, muscovite (phengite) and biotite dehydration melting (with increasing temperature in constant pressure). This produces primary melts with very high (up to 20%) water contents. Two groups of melt compositions are formed on the TAS classification. The less silica rich (<70%) group corresponds to early stages, relatively low volume melt production, whereas the more silica rich group corresponds to later, more voluminous stage of melt production. These stages can be mostly related to the melting reactions of amphibolite/phengite-out and biotite-out, respectively. Proceeding melting reactions produce compositional variation in the melts, especially in sodium and potassium content. The pressure-temperature conditions of melting vary because during strong lithospheric thinning the crustal temperatures increase but also some of the crustal material is dragged downwards by the small-scale convection (cf Fig 5.5). The first melts show strong peraluminious nature (Fig 5.7) but there is a tendency to lower A/CNK ratios (molecular Al/(Ca+Na+K)) as the source rock depletion progresses. The melting regions progressing horizontally (cf. Fig 5.3) show consistently strong peraluminous nature because as the region influenced by the lithospheric thinning spreads sideways, new non-depleted crust is exposed to the heating by the asthenosphere. All the melts extracted have low concentrations (< 2 wt-%) of CaO, FeO and MgO, without clear temporal

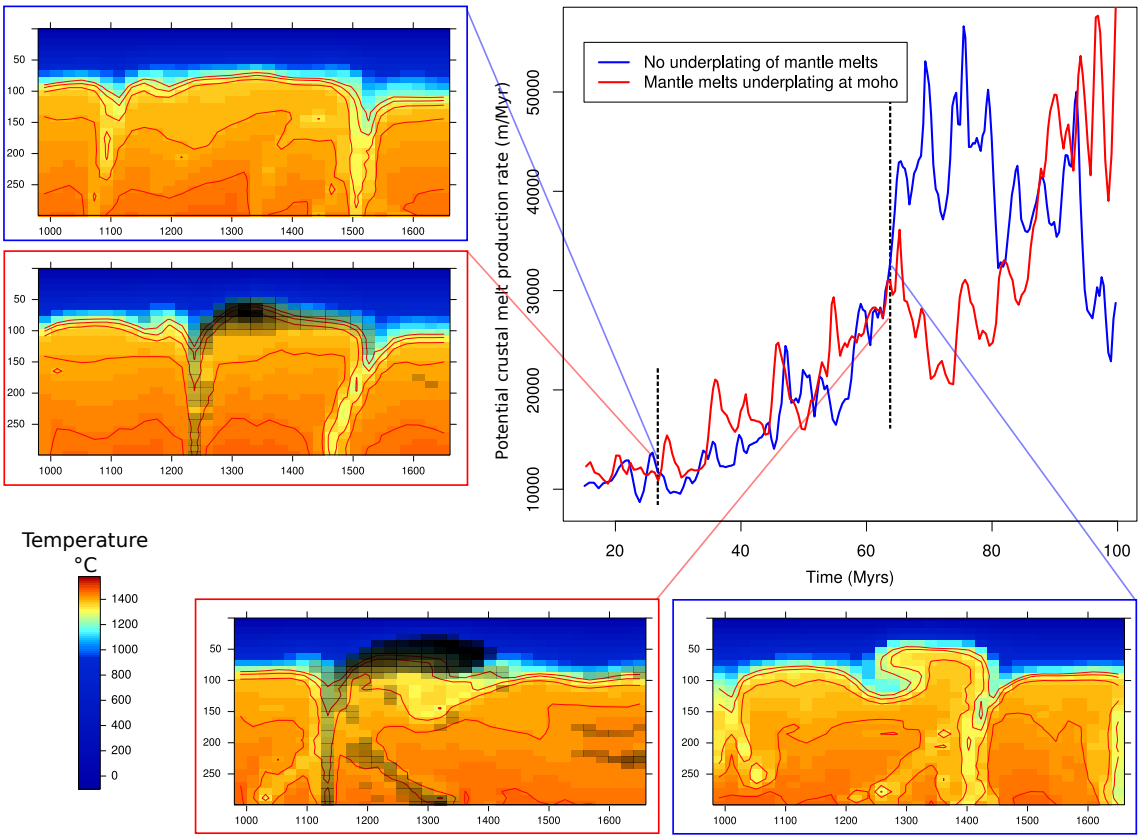

Figure 5.4: Potential crustal melt production rates as a function of time, from two models B and C (Table 5.1): One in which mantle melts are extracted and advected to the moho level (red line), one in which mantle melts are not extracted (blue line). Other model parameters are the same. In neither of the cases are crustal melts extracted, i.e. melting rates shown are potential melting rates. Boxes on the left and at the bottom show the temperature (colour scale) and depletion fields (black) at t=37 Myrs and t=76 Myrs, respectively. At 37 Myrs underplating of mafic magmas at the moho enhances crustal melting via advective heating. As mantle melting continues, a stronger layer of depleted mantle forms (lower left panel, the black layer) which stagnates the formation of crustal melts. Where mantle melts are not extracted (lower right panel, on depleted layer), the melt weakening of both crust and mantle can freely contribute to the further thinning of the lithosphere and more voluminous crustal melt production.

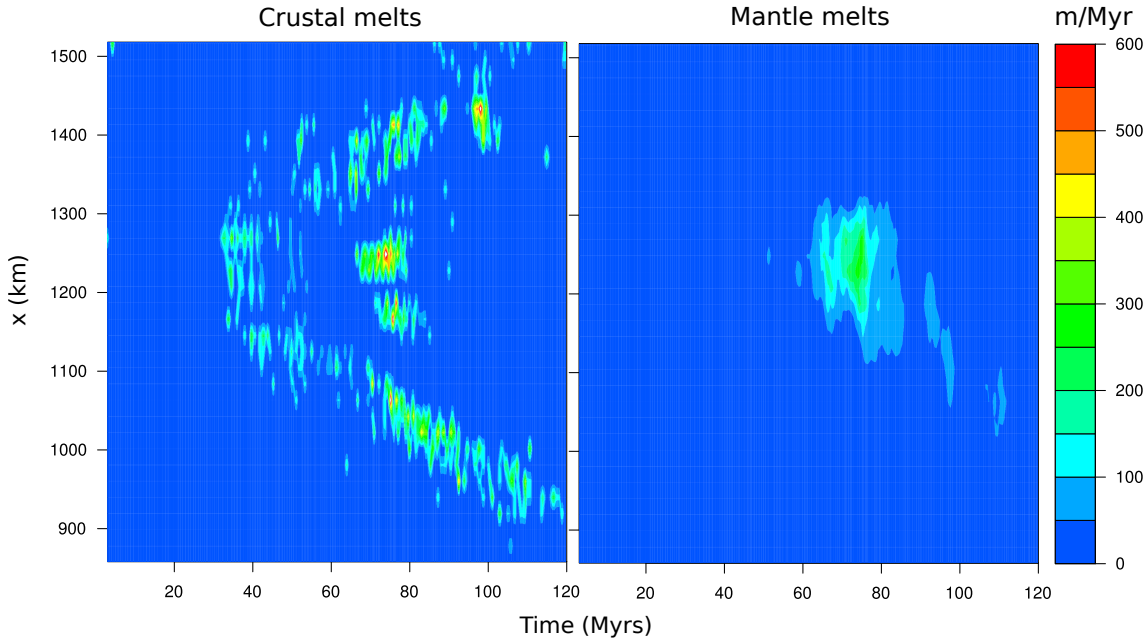

Figure 5.5: Extraction rates of crustal and mantle melts of model D (Table 5.1). Minor extraction of crustal melts starts at about t=30 Myrs. However, it takes another 20 Myrs before a more voluminous phase of mantle melting starts (at location x=1200..1300 km). This melting phase is associated with production of mantle melts, i.e. the more voluminous crustal melting phase is contemporary with strong lithospheric thinning. The crustal melting taking place on the sides, at x $>$ 1300 km and x $<$ 1100 km is produced by the convective removal of the lithosphere where pieces of lower crust is dragged downwards and horizontally into the hotter asthenosphere.

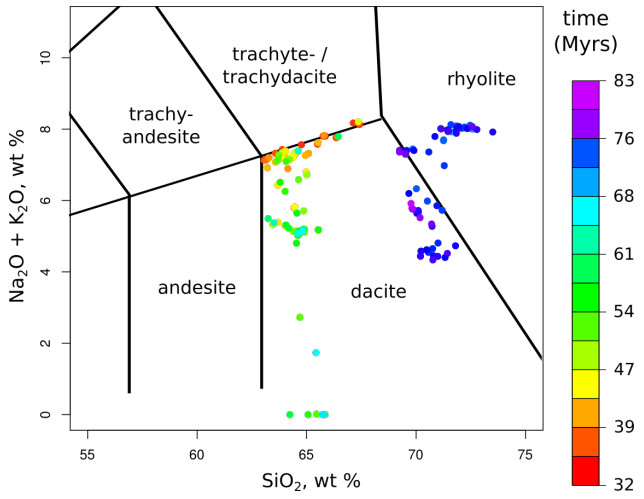

Figure 5.6: Composition of the extracted crustal melts on a totali alkali vs silica content (TAS) diagram. Compositions are from model D, shown in Fig 5.5, at location 1100 km $<$ x $<$ 1300 km. Two groups can be observed: the more silica rich group are the melts produced in the second, more voluminous, melting phase, and the first group represents the less voluminous melting before them (cf. Fig 5.5). Both groups show temporal evolution to less alkaline direction (red to green in the first group and blue to purple in the second group).

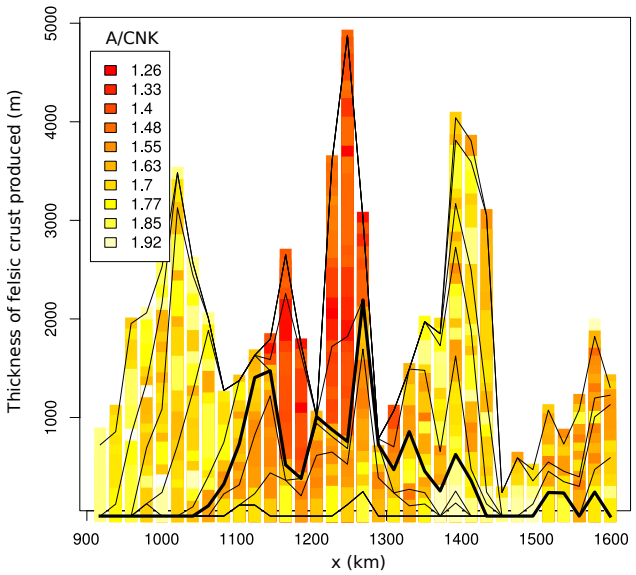

Figure 5.7: "Stratigraphic section" of felsic melts produced (model D, cf. Figs 5.5 and 5.6) assuming all crustal melts percolate to the surface forming a layer of felsic rock. Colours indicate aluminium saturation index, A/CNK (molar $Al_2O_3/(CaO + Na_2O + K_2O)$). Thin black lines are isochrons separated by 10 Myrs. A thick black line marks the t=65 Myrs isochron.

evolution.

The dynamic topography in the models (5.8) is produced to first order by the local thinning of the lithosphere by mantle upwellings. However, melt weakening with its positive feedback to lithospheric thinning causes increased dynamic topography variation within one model: more intensively thinned regions have higher dynamic topography because of stronger thinning and, accordingly, regions of mantle downwelling have stronger negative dynamic topography. This causes higher stresses within the middle-upper crust and an extensional stress fields above thinned regions.

5.4 Discussion

The timeline for extraction of melts (i.e. model D, Figs 5.5, 5.6 and 5.7) shows features similar to the evolution of post-collisional intrusions in Velay dome region of Variscan orogen and in the southern Svecofennian orogeny. There is a prolonged timespan of tens of millions of years of crustal melting before a more voluminous pulse of melt extraction takes place at about t=65 Myrs (cf. Fig 5.5, region 1100 km $<$ x $<$ 1300 km). Some melts are extracted before 65 Myrs but the more voluminous phase is associated with extraction of mantle melts at the same time. The crustal melts extracted are strongly peraluminous and low in CaO, FeO and MgO, reminescent of leucogranitic composition. The composition of the crustal melts in the more voluminous phase evolves towards less peraluminous compositions and higher silica contents. This evolution of crustal melting can be directly compared to that observed by Couzinié et al. (2014), shown in Fig 5.1. In the Velay dome region, migmatization of the crust and production of small volumes of leucogranitic melts dominates the first 20-30 Myrs, after which a more voluminous phase of granitic, less peraluminous, melt production, contemporary to extrusion of mantle melts (vaugnerites), happens in relatively short time ($<$ 10 Myrs). Production of strongly peraluminous crustal melts continues in the model outside the middle region (1100 km $<$ x $<$ 1300 km) and outside the region of mantle

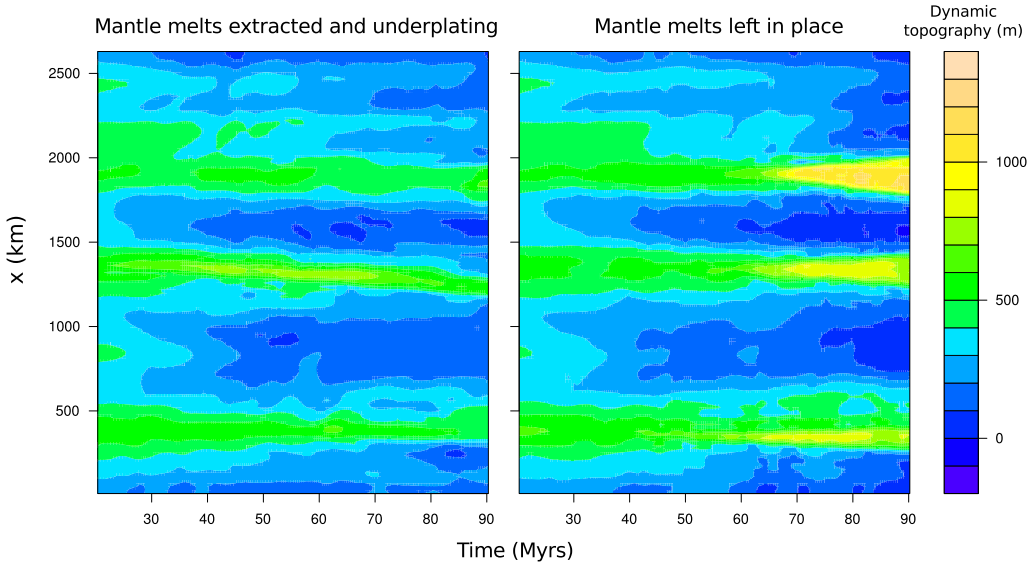

Figure 5.8: Dynamic topography caused by the lithospheric thinning (models B and C). Three regions of lithospheric thinning can be seen. Timeline at location x=1300..1400 km can be compared to the timeline in Fig 5.4. Moderate dynamic topography is caused by the thinning of the lithosphere by small-scale convection. A more significant thinning event can be seen at t=50..70 Myrs when melt weakening starts to enhance the lithosphere removal (right panel). This is not seen on the model (left panel) where mantle melts are extracted and no melt weakened layer is formed. The regions of uplift are associated with tensional strain at the surface.

melt production whereas plutonism at the Velay dome region stopped after the voluminous granite emplacement. Thus, melt extraction outside the middle region, predicted by the model, seem not to be present at the Velay dome region.

In the southern part of the Svecofennian orogeny, a long period of leucogranite production is also present and compatible with model observations. A late-orogenic (second) metamorphic peak at 1.83-1.81 Ga takes place 40 to 60 Myrs after the main collisional stage, in the middle of emplacement of the leucogranitic plutons (1.86 to 1.79 Ga). Here, the late-orogenic metamorphic peak could be related to the voluminous crustal melting phase predicted by the model, as it is associated with enhanced lithospheric thinning and production of mantle melts. This coincides with observations of mantle-derived shoshonitic magmatism dated to 1.82-1.79 Ga (Rutanen et al., 2011).

Thinning of the lithospheric mantle causes uplift (Fig 5.8). The tensional strain associated with the uplift in the models can be related to the extensional features observed in migmatite zones of Svecofennian orogeny and the Velay dome region. Because intensified melt production and surface uplift are contemporous with the strenghtened lithosphere thinning, these three events could be related to the collapse of the orogen, emplacement of granitic plutons and exhumation of the migmatite belts via extensional tectonics.

The extraction of some strongly peraluminous melts in our model continues outside the region of strongest lithosphere thinning. This might correspond to the emplacement of leucogranitic melts after the 1.83-1.82 Ga extension (collapse?) of the crust in the Svecofennian orogeny.

The models shown here do not take into account the greater radiogenic heating caused by the thick-

ening of the continental crust. However, our models show that purely mantle-dominated processes can cause crustal anatexis assuming post-collisional small-scale convection at the asthenosphere-lithosphere boundary and the positive feedback between mantle/crustal melting and further lithosphere thinning by melt weakening. Dome-like structures at the lithosphere bottom can be formed by localized thinning (cf Fig 5.3b) and this can be a cause for the metamorphic zoning of migmatite domes formed at lower and middle crust levels. Increased radiogenic heating by crustal thickening would raise the geotherm and cause more extensive melting. The long relaxation times, however, mean that the melt production by this mechanism would take up to 50 Myrs after the crustal thickening to initiate (Thompson and Connolly, 1995), and thus would not be responsible for the initial anatexis of the lower crust but would increase the melt volumes during later stages, i.e. in our models at the second, more voluminous phase of melt production.

The initial thinning in our models is caused by small-scale convection, itself being a consequence of increased water contents in the upper mantle. However, the positive feedback between the initial thinning and the enhanced mantle delamination does not depend on the initial mechanism. The initial mechanism for minor lithospheric thinning could be also, for example, a thermal upwelling in the upper mantle that is strong enough to cause even minor melting in the lower crust.

The sequence of events observed in our model—crustal anatexis, contemporaneous mantle melting and voluminous crustal melting, extensional stress fields—seems to fit to the idea of a post-collisional phase ending in a crustal collapse. However, the geochemical patterns observed here are somewhat in disagreement with the idea by Bonin et al. (1998) that the transition from post-collisional to post-orogenic stage would be marked by a shift into alkaline magmatic suites: The evolution of the aluminium saturation index (Fig 5.7) does show decrease in A/CNK values towards more alkaline, but the absolute values are still very clearly strongly peraluminious. In addition, our models show high sodium and potassium contents throughout the temporal evolution and no transition into more sodic compositions. However, as noted before, increased radiogenic heating by crustal thickening is not taken into consideration here, and it is possible that middle to upper crustal anatexis might be introduced with help from increased radiogenic heating, and thus variable crustal sources introduced at the late stages of the model. Also, the mixing of mantle melts with crustal melts is not considered, and neither is the evolution in the composition of the mantle melts. It is very likely that these factors complicate the compositional evolution of the melts.

The underplating of mafic magmas has been suggested as an additional heating mechanism for production of crustal melts in post-collisional settings (e.g. Williamson et al., 1992; Laube and Springer, 1998). Even if seismic, geochemical and petrological evidence for underplating exists, the plausibility of this mechanism to significantly enhance crustal melting is hindered by the slow conductive cooling time scales (Hanson and Barton, 1989). In addition, our results show that even though the underplating initially enhances lower crustal melting, its overall effect is minor or even negative because the mantle melt extraction produces a high viscosity depleted layer in the lithospheric mantle, prohibiting further thinning of the lithosphere. This prohibiting effect is dependent on the thresholds applied for melt extraction from the mantle.

5.5 Conclusions

Our models of mantle convection that quantify the feedback mechanisms between melting and melt weakening and, on the other hand, depletion stiffening, show that significant crustal melting can be produced in a post-collisional setting by the thinning of the lithospheric mantle and its subsequent positive feedback mechanisms. A long-term partial crustal melting takes place in the lower crust before more pervasive melting stage of granitic melt production. The associated mantle melts underplating the crust do enhance crustal melting initially but their overall contribution to the crustal anatexis is minor because of negative feedback between melting and melt extraction, depletion stiffening and lithosphere thinning. Dynamic uplift caused by the enhanced lithospheric mantle thinning and the related extensional surface stress regime coincide with strong crustal and mantle melt pulses, thus producing an environment very much like the ones in orogenic collapses hypothesized for migmatite-granite dome regions.

References

Bea, F. (2012). "The sources of energy for crustal melting and the geochemistry of heat-producing elements". In: *Lithos* 153, pp. 278–291.

Bird, P. (1979). "Continental Delamination and the Colorado Plateau". In: *Journal of Geophysical Research* 84.B13, pp. 7561–7571.

Bonin, B. (2004). "Do coeval mafic and felsic magmas in post-collisional to within-plate regimes necessarily imply two contrasting, mantle and crustal, sources? A review". In: *Lithos* 78.1-2, pp. 1–24.

Bonin, B., A. Azzouni-Sekkal, F. Bussy, and S. Ferrag (1998). "Alkali-calcic and alkaline post-orogenic (PO) granite magmatism: petrologic constraints and geodynamic settings". In: *Lithos* 45, pp. 45–70.

Bouilhol, P., A. F. Leyreloup, C. Delor, A. Vauchez, and P. Monié (2006). "Relationships between lower and upper crust tectonic during doming: the mylonitic southern edge of the Velay metamorphic core complex (Cévennes-French Massif Central)". In: *Geodinamica Acta* 19.3-4, pp. 137–153.

Bouilhol, P., V. Magni, J van Hunen, and L. Kaislaniemi (2014). "A numerical approach to melting in warm subduction zones". In: *Earth and Planetary Science Letters*, (in review).

Christensen, U. R. and D. A. Yuen (1985). "Layered Convection Induced by Phase Transitions". In: *Journal of Geophysical Research* 90.B12, pp. 10291–10300.

Connolly, J. A. D. (2005). "Computation of phase equilibria by linear programming: A tool for geodynamic modeling and its application to subduction zone decarbonation". In: *Earth and Planetary Science Letters* 236.1-2, pp. 524–541.

Costa, S. and P. Rey (1995). "Lower crustal rejuvenation and growth during post-thickening collapse: Insights from a crustal cross section through a Variscan metamorphic core complex". In: *Geology* 23.10, pp. 905–908.

Couzinié, S., J.-F. Moyen, A. Villaros, J.-L. Paquette, J. H. Scarrow, and C. Marignac (2014). "Temporal relationships between Mg-K mafic magmatism and catastrophic melting of the Variscan crust in the southern part of Velay Complex (Massif Central, France)". In: *Journal of GEOsciences* 59, pp. 69–86.

Davies, J. H. and F. von Blanckenburg (1995). "Slab breakoff: A model of lithosphere detachment and its test in the magmatism and deformation of collisional orogens". In: *Earth and Planetary Science Letters* 129.1-4, pp. 85–102.

Dilek, Y. and S. Altunkayanak (2007). "Cenozoic Crustal Evolution and Mantle Dynamics of Post-Collisional Magmatism in Western Anatolia". In: *International Geology Review* 49, pp. 431–453.

Dixon, J. E., T. H. Dixon, D. R. Bell, and R Malservisi (2004). "Lateral variation in upper mantle viscosity: role of water". In: *Earth and Planetary Science Letters* 222.2, pp. 451–467.

Faure, M., J.-M. Lardeaux, and P. Ledru (2009). "A review of the pre-Permian geology of the Variscan French Massif Central". In: *Comptes Rendus Geoscience* 341.2-3, pp. 202–213.

Franke, W. (2000). "The mid-European segment of the Variscides: tectonostratigraphic units, terrane boundaries and plate tectonic evolution". In: *Geological Society, London, Special Publications* 179, pp. 35–61.

Fuhrman, M. L. and D. H. Lindsley (1988). "Ternary-feldspar modeling and thermometry". In: *American Mineralogist* 73, pp. 201–215.

Gerdes, A., G. Wörner, and A. Henk (2000). "Hybrids, magma mixing and enriched mantle melts in post-collisional Variscan granitoids: the Rastenberg Pluton, Austria". In: *Geological Society, London, Special Publications* 179.1, pp. 415–431.

Gerya, T. V. and D. A. Yuen (2003). "Characteristics-based marker-in-cell method with conservative finite-differences schemes for modeling geological flows with strongly variable transport properties". In: *Physics of the Earth and Planetary Interiors* 140.4, pp. 293–318.

Hanson, R. B. and M. D. Barton (1989). "Thermal Development of Low-Pressure Metamorphic Belts: Results From Two-Dimensional Numerical Models". In: *Journal of Geophysical Research* 94.B8, pp. 10363–10377.

Holland, T. J. B. and R. Powell (1998). "An internally consistent thermodynamic data set for phases of petrological interest". In: *Journal of Metamorphic Geology* 16.3, pp. 309–343.

Holland, T. and R. Powell (1991). "A Compensated-Redlich-Kwong (CORK) equation for volumes and fugacities of CO_2 and H_2O in the range 1 bar to 50 kbar and 100-1600°C". In: *Contributions to Mineralogy and Petrology* 109, pp. 265–273.

Holt, W. E. and T. C. Wallace (1990). "Crustal Thickness and Upper Mantle Velocities in the Tibetan Plateau Region From the Inversion of Regional Pnl Waveforms: Evidence for a Thick Upper Mantle Lid Beneath Southern Tibet". In: *Journal of Geophysical Research* 95.B8, pp. 12499–12525.

Huppert, H. E. and R. S. J. Sparks (1988). "The generation of granitic magmas by intrusion of basalt into continental crust". In: *Journal of Petrology* 29.3, pp. 599–624.

Kaislaniemi, L., J. van Hunen, M. B. Allen, and I. Neill (2014). "Sublithospheric small-scale convection–A mechanism for collision zone magmatism". In: *Geology* 42.4, pp. 291–294.

Katz, R. F., M. Spiegelman, and C. H. Langmuir (2003). "A new parameterization of hydrous mantle melting". In: *Geochemistry Geophysics Geosystems* 4.9, p. 1073.

Kohlstedt, D. L., B. Evans, and S. J. Mackwell (1995). "Strength of the lithosphere: Constraints imposed by laboratory experiments". In: *Journal of Geophysical Research* 100.B9, pp. 17587–17602.

Korsman, K., T. Korja, M. Pajunen, P. Virransalo, and G. W. Group (1999). "The GGT/SVEKA Transect: Structure and evolution of the Continental Crust in the Paleoproterozoic Svecofennian Orogen in Finland". In: *International Geology Review* 41, pp. 287–333.

Kukkonen, I. and L. Lauri (2009). "Modelling the thermal evolution of a collisional Precambrian orogen: High heat production migmatitic granites of southern Finland". In: *Precambrian Research* 168.3-4, pp. 233–246.

Kurhila, M., T. Andersen, and O. T. Rämö (2010). "Diverse sources of crustal granitic magma: Lu-Hf isotope data on zircon in three Paleoproterozoic leucogranites of southern Finland". In: *Lithos* 115.1-4, pp. 263–271.

Laube, N. and J. Springer (1998). "Crustal melting by ponding of mafic magmas: A numerical model". In: *Journal of Volcanology and Geothermal Research* 81.1-2, pp. 19–35.

Ledru, P., G. Courrioux, C. Dallain, J. M. Lardeaux, J. M. Montel, O. Vanderhaeghe, and G. Vitel (2001). "The Velay dome (French Massif Central): melt generation and granite emplacement during orogenic evolution". In: *Tectonophysics* 342, pp. 207–237.

Liégeois, J.-P., J. Navez, J. Hertogen, and R. Black (1998). "Contrasting origin of post-collisional high-K calc-alkaline and shoshonitic versus alkaline and peralkaline granitoids. The use of sliding normalization". In: *Lithos* 45, pp. 1–28.

Mei, S., W. Bai, T. Hiraga, and D. Kohlstedt (2002). "Influence of melt on the creep behavior of olivine-basalt aggregates under hydrous conditions". In: *Earth and Planetary Science Letters* 201.3-4, pp. 491–507.

Miller, C., R. Schuster, U. Klötzli, W. Frank, and F. Purtscheller (1999). "Post-Collisional Potassic and Ultrapotassic Magmatism in SW Tibet : Geochemical and Sr-Nd-Pb-O Isotopic Constraints for Mantle Source Characteristics and Petrogenesis". In: *Journal of Petrology* 40.9, pp. 1399–1424.

Moresi, L. and M. Gurnis (1996). "Constraints on the lateral strength of slabs from three-dimensional dynamic flow models". In: *Earth and Planetary Science Letters* 138, pp. 15–28.

Nelson, K. D., W. Zhao, L. D. Brown, J. Kuo, J. Che, X. Liu, S. L. Klemperer, Y. Makovsky, R. Meissner, J. Mechie, et al. (1996). "Partially Molten Middle Crust Beneath Southern Tibet: Synthesis of Project INDEPTH Results". In: *Science* 274.5293, pp. 1684–1688.

Nironen, M. and M. Kurhila (2008). "The Veikkola granite area in southern Finland: emplacement of a 1.83-1.82 Ga plutonic sequence in an extensional regime". In: *Bulletin of the Geological Society of Finland* 80.1, pp. 39–68.

Pearce, J. A., J. F. Bender, S. E. Delong, W. S. F. Kidd, P. J. Low, Y. Guner, F. Saroglu, Y. Yilmaz, S. Moorbath, and J. G. Mitchell (1990). "Genesis of collision volcanism in Eastern Anatolia, Turkey". In: *Journal of Volcanology and Geothermal Research* 44.1-2, pp. 189–229.

Poudjom Djomani, Y. H., S. Y. O'Reilly, W. L. Griffin, and P. Morgan (2001). "The density structure of subcontinental lithosphere through time". In: *Earth and Planetary Science Letters* 184, pp. 605–621.

Ranalli, G. and D. C. Murphy (1987). "Rheological stratification of the lithosphere". In: *Tectonophysics* 132, pp. 281–295.

Rudnick, R. L. and D. M. Fountain (1995). "Nature and composition of the continental crust: a lower crustal perspective". In: *Reviews of Geophysics* 33.3, pp. 267–309.

Rutanen, H., U. B. Andersson, M. Väisänen, A. k. Johansson, S. Fröjdö, Y. Lahaye, and O. Eklund (2011). "1.8 Ga magmatism in southern Finland: strongly enriched mantle and juvenile crustal sources in a post-collisional setting". In: *International Geology Review* 53.14, pp. 1622–1683.

Rybacki, E., M. Gottschalk, R. Wirth, and G. Dresen (2006). "Influence of water fugacity and activation volume on the flow properties of fine-grained anorthite aggregates". In: *Journal of Geophysical Research* 111.B3, B03203.

Schutt, D. L. and C. E. Lesher (2006). "Effects of melt depletion on the density and seismic velocity of garnet and spinel lherzolite". In: *Journal of Geophysical Research* 111.B5, pp. 1–24.

Skyttä, P. and I. Mänttäri (2008). "Structural setting of late Svecofennian granites and pegmatites in Uusimaa Belt, SW Finland: Age constraints and implications for crustal evolution". In: *Precambrian Research* 164.1-2, pp. 86–109.

Thompson, A. B. and J. A. D. Connolly (1995). "Melting of the continental crust: Some thermal and petrological constraints on anatexis in continental collision zones and other tectonic settings". In: *Journal of Geophysical Research* 100.B8, pp. 15565–15579.

Väisänen, M., I. Mänttäri, L. M. Kriegsman, and P. Hölttä (2000). "Tectonic setting of post-collisional magmatism in the Palaeoproterozoic Svecofennian Orogen, SW Finland". In: *Lithos* 54, pp. 63–81.

Vanderhaeghe, O., C. Teyssier, and R. Wysoczanski (1999). "Structural and geochronological constraints on the role of partial melting during the formation of the Shuswap metamorphic core complex at the latitude of the Thor-Odin dome, British Columbia". In: *Canadian Journal of Earth Sciences* 36.6, pp. 917–943.

Vigneresse, J. L., P. Barbey, and M. Cuney (1996). "Rheological Transitions During Partial Melting and Crystallization with Application to Felsic Magma Segregation and Transfer". In: *Journal of Petrology* 37.6, pp. 1579–1600.

Wang, Y. F., J. F. Zhang, Z. M. Jin, and H. W. Green (2012). "Mafic granulite rheology: Implications for a weak continental lower crust". In: *Earth and Planetary Science Letters* 353-354, pp. 99–107.

White, R. W., R. Powell, and T. J. B. Holland (2001). "Calculation of partial melting equilibria in the system Na2O-Cao-K2O-FeO-MgO-Al2O3-SiO2-H2O (NCKFMASH)". In: *Journal of Metamorphic Geology* 19, pp. 139–153.

Williams, H. M. (2004). "Nature of the Source Regions for Post-collisional, Potassic Magmatism in Southern and Northern Tibet from Geochemical Variations and Inverse Trace Element Modelling". In: *Journal of Petrology* 45.3, pp. 555–607.

Williamson, B. J., H. Downes, and M. F. Thirlwall (1992). "The relationship between crustal magmatic underplating and granite genesis: an example from the Velay granite complex, Massif Central, France". In: *Transactions of the Royal Society of Edinburgh: Earth Sciences* 83.1-2, pp. 235–245.

Zhong, S., M. T. Zuber, L. Moresi, and M. Gurnis (2000). "Role of temperature-dependent viscosity and surface plates in spherical shell models of mantle convection". In: *Journal of Geophysical Research* 105.B5, pp. 11063–11082.

Chapter 6

Concluding remarks

6.1 Summary

A common thread within the thesis has been the post-collisional convective activation of the lithosphere-asthenosphere boundary (LAB) by increased water contents and subsequent sub-lithospheric small-scale convection (SSC). **Chapter 3** determines the temporal and spatial patterns and volumes of volcanism produced by SSC in the presence of elevated water contents and in the absence of significant plate movement. The irregular patterns of the melt production correspond to those observed in post-collisional mantle-derived magmatism in orogenic plateaux, especially the Turkish-Iranian plateau. The observed SSC is reminescent of the convective removal of thickened lithosphere, however, the important difference being that convective activation of the LAB happens by increasing water contents, "hydrous activation", from below, instead of lithospheric thickening. This can explain the orogenic plateau magmatism even if no tectonic activity or deformation is observed, as is often the case in post-collisional settings where different continental blocks start to behave as one coherent plate. This might have implications for other intraplate magmatism near previous subduction zones, such as the circum-Mediterranean anorogenic igneous activity. The water inputted into the mantle during the long history of multiple subduction zones around the Mediterranean region could have stored significant amounts of water at the upper mantle transition zone, from where the water is able to escape back to the asthenosphere long after cessation of the subduction.

Chapter 4 studies the small-scale convection in the presence of a significant lithosphere thickness gradient, applying the results to the intraplate orogeny of the Moroccan Atlas mountains. The edge-driven convection (EDC) cell produced by a lithospheric thickness gradient is able to produce localized uplift and volcanism. As collision zones bring together lithospheric plates of different thicknesses, and the collision itself thickens the lithosphere, it is expected that thickness gradients exist at or near collision zones. These thickness gradients can then cause EDC and be responsible for some of the post-collisional magmatism. The weakening of the upper mantle by small amounts of water is required to reduce the EDC cell size and to produce significant localized lithosphere erosion by the EDC cell. EDC is shown to work in combination with shear-driven upwelling: A

significant thickness gradient in the lithosphere usually implies the presence of thick strong cratonic lithosphere that is able to thermally insulate the asthenosphere below it, producing higher mantle temperatures under the craton than under the thinner lithospheric domain next to it. This induces horizontal flow and shear-driven upwelling near the edge. EDC is expected to operate at many craton boundaries at the passive margins, but for the EDC to be able to produce magmatism, an elevated mantle water content is needed. The 3D structure of EDC is more complex than could be envisaged from the 2D models, and produces tubular convection cells that are similar to ones observed in a SSC under an moving lithosphere plate.

Chapter 5 studies how SSC can initiate strong lithospheric thinning and crustal melting. A local thinning in the lithosphere can cause lower crust anatexis via conductive heating. The viscosity reducing effect of partial melts within the rock matrix causes positive feedback in the thinning of the lithosphere: Once small amounts of partial melt is formed in the lower crust, this melt weakening effect reduces the strength of the crust-mantle boundary and may allow the detachment of the lithospheric mantle from the crust. This causes asthenosphere upwelling and decompression melting, and exposes the crust to the hot asthenosphere, producing more extensive crustal melting. The loss of the lithospheric mantle causes uplift and extensional stress field at the surface. This chain of events—crustal anatexis, sudden extensive crustal melting and melt extraction together with mantle derived melts, uplift and crustal extension—corresponds to what is usually called the orogenic collapse. The models shown do not take into account the existence of the thickened crust—the process is purely driven by mantle processes. A collaborating process, crustal heating by thickened crust with more radiogenic heat available and consequent mid-crustal weakening, may be in progress simultaneously. The SSC studied in Chapter 3 can be the process causing the small thinning that initiates the loss of the lithospheric mantle as described above.

6.2 Directions for future studies

All the studies in this thesis show significant feedback mechanisms between melting and residue composition changes. Melt extraction removes water with the melts and causes the residue composition to become drier and thus more viscous and less prone to further melting. This forms strong depleted layers at the bottom of the lithosphere, stabilizing the lithosphere against erosion by small-scale convection. This post-collisional accretion of depleted material to the bottom of the lithosphere might be an important process in stabilizing orogenies. It could prevent reactivation and future rifting of the orogeny, despite the orogenic belt being a location for a great number of zones of weaknesses and thermal disturbances (cf. Krabbendam, 2001). Such stabilization could explain how active orogenies evolve into thick cratons, and how for example the Tibetan and Iranian plateaux seem to be regions of lithospheric thickening instead of thinning (McKenzie and Priestley, 2008). Similar processes take place at crustal level, where any crustal melts formed and extracted produce a refractory lower/middle crust, and move radiogenic heat sources to upper crustal level within the melts, thermally stabilizing the crust.

Partial melting prior to melt extraction can, however, weaken the crust and lithospheric mantle. These processes have positive feedback and could partially explain the sudden collapses of the orogenies. The extraction of melt from a partially molten rock is a complex process, length and time

scales of which are orders of magnitude smaller than those typically handled in a mantle convection model. Melt and magma viscosities are significantly smaller than unmolten rock viscosities and thus a two phase flow model is typically needed to model melt extraction from a rock. Another possible approach is to parameterize the melt extraction process so that they can be scaled up to length and time scales treatable in a mantle convection model.

As well as mantle processes affecting the crustal evolution (Chapter 5), the crustal evolution might affect the processes at the mantle level. Crustal scale collapse and thinning of the crust might introduce lithosphere uplift and thus asthenosphere upwelling (e.g. England and Houseman, 1989). Another mechanism for lithosphere thinning, initiated by crustal processes, could also be suggested: The thickening of the crust in an orogeny increases the amount of radiogenic heating and introduces a thicker, more insulating, cover at top of the lithospheric mantle. Together, these raise the geotherm temperatures throughout the lithosphere and this way thin the thickness of the thermal lithosphere. Complex mantle-crust interaction processes were also seen in Chapter 5, where it was shown that the intuitively clear hypothesis of underplating mafic magmas at moho level causing greater extent of crustal melting might not be completely correct because of the complementary process of mantle depletion and viscous stiffening taking place at lithosphere-asthenosphere boundary. Yet another possible example of the effect of even deeper processes at the crustal/lithosphere level is the possibility (Kuritani et al., 2011) of wet plumes originating from the upper mantle transition zone. The minerals storing water deep in the upper mantle might become unstable and release the water in them, affecting the lithosphere-asthenosphere boundary viscosity and causing small-scale convection. As these examples show, it is important for future modelling of orogenic processes to try to integrate crustal and upper mantle scale processes into one model and to carefully constrain the kinematic boundary conditions used in crustal/lithosphere scale models.

The usage of thermodynamic models (Gibbs energy minimization) within a large scale mantle convection model has become more and more popular, and greatly advances possible results from these models: the estimates for mantle mineralogies give an opportunity to model the seismic structure and compositional evolution of the mantle (Tirone et al., 2012; Connolly, 2009; Stixrude and Lithgow-Bertelloni, 2005; Connolly, 2005). These thermodynamic models, however, assume a chemical equilibrium, the assumption of which becomes easily invalid in a model where melt extraction takes place at short time scales. A melt percolating through a rock interacts with it and is being contaminated by the wall rock, but does not have enough time to reach chemical equilibrium, thus being outside the scope of Gibbs energy minimization based chemical models, and in need of models that take into account also kinematic constraints.

A great number of divisions and nomenclature has been proposed to describe the orogenic timeline: synorogenic, postorogenic, late orogenic, post-collisional, syn-collisional, anorogenic, etc. These are often based on geological, i.e. structural, petrological and geochemical, observations at the surface. Still, there is no consensus of the usage of the terms. This reflects mostly the complexity of the orogenic processes, but perhaps also the unrealistic goal of describing each event in the orogenic sequence with one primary driving mechanism. From a geodynamical point of view it seems clear that many of the large scale processes not only overlap but also interact with each other. The thinning of the lithosphere might start during the convergent thickening stage (convective removal of the lithosphere) and then continue seamlessly via the hydrous activation

of the lithosphere bottom, both of which could initiate large scale mantle delamination by local thinning and decoupling of the mantle and crust by partial melts. Other sudden (slab break-off) and more gradual (increased radiogenic heating) processes work at the same time. None of these processes have surface expressions (melt compositions, metamorphic effects, structural features) that would uniquely and unambiguously distinguish them from the rest of the processes. Also, orogenies are not spatially homogeneous: while overall convergence might still take place at the plateau boundaries (i.e. "orogenic" stage), the internal parts of the plateau might behave as one coherent plate without convergence, or even with large scale extension (i.e. post-orogenic). In the geodynamic context, then, it seems best to abandon the detailed division and nomenclature, and concentrate on the clearly defined events: collision (e.g. beginning of the subduction of continental crust), the long convergent stage after it, the collapse of the orogeny (end of orogenic stage), and finally the cessation of any tectonic activity (stabilization, the "anorogenic" stage).

References

Connolly, J. A. D. (2005). "Computation of phase equilibria by linear programming: A tool for geodynamic modeling and its application to subduction zone decarbonation". In: *Earth and Planetary Science Letters* 236.1-2, pp. 524–541.

– (2009). "The geodynamic equation of state: What and how". In: *Geochemistry Geophysics Geosystems* 10.10, Q10014.

England, P. and G. Houseman (1989). "Extension during continental convergence, with application to the Tibetan plateau". In: *Journal of Geophysical Research* 94.B12, pp. 17561–17579.

Krabbendam, M. (2001). "When the Wilson Cycle breaks down: how orogens can produce strong lithosphere and inhibit their future reworking". In: *Geological Society, London, Special Publications* 184.1, pp. 57–75.

Kuritani, T., E. Ohtani, and J.-I. Kimura (2011). "Intensive hydration of the mantle transition zone beneath China caused by ancient slab stagnation". In: *Nature Geoscience* 4.10, pp. 713–716.

McKenzie, D. and K. Priestley (2008). "The influence of lithospheric thickness variations on continental evolution". In: *Lithos* 102.1-2, pp. 1–11.

Stixrude, L. and C. Lithgow-Bertelloni (2005). "Mineralogy and elasticity of the oceanic upper mantle: Origin of the low-velocity zone". In: *Journal of Geophysical Research* 110.B03204.

Tirone, M., G. Sen, and J. P. Morgan (2012). "Petrological geodynamic modeling of mid-ocean ridges". In: *Physics of the Earth and Planetary Interiors* 190-191.October, pp. 51–70.